THESE DE DOCTORAT

ED 211 - Sciences exactes et leurs applications

Présentée et soutenue le : 13/12/2024
Par : Giberto Mitsuyoshi Yuki Junior

Thèse pour obtenir le grade de
Docteur de l'Université de Pau et des Pays de l'Adour
Génie des procédés
Docteur de l'Université de Turin
Sciences agricoles, forestières et alimentaire

Modeling of anaerobic digestion and its coupling with catalytic methanation

Thèse dirigée par : Frédéric MARIAS et Elio DINUCCIO

JURY

Président du jury

• Isabelle LE HECHO	Professeur des universités / IPREM / UPPA

Rapporteurs

• André PAUSS	Professeur des universités / TIMR / UTC
• Aras AHMADI	Maître de conférences HDR / TBI / INSA Toulouse

Examinateurs

• Cecilia SAMBUSITI	Docteur / TotalEnergies
• Luisella CELI	Professeur / DISAFA/ UniTO
• Fabrizio GIOELLI	Professeur associé / DISAFA / UniTO

TABLE OF CONTENTS

LIST OF TABLES

LIST OF FIGURES

ABSTRACT

With a growing share of energy being produced from renewable sources, new challenges emerge on how to deal with this new energy paradigm, where production is highly affected by conditions humans cannot manipulate. In the EU, wind and solar energy capacities have rapidly increased in recent years. Solar energy production peaks during sunny days and ceases at night, while wind energy generation fluctuates with wind speed. This variability in electricity production will have to be accounted for in the future energy grid, which will need new energy storage solutions and grid management strategies.

In this scenario, the development of multi-energy platforms will be required, as one source can compensate for or store the energy produced by another. In addition, it will enable to explore synergies from these different systems. Integrating methanation and anaerobic digestion, for instance, represents an alternative to convert renewable electricity into gas in a power-to-gas approach. Moreover, it enables the energetic valorization of CO_2 from biogas. However, these two reactors are operationally different in terms of their characteristic time and thermal behavior. For this reason, mathematical models can play a valuable role in defining their adequate management.

In such context, at first, a model for a biogas digester was developed. This model contains the kinetics from a modified version of the Anaerobic Digestion N°1 (ADM1), one of the most widespread models in this domain, along with an advanced thermal description based on empirical correlations for the heat transfer terms. In addition, the biogas storage in an air-inflated double-membrane gasholder was also included in this work. The digester model was validated using literature data for both lab-scale and large-scale digesters. It was also used in a study case to evaluate the influence of geographical location of the biogas plant on its heat losses.

To simulate an entire biomethane plant, the process units composing the biogas cleaning and upgrading stages were also modeled. Integrating these models with the digester

allowed for the evaluation of the entire system's functioning.

In addition, an existing model for catalytic methanation developed in a previous PhD thesis carried out in LaTEP was included in this simulation environment. This allowed simulating the whole system: biomethane and catalytic methanation plants. Simulations of this multi-energy platform showed that this solution would be able to store excess energy from the grid, as the start-up of the methanation reactors could started up within a few minutes. Besides, it was shown that the production in these reactors would be affected by seasonal variations in weather conditions. Finally, insights into the process safety of this system and potential opportunities for heat integration were discussed.

RÉSUMÉ EN FRANÇAIS

Avec une part croissante de l'énergie produite à partir de sources renouvelables, de nouveaux défis émergent quant à la gestion de ce nouveau paradigme énergétique, où la production est fortement influencée par des conditions que les humains ne peuvent pas manipuler. Dans l'UE, les capacités éoliennes et solaires ont rapidement augmenté ces dernières années. La production d'énergie solaire atteint son pic pendant les journées ensoleillées et cesse la nuit, tandis que la production d'énergie éolienne fluctue avec la vitesse du vent. Cette variabilité de la production d'électricité devra être prise en compte dans le futur réseau énergétique, qui nécessitera de nouvelles solutions de stockage d'énergie et des stratégies de gestion du réseau.

Dans ce scénario, le développement de plateformes multi-énergies sera nécessaire, car une source peut compenser ou stocker l'énergie produite par une autre. De plus, cela permettra d'explorer les synergies entre ces différents systèmes. L'intégration de la méthanation et de la digestion anaérobie, par exemple, représente une alternative pour convertir l'électricité renouvelable en gaz dans une approche power-to-gas. De plus, cela permet la valorisation énergétique du CO_2 provenant du biogaz. Cependant, ces deux réacteurs sont opérationnellement différents en termes de temps caractéristique et de comportement thermique. Pour cette raison, les modèles mathématiques peuvent jouer un rôle précieux dans la définition de leur gestion adéquate.

Dans ce contexte, un modèle pour un digesteur de biogaz a d'abord été développé. Ce modèle contient la cinétique d'une version modifiée du Anaerobic Digestion Model N°1 (ADM1), l'un des modèles les plus répandus dans ce domaine, ainsi qu'une description thermique avancée basée sur des corrélations empiriques pour les termes de transfert de chaleur. De plus, le stockage du biogaz dans un gazomètre à double membrane a également été inclus dans ce travail. Le modèle du digesteur a été validé à l'aide de données de la littérature pour des digesteurs à l'échelle de laboratoire et à grande échelle. Il a également été utilisé dans une étude de cas pour évaluer l'influence de la localisation géographique de l'usine de biogaz sur ses pertes de chaleur.

Pour simuler une usine de biométhane entière, les unités de traitement composant les étapes de nettoyage et de valorisation du biogaz ont également été modélisées. L'intégration de ces modèles avec le digesteur a permis d'évaluer le fonctionnement de l'ensemble du système.

De plus, un modèle existant de méthanation catalytique développé dans une thèse de doctorat précédente réalisée au LaTEP a également été inclus dans cet environnement de simulation. Cela a permis de simuler l'ensemble du système : usines de biométhane et de méthanation catalytique. Les simulations de cette plateforme multi-énergies ont montré que cette solution serait capable de stocker l'excès d'énergie du réseau, car le démarrage des réacteurs de méthanation pourrait être effectué en quelques minutes. En outre, il a été démontré que la production dans ces réacteurs serait affectée par les variations saisonnières des conditions météorologiques. Enfin, des perspectives sur la sécurité des procédés de ce système et des possibilités d'intégration thermique ont été discutées.

Nomenclature

A	Surface (m^2)
$A_{0,\ j}$	Frequency factor of hyrdolysis reaction j (s^{-1})
A_{0i}^{mem}	Frequency factor in membrane capcity estimation for compound i (mol s^{-1} Pa^{-1})
ASH	Ash content of biomass (%)
COD	Chemical oxygen demand (kg)
C_P	Heat capacity at constant pressure (J mol^{-1} K^{-1})
$\hat{C}_P$	Heat capacity at constant pressure (J kg^{-1} K^{-1})
cte	Constant
Cv	Heat capacity at constant volume (J mol^{-1} K^{-1})
C_V	Valve constant (Nm^3 h^{-1} mbar$^{-0.5}$)
C_i	Concentration of compound i (mol m^{-3})
D_h	Hydraulic diameter (m)
DHI	Diffuse horizontal irradiance (W m^{-2})
DNI	Direct normal irradiance (W m^{-2})
E	Energy (J)
E_{a_j}	Activation energy of reaction j (J mol^{-1} K^{-1})
f	Friction factor
F	Molar flow rate (mol s^{-1})
$\tilde{H}$	Molar enthalpy (J mol^{-1})
H	Enthalpy (J)
h	Convective heat transfer coefficient (W m^{-2} K^{-1})
HRT	Hydraulic retention time (d)
HT	Height (m)
I	Inhibition factor
ID	Internal diameter (m)
IR	Inner radius (m)
J	Radiosity (W m^{-2})
Q	Heat flow rate (W)

k_{DE}	Cell death kinetic constant (s^{-1})
k_G	Mass transfer coefficient in the gas phase ($m\ s^{-1}$)
k_{gain}	Gain of the P-controller
K_H	Henry's law constant ($mol\ m^3\ Pa^{-1}$)
K_I	Inhibition constant ($mol\ m^{-3}$)
k_j	Hydrolysis reaction constant of reaction j (s^{-1})
$k_{max,j}$	Maximum substrate uptake rate in reaction j (s^{-1})
K_S	Cosubstrate constant ($mol\ m^{-3}$)
k_La	Mass transfer coefficient in the liquid phase (s^{-1})
K_W	Ionic product of water ($10^{-14}\ mol^2\ L^{-2}$)
L	Length (m)
LHV	Lower heating value ($J\ kg_{-1}$)
LVL^G	Gas storage level
m	Month
m_f	Monthly biomass feed (kg)
m_{fuel}	Monthly fuel use (kg)
$\dot{m}_{HEX}$	Mass flow rate of water in the heat exchanger ($kg\ s^{-1}$)
$\dot{m}_{bias}$	Bias of the heat exchanger's P control ($kg\ m^{-1}$)
n	Molar quantity (mol)
N	Number of intervals or blower rotation speed (Hz)
N_m	Number of membrane modules in membrane stage m
o	Membrane cut-ratio
OD	Outer diameter (m)
OLR	Organic loading rate ($kg\ VS\ m^{-3}\ d^{-1}$)
OR	Outer radius (m)
P	Pressure (Pa)
pH_{LL}	Parameter that indicates pH lower limit
pH_{UL}	Parameter that indicates pH upper limit
Po	Power (W)

Q	Heat flow rate (W)
r_j	Reaction rate (mol s^{-1} m^{-3})
r_i	Permeation factor
R	Ideal gas constant (8.314 J K^{-1} mol^{-1})
R_{cap}	Radius of the spherical cap (m)
R_{th}	Thermal resistance (K W^{-1})
s_{hg}	Temperature deviation that leads to half growth rate (K)
SRT	Solid retention time (d)
t	Time (s)
T	Temperature (K)
T_a	Temperature at which the microorganisms are adapted to (K)
TMY	Typical metorological year
TS	Total solids (%)
u	Speed (m s^{-1}
U	Overall heat transfer coefficient (W m^{-2} K^{-1})
V	Volume (m^3)
$\dot{V}$	Volumetric flow rate (Nm^3 h^{-1})
VF	View factor
VFA	Volatile fatty acids
VS	Volatile solids
$\dot{W}_s$	Shaft work (W)
x_i	Molar fraction of compound i in liquid phase
Y	Generic data value
y_i	Molar fraction of compound i in gas phase
z	Length in the axis perpendicular to the spherical cap base (m)

Superscripts

A	Air layer
adv	Advection
cd	Conduction

cv	Convection
cv/cd	Convection and conduction
DHI	This indicates the surface that actually receive DHI
DNI	This indicates the surface that actually receive DNI
env	Environment
G	Gas phase
GL	Gas-liquid transfer
HEX	Heat exchanger
L	Liquid phase
rad	Radiation
sky	Sky
ug	Underground

Subscripts

$cool$	Cooling
el	Electric
f	Feed
for	Forced convection
GL	Gas-liquid transfer
HW	Hot water
i	Compound i
in	Inlet
ise	Isentropic
j	Reaction j or stream j
m	Membrane stabe
nat	Natural convection
net	Net
out	Outlet
p	Permeate
r	Retentate

R	Reaction
z	Types of energy efficiency (electric fuel and thermal)

Greek letters

α	Zenith angle
α_z	Absorptivity of surface z
α_R	Coefficient of linear variation of μ with temperature (s^{-1} K^{-1})
ν	Stoichiometric coefficient
θ	Inclination angle between a point in a spherical cap and the horizontal plan
μ	Microorganism maximum growth rate (s^{-1})
δ	Thickness (m) or pressure ratio
Δ	Variation or difference
ϵ	Emissivity or pipe roughness
η	Efficiency
κ	Polytropic coefficient
λ	Thermal conductivity (W m^{-1} K^{-1})
Ξ	Membrane permeability (mol m^{-2} s^{-1} bar^{-1})
ρ	Density (kg m^{-3})
σ	Stefan-Boltzmann constant (5.67 10^{-8} W m^{-2} K^{-4})
τ_a	Adaption time constant (s)
ψ	Angle between a tilted surface and the horizontal
ζ	Frictional losses in pipeline elements

Compounds

AA	Amino acids ($C_5H_{9.625}O_{2.5}N_{1.25}$)
CH	Carbohydrate ($C_6H_{10}O_5$)
HAc	Acetic acid ($C_2H_4O_2$)
HBu	Butyric acid ($C_4H_8O_2$)
HPr	Propionic acid ($C_3H_6O_2$)
HVa	Valeric acid ($C_5H_{10}O_2$)
$LCFA$	Long chain fatty acids ($C_{16}H_{32}O_2$)

LI	Lipids ($C_{51}H_{98}O_6$)
PR	Proteins ($C_5H_{7.625}O_{1.5}N_{1.25}$)
SU	Glucose ($C_6H_{12}O_6$)
X	Microorganism ($C_5H_7O_2N$)

Reactions

AE	Acetogenesis
AI	Acidogenesis
HY	Hydrolysis
ME	Methanogenesis

Model units

$3MEM$	Three-stage membrane separator
BGC	Biogas cleaner
CAT	Catalytic methanation reactor
CHL	Chiller
CMP	Compressor
DIG	Digester
GST	Gas stream
LST	Liquid stream

CHAPTER 1

CONTEXT AND OBJECTIVES

1.1 Context

In 2021, more than 77% of European greenhouse gas (GHG) emissions were originated from energy use or production [1]. To face the climate change, the European Union has stablished an audacious objective of becoming the first carbon neutral continent by 2050 [2]. This will require profound changes in the energy sector, which will have a growing share of renewable sources. Although fossil fuels still represented the largest fraction of final energy consumption in 2022, the participation of renewable energies has been steadily growing in the recent years (Figure 1.1) [3].

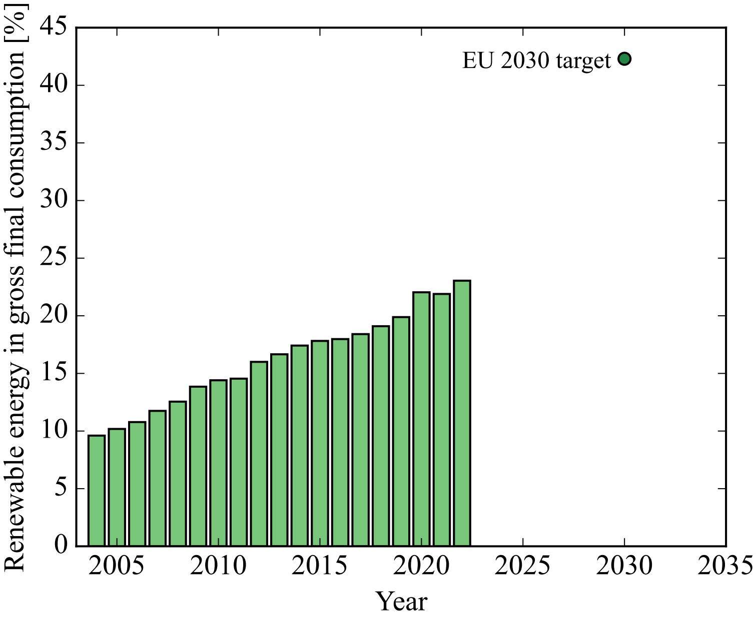

Figure 1.1: Share of renewable sources in EU final energy consumption. Adapted from [3].

To support this transition, a significant emphasis has been placed on intermittent renewable sources, notably wind and solar power. Indeed, from 2012 until 2022, the generation potential of these two sources increased by 1.9 and 2.6 fold respectively in the EU (Figure 1.2) [4]. Despite having a key importance in reducing greenhouse gas emissions, a high share of intermittent sources in the energy mix will require advancements in energy storage solutions and grid management to address their variability [5].

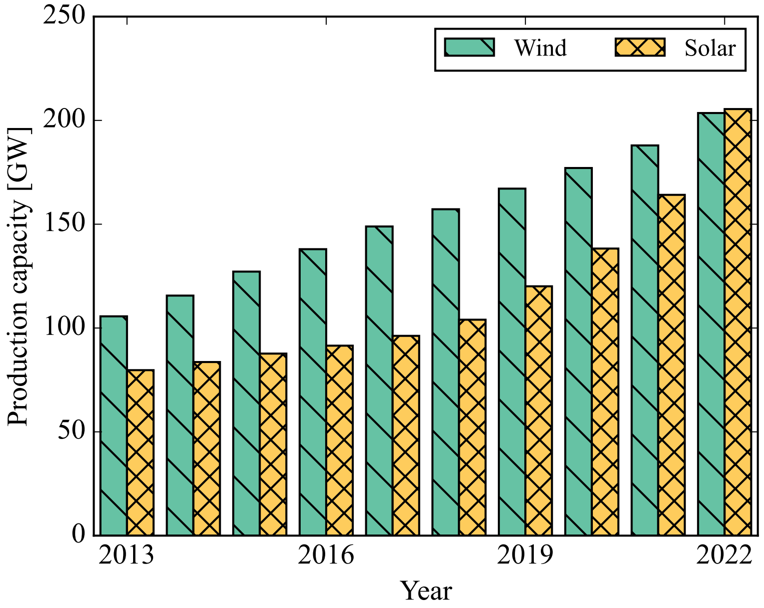

Figure 1.2: Production capacity of wind and solar energy in the EU.

1.1.1 Biogas

The biogas industry can play a major role in such energy transition. Not only it generates a green gas, it also produces a nutrient rich digestate that can be returned to the soil as a fertilizer, thus helping also to decarbonize the agriculture sector, which was responsible for 10.7 % of GHG European emission in 2021 [1]. The biogas generated from the degradation of organic matter is composed mainly by CH_4 and CO_2, and it can be energetically valorized in several ways. In combined heat and power units (CHP), it can be used to cogenerate heat and electricity. Alternatively, it can be upgraded into biomethane, which can be transported and stored in the existing natural gas infrastructure, or used as vehicle fuel. In addition, the biogas industry is already a mature sector, with over 18 000 operating plants across Europe [6].

In France, heat and power generation is the most common valorization route of biogas. However, in recent years, there has been a shift towards upgrading to biomethane. From 2018 until 2023, the number of biogas plants using a CHP increased by 2.1 fold, while biomethane upgrading increased by more than 10 fold in this same period (Figure 1.3 (a)) [7, 8]. The biogas plants are often classified according to the type of feedstock used. The agricultural sites are the most common among the French biomethane units (Figure 1.3 (b)) [8].

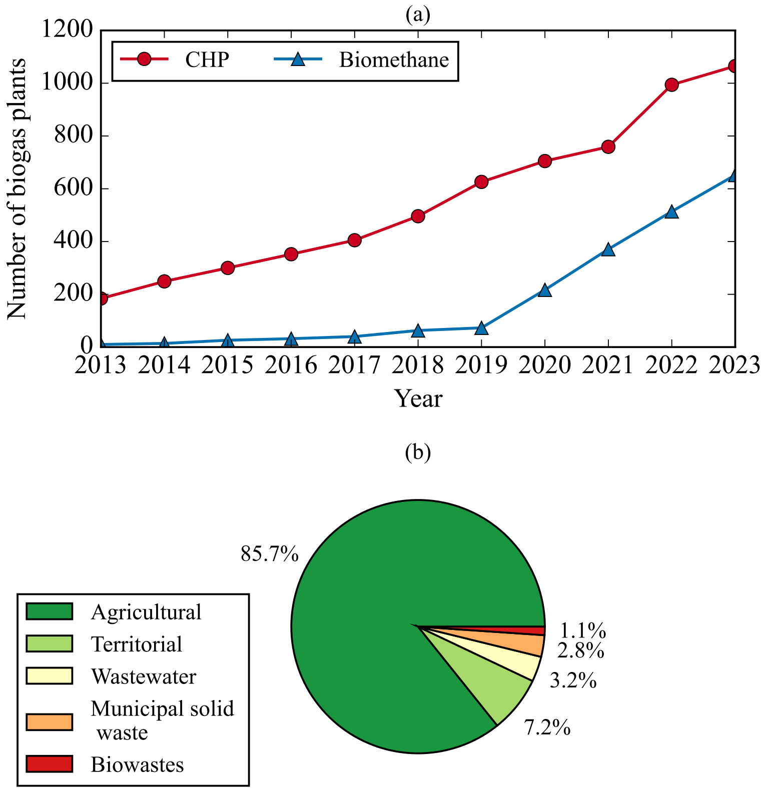

Figure 1.3: Number of cogeneration and biomethane plants in France (a) and classification of French biomethane plants (b).

In the current context, biomethane production offers some advantages over electricity generation using biogas. From an energy perspective, biomethane can be transported with minimal losses and stored in existing infrastructure used for natural gas. Therefore, it allows a temporary and local decoupling of production and utilization [9]. In addition, it has a higher flexibility in terms of utilization, as it can then be employed in electricity and heat generation, as a vehicle fuel, or as a reagent in chemical plants. Besides, biomethane plants achieved a higher energy conversion efficiency compared to cogeneration ones [10].

Regarding the environmental perspective, the comparative performance between biomethane production and cogeneration depended heavily on the carbon footprint of the country's electricity

[11]. In cases where the electricity generation is decarbonized, such as in France, the net GHG emissions of cogeneration plants might be positive, thus favoring the biomethane upgrading [11]. This scenario is the most likely for the upcoming years, with an increasing electricity production from renewable sources [12].

1.1.2 Power-to-gas

Other solution to the intermittency in electricity generation is to convert its surplus into hydrogen by electrolysis. Then, this gas can be reacted with CO_2 to form CH_4 using the methanation reaction. This approach is called Power-to-gas (P2G) and has many benefits [13]:

- Electricity storage;
- Possibility of using natural gas infrastructure for storing and transportation;
- CO_2 capture and valorization;
- Process waste heat can be recovered and used internally or sent to heat networks.

In this context, one promising possibility is to use the carbon dioxide from biogas to achieve a fully renewable energy system (Figure 1.4). Indeed, various projects in Europe are adopting this concept. For instance, in Lescar (France), there is the Cap Ecologia project, which will be a multi-energy platform that includes a wastewater anaerobic digester, a catalytic methanation reactor and an electrolyzer [14]. The yearly capacity of this plant will be of 13 000 MWh, from which more than 30% will come from the CO_2 conversion in the methanation reactor. The electricity used will be locally generated by 12 000 m^2 of solar panels. Other examples of projects in Europe are: Power-to-X project of Nature Energy in Denmark, with a gas production of 500 m^3 h^{-1}; MéthyCentre in France, with a methane production of 12.5 m^3 h^{-1}; and OCCI-BIOME by Arkolia, in France, with a methane production capacity between 50 and 100 m^3 h^{-1} [8].

1.2 Objectives

Given the role that biomethane can play in the energy transition, the objective of this work will be to develop computational models to dynamically simulate a biomethane production in a biogas

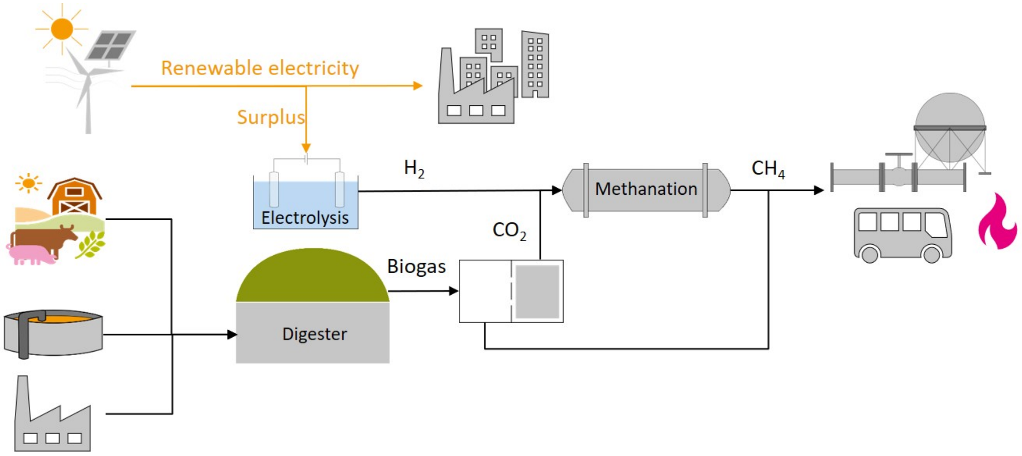

Figure 1.4: Scheme of a P2G system using CO_2 from biogas.

plant combined with a catalytic methanation reactor in a P2G approach. The produced gas should meet the grid injection specifications. Although these values may vary from country to country, the specifications for injection into the French natural gas grid were adopted in this work (Table 1.1) [15].

Table 1.1: Gas quality requirement for grid injection in France.

Parameter	Specification
Higher heating value	Gas type H: 10.7-12.8 kWh Nm^{-3} Gas type B: 9.5-10.5 kWh Nm^{-3}
H_2S	< 5 mg S Nm^{-3}
CO_2	$< 2.5\%$
H_2	$< 6\%$
CO	$< 2\%$

As the majority of biogas digesters in France use agricultural biomasses as feedstock, which corrspond to the biogas plant type that will be modeled in this thesis. Besides, to reach the injection requirements, the CO_2 present in biogas should be separated. Therefore, cleaning and upgrading units of the biogas plant will also be included in the modeling work. Then, all these models will be integrated and used to simulate the whole system, including the biogas plant and the P2G plant. These simulations will be used to evaluate the operation of such multi-energy platform and identify possible synergies between the process units.

This PhD manuscript is structured as follows: in Chapter 2, the technologies and modeling approaches used in biogas and P2G context are presented; in Chapter 3, a biogas plant in Italy is assessed in terms of energy and environmental performance; in Chapter 4, the digester model is developed and validated against experimental data; in Chapter 5, the auxiliary models used to simulate biomethane and P2G plants are described; and in Chapter 6, these models are used in several study cases.

CHAPTER 2

INTRODUCTION AND LITERATURE REVIEW

Anaerobic digestion is a complex process that comprehends a number of bioreactions. Besides, concerning the available biogas technologies, there are several options of digester types and biogas treatment routes. This Chapter presents an overview on the anaerobic digestion process and the available technologies in the biogas industry. These information guided the modeling approach used throughout this work. Moreover, some approaches on P2G integration with biogas is explored at the end of this Chapter.

2.1 Anaerobic digestion

In short, anaerobic digestion (AD) consists in the biodegradation of organic matter in the absence of oxygen (i.e. anaerobic conditions). It can be represented by one general equation (Eq. 2.1) [16]. However, this process is not a simple one.

$$
\begin{aligned}
&C_cH_hO_oN_nS_s + yH_2O \rightarrow xCH_4 + nNH_3 + sH_2S + (c-x)CO_2 \qquad (2.1)\\
&x = \frac{1}{8}\left(4c + h - 2o - 3n - 2s\right)\\
&y = \frac{1}{4}\left(4c - h - 2o + 3n + 2s\right)
\end{aligned}
$$

In fact, AD comprehends a myriad of reactions carried out by hundreds of different bacteria and archaea [17]. These processes are commonly grouped into four steps: hydrolysis, acidogenesis, acetogenesis and methanogenesis (Figure 2.1). Similarly to a production chain, the product of each step is processed by the next one, until the last one, in which methane is produced.

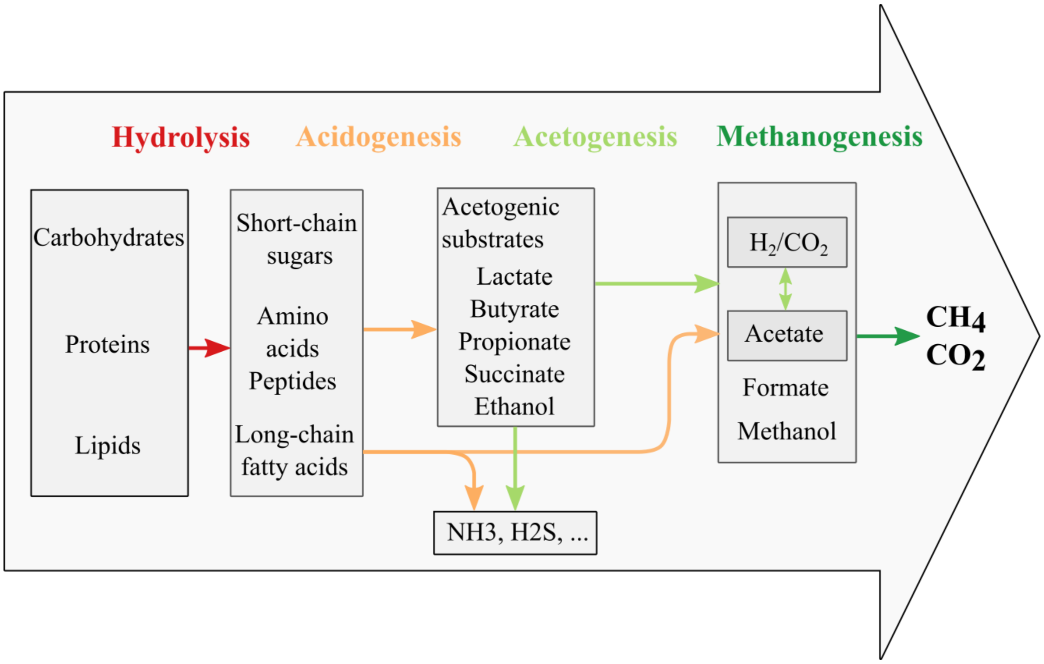

Figure 2.1: The four stages of anaerobic digestion.

2.1.1 Hydrolysis

In the hydrolysis phase, the macromolecules, which are biopolymers, are broken down to their monomers, solubilizing them as well (Eq. 2.2). Carbohydrates are reduced to sugars, proteins into amino acids, and lipids into fatty acids. This process is extracelular and is catalyzed by enzymes secreted by hydrolytic bacteria. The degradation kinetics depend on the organic matter composition. Carbohydrates are generally decomposed within a few hours, while proteins and lipids take a few days. Fibers, however, have a lower degradation rate. For instance, the hydrolysis of lignocellulose and lignin is slower and incomplete. Regarding the whole AD process, the hydrolysis is generally considered the rate-limiting step, but this depends on the composition of the organic matter.

$$RCCR + \mathbf{H_2O} \rightarrow RC\mathbf{OH} + \mathbf{H}CR \tag{2.2}$$

2.1.2 Acidogenesis

The molecules produced in the hydrolysis phase become the substrate of the acidogenic bacteria. They are degraded into organic acids, alcohols, hydrogen and carbon dioxide. As these acids have a short carbon chain, it is common to refer to them as volatile fatty acids (VFA) in the literature. The acidogenesis reactions take place inside the bacteria cells, and they are heavily influenced by their conditions. For instance, a high hydrogen partial pressure promotes the formation of organic acids with longer chains instead of acetic acid [16]. Using glucose as an example, there are several different products that can be obtained from it, which are shown in Table 2.1 [18].

Table 2.1: Possible products from acidogenesis of glucose [18].

Product	Reaction
Acetic acid	$C_6H_{12}O_6 + 2H_2O \rightarrow 2CH_3COOH + 2CO_2 + 4H_2$
Propionic acid	$C_6H_{12}O_6 + 2H_2 \rightarrow 2CH_3CH_2COOH + 2H_2O$
Acetic and propionic acids	$C_6H_{12}O_6 \rightarrow CH_3CH_2COOH + CH_3COOH + 2CO_2 + 2H_2$
Butyric acid	$C_6H_{12}O_6 \rightarrow CH_3\left(CH_2\right)_2COOH + 2CO_2 + 2H_2$
Ethanol	$C_6H_{12}O_6 \rightarrow 2CH_3CH2OH + 2CO_2$
Ethanol and acetic acid	$C_6H_{12}O_6 + H_2O \rightarrow CH_3CH_2OH + CH_3COOH + 2CO_2 + 2H_2$
Lactic acid	$C_6H_{12}O_6 \rightarrow 2CH_3CHOHCOOH$
Lactic acid and ethanol	$C_6H_{12}O_6 + H_2O \rightarrow CH_3CH_2OH + CH_3CHOHCOOH + 2CO_2$

2.1.3 Acetogenesis

In acetogenesis phase, the organic acids are converted to acetic and formic acid, releasing also H_2 and CO_2 [19]. In fact, acetogenic bacteria are mandatory H_2 producers. However, the reactions carried out by these microorganisms are only favorable at low hydrogen concentrations [16]. For this reason, the acetogenic bacteria live in syntrophy with methanogens, as the latter are H_2 consumers [16, 19], as it will be explained in the next section. The acetogenic reactions are shown in Table 2.2 [16].

Table 2.2: Acetogenic reactions [16].

Substrate	Reaction
Propionic acid	$CH_3\left(CH_2\right)COOH + 2H_2O \rightarrow CH_3COOH + CO_2 + 3H_2$
Butyric acid	$CH_3\left(CH_2\right)_2COOH + 2H_2O \rightarrow 2CH_3COOH + 2H_2$
Valeric acid	$CH_3\left(CH_2\right)_3COOH + 2H_2O \rightarrow CH_3COOH + CH_3CH_2COOH + 2H_2$
Isovaleric acid	$\left(CH_3\right)_2CHCH_2COOH + HCO_3H + H_2O \rightarrow 3CH_3COOH + H_2$
Capronic acid	$CH_3\left(CH_2\right)_4COOH + 4H_2O \rightarrow 3CH_3COOH + 5H_2$
CO_2/H_2	$2CO_2 + 4H_2 \rightarrow CH_3COOH + 2H_2O$
Glycerine	$C_3H_8O_3 + H_2O \rightarrow CH_3COOH + 3H_2 + CO_2$
Lactic acid	$CH_3CHOHCOOH + 2H_2O \rightarrow CH_3COOH + HCO_3H + 2H_2$
Ethanol	$CH_3\left(CH_2\right)OH + H_2O \rightarrow CH_3COOH + 2H_2$

2.1.4 Methanogenesis

The forth stage of AD is the methanogenesis. In this phase, acetic acid, formic acid and H_2 formed in the acetogenesis reactions are converted into methane by methanogenic archaea. Compared to the anterior group, methanogens require H_2 to survive. Thus, by living in syntrophy with acetogens, one group produces H_2 and the other one utilizes it, balancing it to achieve the survival of both microorganism groups. Among the methanogens, two groups are especially of interest in AD: acetoclastic methanogens and hydrogenotrophic methanogens. The difference between them corresponds to the substrate used. The former consumes acetate, and the latter hydrogen. In Table 2.3, the methanogenic reactions are shown [16].

Table 2.3: Methanogenic reactions [16].

Substrate	Reaction
CO_2	$CO_2 + 4H_2 \rightarrow CH_4 + 2H_2O$
Formate	$4HCOOH + H_2O \rightarrow CH_4 + 3HCO_3H$
Acetate	$CH_3COOH + H_2O \rightarrow CH_4 + HCO_3H$
Methanol	$CH_3OH + H_2 \rightarrow CH_4 + H_2O$
Ethanol	$2CH_3CH_2OH + CO_2 \rightarrow CH_4 + 2CH_3COOH$

2.2 Biogas technology

The processes in a biomethane plant can be separated into 3 categories: anaerobic digestion, biogas cleaning and biogas upgrading. In this Section, the available technologies for each one of these parts are analyzed. The objective here is to define the biomethane plant structure that will be used in the next parts of this work.

2.2.1 Digesters

The reactor in which the anaerobic digestion reactions take place is commonly called digester. The choice of which digester technology should be used depends on the process operating conditions, as for instance humidity and temperature, and the feedstock characteristics.

The temperature plays an important role in AD. It influences in a number of parameters, such as the digestion rate, the substrate solubility and the solution ionization equilibria, and most importantly, it selects the microorganism community that will carry out the bioreactions. There are three ranges of operating temperature: thermophilic (45-70 °C), mesophilic (20-40°C) and psychrophylic (4-15 °C). While, this process parameter defines mostly the necessity of heating or not the digester, the humidity, or alternatively total solids content (TS), is important to decide which type of digester should be used.

Initially, the digesters can be separated in two main groups: wet and dry digesters (Figure 2.2) [20]. The former then can be subdivided according to whether the microorganisms are grown suspended in the reaction medium or attached to a packing medium. The dry digester subcategories depend if the reactor is operated continuously or in batch. Dry digesters are recommended for feedstock with high TS content (TS >20). However, wet technologies can also be applied to these materials, but it requires diluting it with water or liquid digestate.

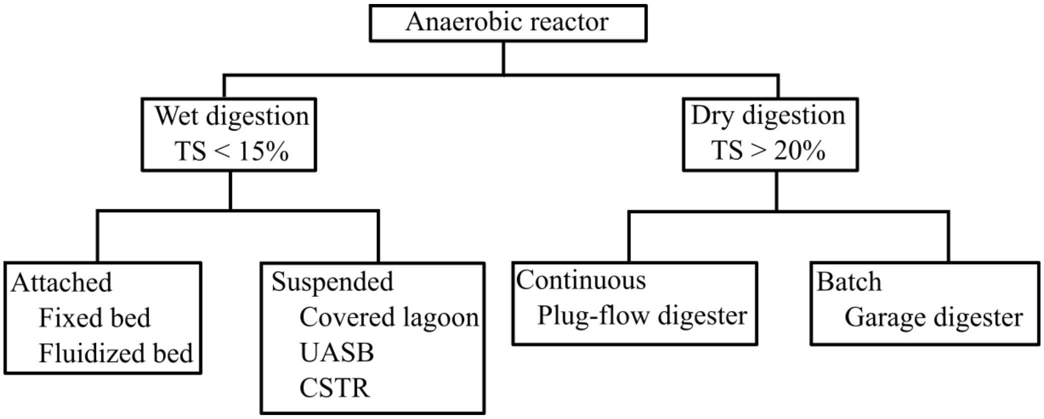

Figure 2.2: Classification of anaerobic digester. Adapted from [20].

Plug-flow digester

Plug-flow digesters can be either be vertical or horizontal (Figure 2.3). The first constitutes of a cylindrical tank in which the digestate can flow upwards or downwards, while horizontal reactors can also be structured as a rectangular ducts. The effluent flows continuously inside the reactor and part of it is recirculated.

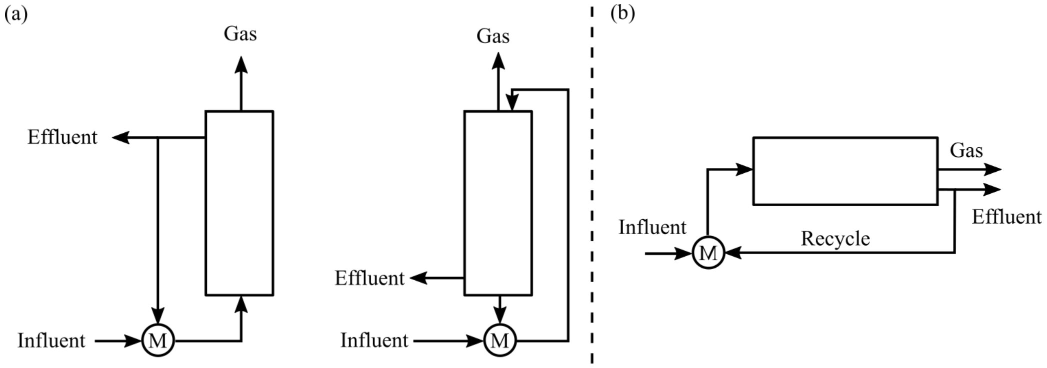

Figure 2.3: Vertical plug-flow digester (a) and horizontal plug-flow digester (b). Adapted from [20].

Garage digester

The garage digester is a batch dry digester that consists of a gas-tight chamber (Figure 2.4). During the digestion period, the leachate is continuously recirculated over the substrate and the biogas is collected from the headspace. Then, the reactor is unloaded and loaded with fresh matter. Part of the digestate is left inside the digester to serve as inoculum for the next batch. This type of digester can treat materials with up to 50% TS.

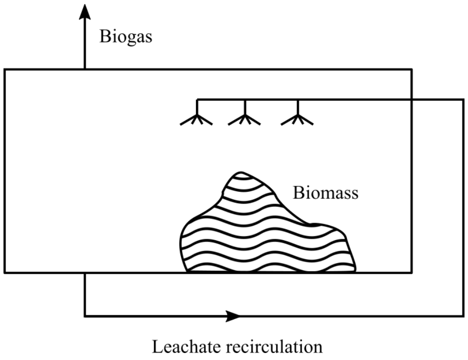

Figure 2.4: Garage digester. Adapted from [20].

Fixed and fluidized bed reactors

In these reactors, the microorganisms grow attached to an inert surface, which can be a fixed structure or suspended particles (Figure 2.5). In fixed bed reactors, the digestate flows through a filter impregnated with the biofilm, while in fluidized bed, the particles are kept in suspension due to an upwards influent injection. In both cases, the degradation occurs as the organic compounds enter in contact with the microorganisms. In anaerobic filter reactors, the solid retention time is between 1 and 10 days, and TS <5%, with an organic loading rate (OLR) of up to 16 kg of chemical oxygen demand (COD) m^3 d^{-1}. Alternatively, in the fluidized bed ones, the OLR is in the range 10-50 kg COD m^3 d^{-1}. These types of reactor have been used mostly in wastewater treatment [21].

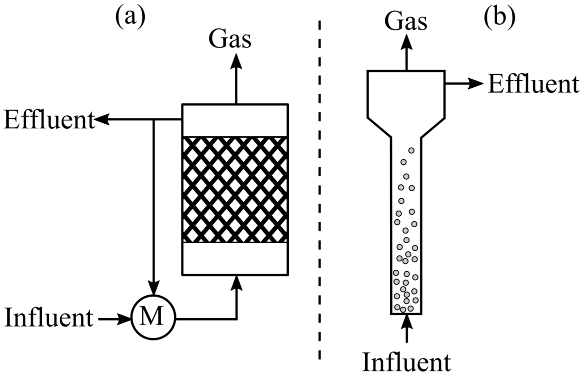

Figure 2.5: Fixed bed reactor (a) and fluidized bed reactor (b). Adapted from [20].

Covered lagoon

The covered lagoon is one example of a plug flow digester. It consists in a tank dug into the soil, which is then impermeabilized with a polymeric material (Figure 2.6). The biogas is stored and collected in the headspace, which is also delimited by a gas tight polymeric membrane. This type of digester has a low technological level and do not have a heating or mixing system. Generally, it is used in rural areas to treat animal wastes [19]. The material treated has a TS <3% and retention time can reach up to 100 days.

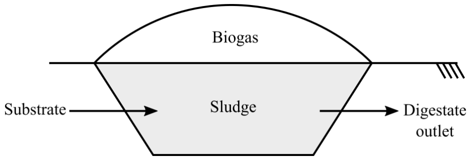

Figure 2.6: Covered lagoon reactor. Adapted from [19].

Upflow Anaerobic Sludge Blanket (UASB)

The UASB is a vertical reactor in which the substrate flows upward (Figure 2.7). The sludge concentration varies from a high density at the bottom, to a light one close to the top. The highest microbial activity is located on the fresh material feed side. The digestate and the biogas are collected at the top of the digester. This type of reactor operates with TS of up to 3%, a hydraulic retention time (HRT) of less thane 72 hours, solid retention time (SRT) in the range of 20-30 d, and OLR between 0.5 and 8.0 kg of volatile solids (VS) m^3 d^{-1}. This reactor has been used especially in the wastewater treatment sector.

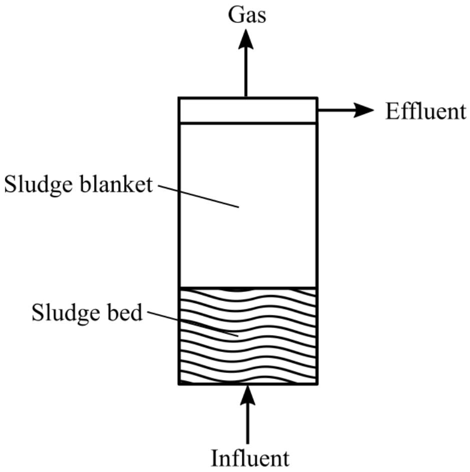

Figure 2.7: UASB reactor. Adapted from [21].

Continuous stirred-tank reactor (CSTR)

The CSTR is a tank where the biomass is kept in suspension by mixing (Figure 2.8). It is the most common digester type in Europe [19]. For instance, in the French region *Hauts-de-France*, more than 96% of installed digesters were of such type [22]. Mixing can be carried out by mechanical agitators or by digestate or biogas recirculation. The HRT is highly variable in these reactors, reaching up to more than 100 days in some applications. The OLR is tipically between 1 and 4 kg VS m^3 d^{-1} [19].

2.2.2 Biogas cleaning

The biogas leaves the digesters saturated in water. Besides, it also contains many other contaminants, such as H_2S, NH_3 and siloxanes (Table 2.4). Despite relative low concentrations of its impurities, removing them is important to avoid process problems, such as corrosion and mechanical wear [23]. Among impurities, the most relevant ones are water and hydrogen sulfide.

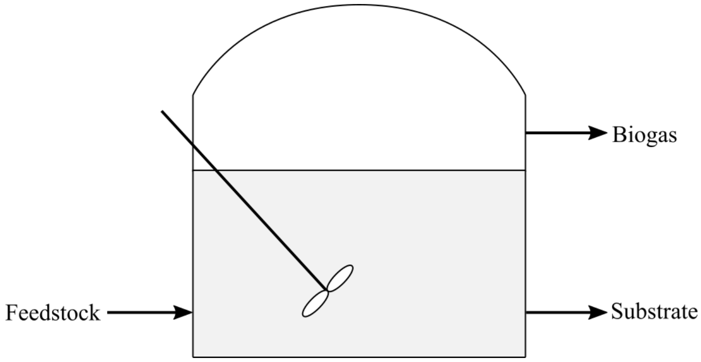

Figure 2.8: CSTR reactor.

Table 2.4: Typical composition (%) of raw biogas [24].

Compound	Agricultural biomass	Landfill	Industrial waste
Methane	50-80	50-80	50-70
Carbon dioxide	30-50	20-50	30-50
Hydrogen sulfide	0.7	0.1	0.8
Hydrogen	0-2	0-5	0-2
Nitrogen	0-1	0-3	0-1
Oxygen	0-1	0-1	0-1
Carbon monoxide	0-1	0-1	0-1
Ammonia	Traces	Traces	Traces
Siloxanes	Traces	Traces	Traces
Water	Saturation	Saturation	Saturation

Water should be removed from the biogas before its utilization in combustion engines or injection into the gas grid. Generally, this compound is the first one to be removed from biogas to avoid equipment and pipeline corrosion [19]. This is carried out by either cooling or compressing the gas stream. The former can be carried out in a chiller or in buried pipes with condensate traps, depending on the tolerance of water vapor content in the downstream units [19, 25].

Hydrogen sulfide is a relevant nuisance to the biogas process, as it is toxic and corrosive. Generally, its removal takes place in two phases: a rough and then a fine one. In the former, methods like biological desulfurization and iron chloride dosing are employed. Biological desulfurization consists in adding controlled amounts of oxygen or air to the biogas, thus this method is also known as microaeration. The oxygen allows the development of aerobic microorganisms that oxidize H_2S into elemental sulfur. The oxygen injection can be carried out using pure O_2 or air, and it can take place either directly in the digester headspace or in a dedicated unit, such as a biofilter. On the other hand, iron chloride dosing involves adding iron chloride to the digestate, which reacts with

H_2S in the liquid phase, leading to the precipitation of iron sulfide. These methods are said rough desulfurization because, despite removing up to 80% of H_2S from the biogas, the concentration of this compound is still too high to some applications, notably for grid injection.

In the fine phase, adsorption with activated carbon or iron oxide is generally used. A previous H_2S removal is recommended before these methods to avoid the saturation of the adsorption material and ease its regeneration [19]. While the adsorption with activated carbon is a physical process, the iron oxide one is based on the reaction between H_2S and the bed material, which leads the formation of iron sulfide. These methods are effective in reducing the H_2S concentration to levels below 5 ppm [19].

2.2.3 Biogas upgrading

After the cleaning stage, the clean biogas is basically constituted by CH_4 and CO_2. In the upgrading stage, the carbon dioxide is separated from biogas to produce biomethane. Several techniques can be employed for this separation. The main ones are: pressure swing adsorption (PSA), water scrubbing, chemical absorption, membrane separation and cryogenic distillation (Table 2.5).

Table 2.5: Overview of main biogas upgrading technologies.

	PSA	Water scrubber	Amine scrubber	Membrane separation	Cryogenic distillation	Sources
Biomethane purity (%)	90-99	80-99	98-99.9	90-99.5	98-99.9	[9, 26]
Methane losses (%)	1-5	0.5-3	0.1-0.5	0.1-4	0.1-2	[9, 26]
Electricity demand (kWh Nm^{-3})	0.16-0.43	0.2-0.5	0.05-0.25	0.18-0.35	0.18-1.5	[9, 26, 27, 28]
Operating pressure (bar)	1-10	4-10	0.05-4	7-20	10-50	[9, 28]
Fine desulfurization	Yes	No	Yes	Yes	Yes	[9, 27]

PSA is an adsorption separation method that relies on the different adsorption capacity under varying pressures. A PSA unit constitutes of 4-6 columns in parallel that have a cyclic operation [27]. In some of them, biogas is passed at high pressure, leading to the adsorption of CO_2 to the bed material. The other ones operate at a low pressure without biogas feed, which releases the CO_2, thus regenerating these adsorption columns.

Water and amine scrubbing are both absorption processes. The difference is that the former is a physical absorption, while the latter is a chemical one. Water absorption is based on the higher solubility of CO_2 in water compared to methane. In this unit, the biogas is passed through an absorption column, in which the carbon dioxide and other soluble compounds (e.g. H_2S) are transferred to the water stream. The absorbant is then regenerated by a pressure reduction and degassing using air [9]. After passing through the absorption column, the biomethane stream requires to be dried before being injected. The amine scrubbing process works in a similar way. However, the absorption process takes place by a chemical reaction between carbon dioxide and the absorbant, which is regenerated by heating [9]. The biomethane stream also needs to be dried after this separation unit.

Membrane separation is based on the permeability difference between CO_2 and CH_4 through polymer membranes. In this process, the biogas is pressurized and passed through a series of membrane stages, typically arranged in a three-stage configuration in modern plants [29]. In the permeate, a CO_2-rich gas is obtained, while a CH_4 is obtained in the retentate. Over the last years, the cost of membrane units has significantly decreased, making it one of the most cost-effective biogas upgrading technologies available [30]. Consequently, its use in biogas plants has significantly increased. For instance, in 2021, this technology was used in 84% of biomethane plants in France (Figure 2.9) [31].

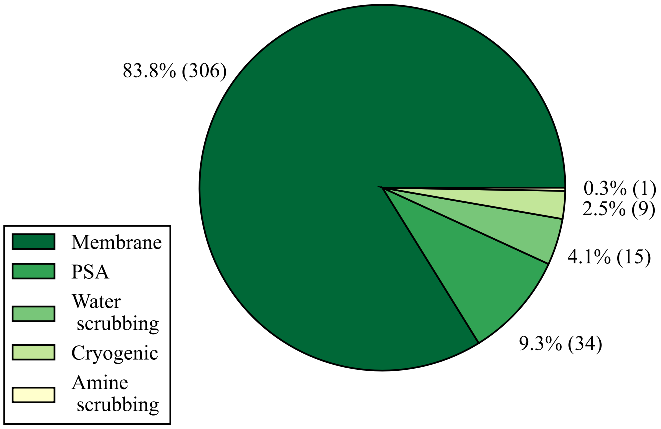

Figure 2.9: Upgrading techonologies used in French biomethane plants in 2021 [31].

Cryogenic distillation involves compressing and cooling the biogas to condensate and separate its compounds. This process yields high-purity biomethane and liquid CO_2 as by-products, which can be sold to other industries [28]. This technology is particularly interesting to produce liquefied biomethane. However, its application is still limited due to its high energy consumption, despite recent advancements that managed to considerably reduce this power demand [28].

2.3 Anaerobic digestion modeling

The AD process can be mathematically described with several approaches, which range from simple empirical models to complex mechanistic ones [32]. Empirical models are based on statistical correlations derived from experimental data. On the other hand, mechanistic models represent the biochemical reactions occurring inside the digester to estimate the biogas production. Thus, differently from the former group, the latter category incorporates several physical parameters of the reactor, such as substrate concentration, microbial growth rates and temperature [18, 32]. Although empirical models can be useful for a number of applications, such as process control for example, the focus here is given to mechanistic ones.

Among them, the Anaerobic Digestion Model N°1 (ADM1) stands out as the most widely used in the literature [18, 32, 33, 34]. Since its release in 2002, it has become the benchmark for AD modeling. In fact, it was the result of a task group that harmonized different AD modeling approaches. Although ADM1 was initially designed for wastewater treatment, it has since been applied to a range of other areas, including wastewater [35], urban waste [36], and agricultural residues [37, 38]. Fitting to other kind of feedstocks was generally carried out by re-estimating its parameters or changing its structure. For example, Ozgun [35] calibrated ADM1's parameters with experimental data from a full-scale sludge digester, while Koch *et al.* [37] added inert particles to consider the inert fraction of lignocellulosic fibers.

In a recent ADM1 modification, Weinrich and Nelles [39] enhanced its applicability to agricultural biomasses. This version, here noted as ADM1-W, presents a mass-based stoichiometry instead of using the chemical oxygen demand (COD). Besides, a systematic simplification was suggested, with four different levels of complexity, which can be used according to the intended use.

Other mechanistic model that has a similar complexity level as the ADM1 is the BioModel. Its original version was released in 1993 [40], with a relevant update four years later [41]. Although the BioModel is one of the approaches that led to the development of ADM1, this earlier model is more focused on manure-based systems. In the last years, this model has also received several improvements. Kovalovszki *et al.* [42] expanded the model application to various co-digestion scenarios.

Then, hydrogenotrophic methanogenesis was added to simulate a biomethanation scenario [43]. In addition, Kegl and Kovač Kralj [44] integrated three-phase (gas-liquid-solid) physico-chemical processes, such as precipitation and dissolution reactions, into BioModel.

ADM1

Due to its acceptability and extensive application in AD modeling, the ADM1 was used as base model for this work. This section provides a brief overview of the original version [33]. Then, the changes proposd by Weinrich and Nelles [39], ADM1-W, are presented. Our work is based on this modified version.

In the ADM1, the digestion process is separated in five phases: composite disintegration, hydrolysis, acidogenesis, acetogenesis, and methanogenesis (Figure 2.10). In the first step, composite particulates are broken down to particulates of proteins, carbohydrates, lipids, and inert compounds. These individual particulates are then hydrolyzed into their respective monomers. Then, in the acidogenesis, these monomers are converted into VFAs, H_2 and CO_2. The VFAs considered in ADM1 are: propionic acid (HPr), butyric acid (HBu), and valeric acid (HVa). In acetogenesis, these compounds are converted into acetate, CO_2 and H_2. The last step includes both the acetoclastic and the hydrogenotrophic methanogens. Therefore, acetate and H_2 are transformed into methane in this stage. Inorganic carbon (IC) and nitrogen (IN) are also included to consider the ammonia uptake and the CO_2 release by microorganisms. These two compounds play also a significant role as pH buffer in the digestate.

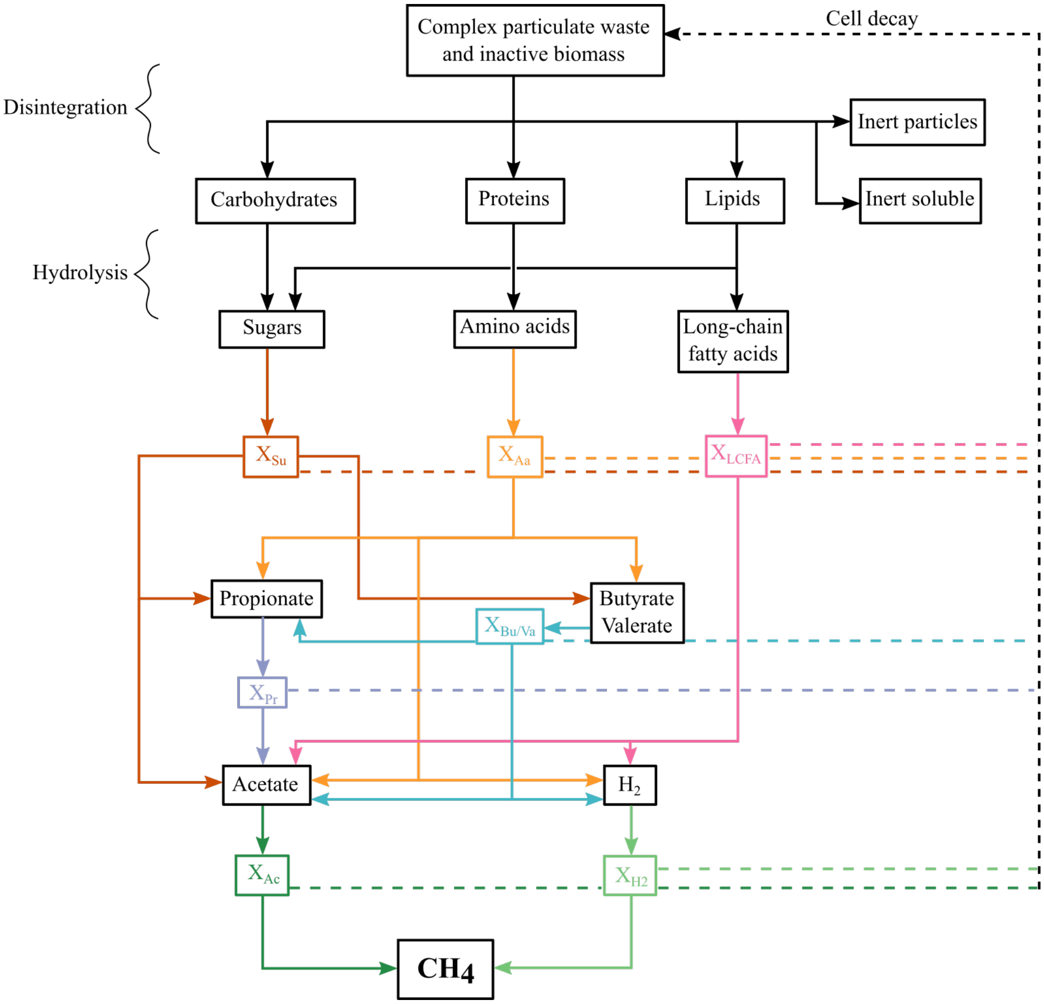

Figure 2.10: AD biochemical reactions of ADM1. The colored elements indicate the bioreactions: acidogenesis from sugars (X_{Su}); acidogenesis from amino acids (X_{Aa}); acidogenesis from LCFA (X_{LCFA}); acetogenesis from propionate (X_{Pr}); acetogenesis from butyrate and valerate ($X_{Bu/Va}$); aceticlastic methanogenesis (X_{Ac}); and hydrogenotrophic methanogenesis (X_{H2}). Adapted from [45].

The reaction rates are calculated in terms of substrate uptake. As a general form, the rate of reaction j is calculated as the product of the uninhibited rate, $r_{j,max}$, and its inhibition factors (Eq. 2.3). The microorganism biomass growth is calculated as a function of the substrate uptake by including a yield coefficient. The concentrations of organic compounds are expressed in terms of COD, while inorganic ones (e.g. carbon and nitrogen) are expressed in molar basis. IC, IN and VFAs are used to estimate the pH with a charge balance within the solution, which also include anions (AN) and cations (CAT) (Eq. 2.4). In Eq. 2.4, the concentrations are expressed in molar basis.

$$r_j = r_{j,max} I_{j1} I_{j2} I_{j3} \tag{2.3}$$

$$C_{CAT^+} + C_{NH_4^+} + C_{H^+} - C_{HCO_3^-} - C_{Ac^-} - C_{Pr^-} - C_{Bu^-} - C_{Va^-} - \frac{K_W}{C_{H^+}} - C_{AN^-} = 0 \tag{2.4}$$

The inhibition factors include non-competitive inhibition for hydrogen and free ammonia (Eq. 2.5), co-substrate limitation for total ammonia (Eq. 2.6), and pH inhibition (Eq. 2.7).

$$I_1 = \frac{1}{1 + \frac{C_l}{K_l}},\ l = H_2 \text{ or } NH_{3,free} \tag{2.5}$$

$$I_2 = \frac{C_{IN}}{C_{IN} + K_{IN}} \tag{2.6}$$

$$I_3 = \frac{1 + 2 \cdot 10^{0.5(pH_{LL} - pH_{UL})}}{1 + 10^{pH - pH_{UL}} + 10^{pH_{LL} - pH}} \tag{2.7}$$

The composite disintegration, macromolecules hydrolysis and cell decay were described using a first-order kinetics. On the other hand, the other bioreactions used a Monod equation. Eq. 2.8 represents the Monod-type kinetics, where $k_{max,j}$ is the maximum substrate uptake rate, C_i the substrate concentration and $K_{s,i}$ its half-saturation constant.

$$r_{j,max} = k_{max,j} \frac{C_i}{K_{s,i} + C_i} \tag{2.8}$$

H_2, CO_2 and CH_4 are assumed to be produced in liquid phase and then transferred to the gas phase using a mass transfer equation (Eq. 2.9). In addition, the water vapor concentration is supposed to be at its saturation level.

$$F_i^{GL} = k_L a \left(C_i^L - K_{Hi} P_i \right) \tag{2.9}$$

In comparison, ADM1-W converted all compounds and reaction rates to a mass-basis format. Besides, instead of representing the rates in terms of substrate uptake, Weinrich and Nelles [39] expressed them as cell growth rates. To achieve a stoichiometric balance in all equations, the compounds without a known molecular composition were removed, which includes, the composite particulate and the inert particles. Therefore, the disintegration step of ADM1 was removed. Its kinetic effect was integrated into the kinetic constants of the hydrolysis reactions. Besides, the pH inhibition factor was calculated with Hill functions instead (Eq. 2.10). Despite the efforts in adapting all ADM1's stoichiometries, the cell decay reaction still presented a slight atomic unbalance (Eq. 2.11, as in [39]). A more complete description of ADM1-W will be presented in Chapter 4.

$$\begin{aligned} I &= \frac{K_{pH}^n}{K_{pH}^n + C_{H+}^n} \\ n &= \frac{3}{pH_{UL} - pH_{LL}} \\ K_{ph} &= 10^{-\frac{pH_{UL}+pH_{LL}}{2}} \end{aligned} \tag{2.10}$$

$$C_5H_7O_2N \rightarrow 0.126\, C_6H_{10}O_5 + 0.997\, C_4H_{6.1}O_{1.2}N + 0.007\, C_{51}H_{98}O_6 \tag{2.11}$$

2.4 Thermal modeling

Due to the large size of industrial-scale anaerobic digesters, the heat losses from these reactors can be important. Indeed, the self-consumption of biogas to provide this thermal energy can reach up to 15% depending on the digester's structure and weather conditions [46, 47]. Thus, reducing theses losses is of paramount importance to improve the performance of biogas plants. For this reason, modeling also the digester's thermal aspect is required to properly represent the energy flows within such system.

Different approaches have been used to evaluate the thermal behavior of anaerobic digesters. Teleszewski and Żukowski [48] described the heat losses through digester's structures using an overall heat transfer coefficient. In other studies, the energy flows through the digester's structure was computed using a heat resistance network, with a dynamic energy balance on the digestate [49, 50]. This approach, however, does not take into account the thermal inertia of structural bodies. This aspect was addressed by Avila-Lopez *et al.* [47] by including also the structure in the differential energy balances. Indeed, they developed a comprehensive thermal model that included the different heat transfer forms (advection, convection, conduction and radiation) inside and through the digester's boundaries as a function of weather conditions [47].

Calise *et al.* [36] combined a simplified ADM1 version with a thermal model based on the logarithmic mean temperature difference (LMTD) method. Then, in a later work, they improved the thermal model by replacing the LMTD method by an energy balance on the digestate, replacing thus the steady state assumption of their previous work [51]. This led to a significant difference in biogas production, suggesting that a good prediction of the temperature dynamics has an important effect on the evaluation of the bioreactions yields [51]. In these studies, the thermal model was quite simple compared to others available in the literature [47, 49, 50, 52]. Therefore, the integration of thermal and kinetic modeling has not been fully explored yet.

2.5 AD and catalytic methanation integration

In the literature, there are few works that performed dynamic simulations of a P2G system including AD and catalytic methanation. In some cases, the stream coming from the biogas plant was adopted with constant flow rate and composition [53] or with data from an existing plant [54]. In contrast, Calise *et al.* [55] developed a dynamic model for a P2G system including a catalytic methanation reactor, a biogas digester and an electrolyzer to perform a thermoeconomic evaluation of such multi-energy platform. In this first work, they employed simplified models. For instance, the methanation reactor was described only using a plug-flow model to calculate the mass balance in such unit. However, in a later work, Calise *et al.* [56] adopted a more advanced model that included mass, energy and momentum conservation equations [57]. These studies have focused on evaluating the P2G system in terms of environmental benefit [53, 56], economic performance Calise *et al.* [55], or energy conversion efficiency Calise *et al.* [55, 56]. However, the possible synergies between the biogas and the P2G systems have not been evaluated.

2.6 Conclusions

The survey on biogas installations revealed that the CSTR digester is the most common in Europe and in France. In addition, the majority of biogas plants use feedstocks originated from agriculture or livestock activity. Regarding the technology employed to upgrade biogas into biomethane, membrane separators are widely used in France.

Concerning the modeling approaches, the ADM1 is the mainstream approach for bioreactions description in AD systems, with a good acceptability in the scientific community. In addition, a modified version of ADM1 that is more suitable for agricultural systems have already been developed [39]. Comprehensive thermal models for agricultural digesters are also available in the literature [47]. These works capture the effects of weather conditions and digester structure in the heat losses evaluation. The coupling of these two aspects (kinetics and thermal) has not been thoroughly explored yet. For this reason, a dynamic model that combines this complex kinetics and an advanced thermal model will be developed in this thesis.

The literature on coupling AD and catalytic methanation, however, is still much more limited, with few studies that coupled these two reactors. In this field, the possibilities on thermal integration in such platform has not been evaluated yet.

From the literature review, it was possible to define a typical biogas plant to be modeled and reference studies for kinetic and thermal modeling. This unit consists of an agricultural biogas plant, with a CSTR digester and a membrane upgrading unit. Therefore, the works of Weinrich and Nelles [39] and of Avila-Lopez *et al.* [47] will be used as basis for the model development.

CHAPTER 3

TECHNICO-ENVIRONMENTAL EVALUATION OF A BIOMETHANE PLANT IN NORTHERN ITALY

The environmental benefits of a biogas plant is strongly influenced by its technical performance [11]. Thus, a comparative analysis between different biogas valorization routes were carried out in terms of energy efficiency and carbon footprint. An agricultural biomethane plant located in Northern Italy (*Cooperativa Speranza*' biogas plant) was used as reference to compare with two main biogas usages: biomethane obtained by membrane separation, and cogeneration in combined heat and power (CHP) engines.

3.1 *Cooperativa Speranza*'s biogas plant (CSBP)

The biogas plant of Cooperativa Speranza is located in Candiolo (44°57'20.2"N, 7°34'06.5"E), province of Turin, Italy. It is composed of two concentric digesters with a total capacity of 14 000 m^3, followed by one post-digester and a digestate storage tank, both with a capacity of 6 100 m^3 each (Figure 3.1). The digesters operate under mesophilic conditions (40°C) with a hydraulic retention time (HRT) of around 130 days. The biomass intake is around 50 000 t $year^{-1}$. This feedstock consists of a mixture of cattle slurry and manure, and silage of energy crops (sorghum and triticale) and crop residues from several farms that are part of the *Cooperativa Speranza* (Table 3.1).

The desulfurization of biogas is carried out by oxygen microinjection inside the digesters' headspace and by adsorption in activated carbon filters. The oxygen used is produced in-situ in an air separation unit. The clean biogas is then upgraded into liquified biomethane (Bio-LNG) by cryogenic separation (CRYO), and is used as fuel for heavy trucks. As a co-product of the upgrading process, liquified CO_2 (LCO2) is also obtained and it is sold to a beverage company. The cryogenic distillation process is the main electricity consumer of the system, as it involves compressing biogas up to 40 bar and cooling it up to – 140°C.

The electricity demand of the system is partially met by internal production from solar photo-

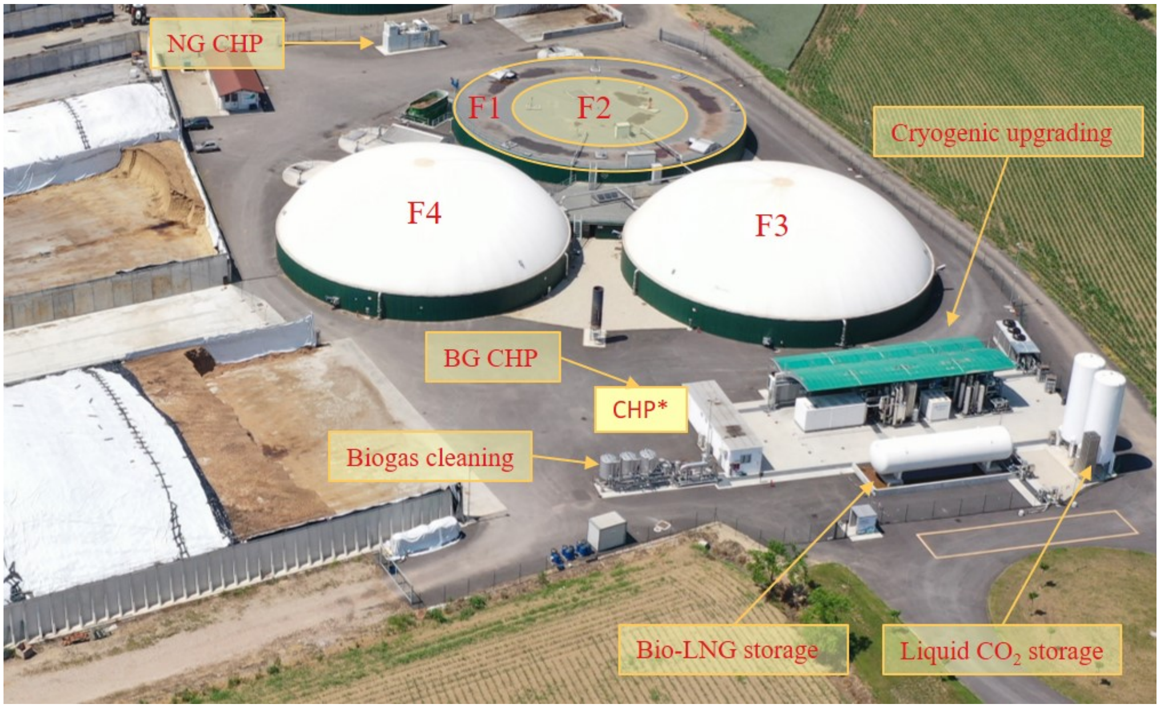

Figure 3.1: Aerial view of the biogas plant. It is indicated in the picture the digesters (F1 and F2), the post-digester (F3), the digestate storage (F4), the natural gas CHP (NG CHP), the biogas CHP (BG CHP), the biogas cleaning and upgrading units. *The moment the picture was taken, the BG CHP had not been installed yet.

voltaic panels (PV) and two CHP units: one powered by natural gas from the Italian gas grid (NG CHP) and the other one that uses biogas from the plant (BG CHP). The remaining part is bought from the national electric grid. The heat produced in CHPs and in the upgrading unit's compressors is recovered and, in addition to heating the digesters, is sold to a neighbor glass industry by a heat district system. To reduce the excess heat dissipated to the environment during summer, an absorption refrigeration system (ARS) was installed in the glass manufacturer. The ARS produces chilled water at a temperature of 7°C, by using the heat recovered from the biogas plant through absorption in a lithium bromide and water solution ($LiBr/H_2O$).

Specifications and monthly values of inputs and outputs of CSBP for the year 2023 were obtained from the plant manager, except for the biomass intake data which were provided by the plant owners. In Table 3.2, it is presented the monthly electricity sources and sinks in CSBP. While, in Table 3.3, the main plant outputs and dry biogas production are shown. The plant manager also provided the CHPs' electric and thermal efficiencies, which are respectively 35.8% and 45.5% for

Table 3.1: Biomas input in CSBP during 2023.

	Monthly biomass input [t]							
Month	Slurry	Manure	Sorghum[a]	Triticale[a]	Olive pomace	Shelled corn[b]	Corn cob[b]	Corn stalk[b]
1	2 492	327	475	0	0	142	519	61
2	1 909	292	374	0	0	112	409	48
3	2 770	348	393	0	0	118	430	50
4	2 801	439	453	0	0	136	495	58
5	2 496	310	394	0	0	118	431	51
6	2 273	452	297	0	0	89	325	38
7	3 286	475	299	0	0	90	327	38
8	3 600	470	541	0	0	87	252	28
9	3 387	308	0	908	0	0	0	0
10	3 259	437	0	1 031	142	0	0	0
11	3 553	365	461	420	185	26	95	0
12	3 486	437	890	0	0	50	184	0

[a] Energy crops produced in double-cropping system

[b] Crop residues

NG CHP, and 38.5% and 43.6% for BG CHP. Thus, the heat produced in each cogeneration unit was calculated from their electricity production. The thermal power recovered from the upgrading unit was approximately 80 kW throughout the whole year. Although the digesters' thermal energy consumption was not monitored, the plant manager estimated it to be 80 kW in summer and 380 kW in winter. Therefore, the heating power, Q_{DIG}, was estimated for each month, m, using a cosine function with its maximum in February and its minimum in August (Eq. 3.1). A scheme of the system boundary for CSBP considered in energy and environmental analyses is shown in Figure 3.2.

$$Q_{DIG} = 150\, cos \left(\frac{(m-2)\,\pi}{6} \right) + 230 \tag{3.1}$$

Table 3.2: Electric energy input and consumption in CSBP during 2023.

	Source [kWh$_{el}$]				Consumption [kWh$_{el}$]		
Month	NG CHP	BG CHP	PV	Grid	Digesters[a]	ARS	CRYO
1	245 290	26 350	9 278	10 457	30 666	0	213 472
2	209 573	95 592	13 921	10 120	28 563	0	188 728
3	212 278	103 186	22 167	18 630	32 190	0	206 249
4	238 937	110 689	27 830	13 454	31 467	0	271 746
5	226 973	108 524	25 538	23 634	39 512	0	318 483
6	228 257	30 928	26 984	88 469	39 938	1 584	304 484
7	249 466	65 205	30 702	81 634	38 569	5 906	341 431
8	253 971	49 549	26 941	102 040	39 731	619	333 919
9	248 515	8 257	22 067	128 156	37 504	2 789	328 878
10	259 881	54 407	15 072	86 464	36 509	27	345 464
11	238 876	87 733	12 985	37 994	27 775	0	331 292
12	249 240	112 714	8 914	28 069	31 126	0	349 400

[a] Stirring, pumping and production of O_2 for desulfurization

Table 3.3: CSBP's outputs and biogas production during 2023.

	Outputs				Biogas production		
Month	Bio-LNG [kg]	LCO2 [kg]	Heat [kWh]	Cold [kWh]	Volume [Nm^3]	CH_4 [%]	CO_2 [%]
1	157 690	257 870	8	0	395 561	52.6	47.1
2	119 270	243 850	12 706	0	337 188	53.1	46.7
3	157 330	192 750	12 115	0	346 663	52.4	47.1
4	146 400	304 510	3 279	0	477 620	51.0	48.6
5	134 350	287 050	342	0	398 759	51.5	48.1
6	138 932	230 680	0	35 816	398 667	52.0	47.3
7	182 529	325 750	0	133 441	503 798	51.6	47.7
8	180 233	282 900	0	19 731	505 120	51.6	47.6
9	183 220	292 120	0	64 118	497 680	51.5	47.5
10	195 621	274 950	0	545	512 770	52.0	47.5
11	124 895	322 740	28 810	0	478 710	52.2	47.6
12	133 234	303 630	67 020	0	528 280	51.7	48.1

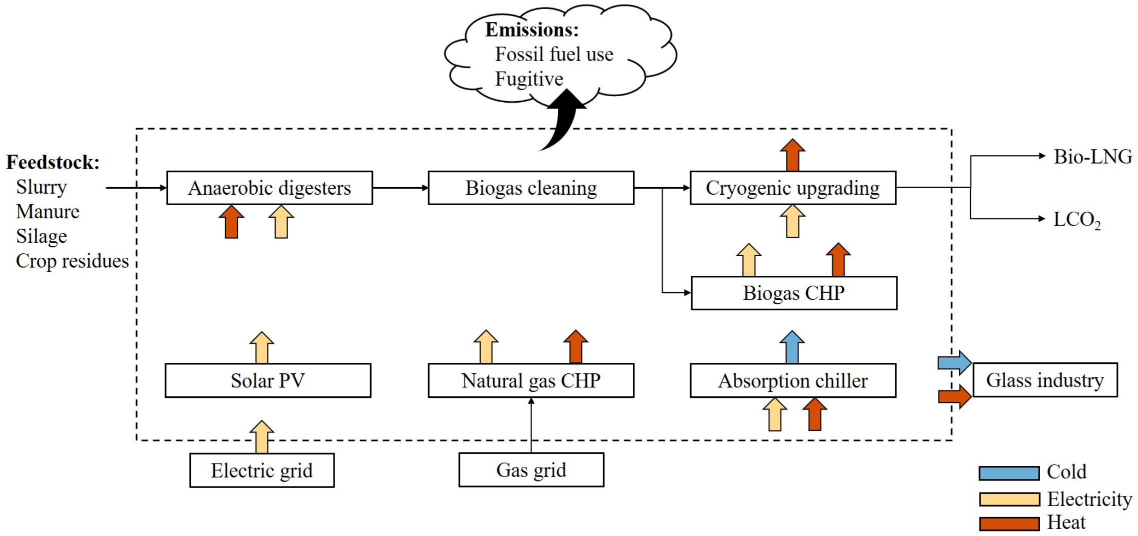

Figure 3.2: Process scheme of CSBP. The dotted line delimits the system boundary and, in each box, arrows entering corresponds to inputs and exiting to ouputs.

3.2 Hypothetical scenarios

To compare the performance of CSBP, two alternative scenarios for biogas valorization were developed. These two hypothetical cases represent classical usages of biogas. The first one corresponds to the heat and power cogeneration in a CHP engine, which will be referred as COGEN. The second one refers to a biogas upgrading to biomethane through membrane separation, which will be referred as MEM. In both cases, it was considered that the biogas digesters would be identical as in CSBP.

3.2.1 Biogas CHP

In this hypothetical scenario, the biogas is sent to a CHP unit, where it is used to cogenerate heat and electricity. (Figure 3.3). The thermal energy produced in the CHP was supposed to be used to heat the digester, and its surplus was sold to the glass industry according to its demand, which was assumed to be the same as in CSBP. However, as there is not the ARS in this case, no heat could be exported from June to October, when the neighbor industry only required chilled water.

The CHP's outputs were calculated considering the same efficiencies of CSBP's BG CHP. The biogas production was also taken as the same of the reference case (Table 3.3) and a LHV of 50 MJ

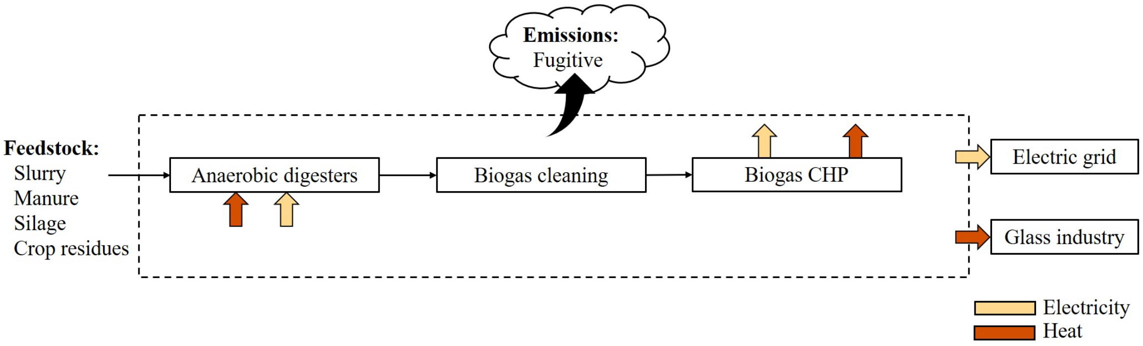

Figure 3.3: Process scheme of COGEN. The dotted line delimits the system boundary and, in each box, arrows entering corresponds to inputs and exiting to ouputs.

kg^{-1} was adopted for methane. The energy produced and sold in this case are exhibited in Table 3.4.

Table 3.4: COGEN's calculated production and outputs.

	Production in CHP		Sold	
Month	Electricity [kWh$_{el}$]	Heat [kWh$_{th}$]	Electricity [kWh$_{el}$]	Heat [kWh$_{th}$]
1	794 242	899 453	763 576	8
2	683 471	774 009	654 908	12 706
3	693 414	785 268	661 224	12 115
4	929 836	1 053 009	898 369	3 279
5	783 919	887 763	744 407	342
6	791 348	896 175	751 410	0
7	992 338	1 123 791	953 769	0
8	994 942	1 126 740	955 211	0
9	978 388	1 107 992	940 884	0
10	1 017 840	1 152 671	981 331	0
11	953 886	1 080 245	926 111	28 810
12	1 042 577	1 180 685	1 011 451	67 020

3.2.2 Membrane upgrading

In this scenario, the biogas was considered to be upgraded into biomethane using a membrane separation process and then injected into the gas grid. It was assumed that no thermal energy would be recovered in the upgrading unit. Therefore, the heat demand of digesters would be supplied by sending a fraction of the biogas produced into a boiler (Figure 3.4).

The biogas volume sent to do boiler was calculated considering a thermal efficiency of 0.82 [58]. In the membrane unit, the product gas was considered to have a purity of 97%, 1% of methane

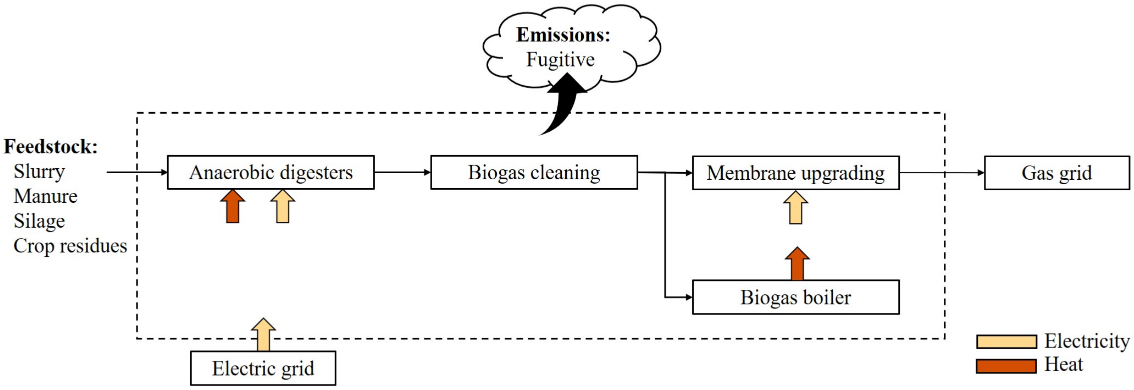

Figure 3.4: Process scheme of MEM. The dotted line delimits the system boundary and, in each box, arrows entering corresponds to inputs and exiting to ouputs.

loss in the lean gas and a specific electricity consumption of 0.30 kWh Nm^{-3} biogas [59]. The electricity consumption of membrane upgrading and the outputs of MEM are shown in Table 3.5.

Table 3.5: Membrane inputs in MEM and biomethane sent to the gas grid.

	Membrane input		Gas grid
Month	Electricity [kWh]	Biogas [Nm^3]	Biomethane [kg]
1	99 585	331 949	123 772
2	83 245	277 482	104 342
3	84 717	282 392	105 104
4	126 888	422 960	153 063
5	106 938	356 459	130 262
6	110 899	369 664	136 811
7	144 793	482 644	177 251
8	146 102	487 005	179 033
9	142 699	475 663	174 877
10	144 920	483 066	178 421
11	131 643	438 811	162 210
12	142 004	473 346	173 300

3.3 Energy efficiency

Each system was evaluated in terms of energy efficiency using the output-input ratio method, in which the energy content of the output is divided by the energy of all inputs [60]. Here, this efficiency was separated into three categories, z, to account for the different products of each study case: electric, fuel, and thermal (i.e. heat and cold) (Eqs. 3.2 and 3.3).

$$\eta_z = \frac{E_{out,z}}{\sum_i m_{f,i} LHV_i + \frac{E_{in,el}}{0.39} + m_{fuel} LHV_{fuel}} \tag{3.2}$$

$$\eta_{plant} = \sum_z \eta_z \tag{3.3}$$

Natural gas was assumed to be constituted by methane only. Thus, its LHV was also used as 50 MJ kg^{-1}. To evaluathe the energy content of each feedstock, a similar method used by Erol *et al.* [61] was employed. A linear correlation based on the ash content of the feedstock, ASH_i, was obtained through regression with agricultural biomasses from Phyllis2 database [62] (Eq. 3.4 and Figure 3.5). Compared to the work of Erol *et al.* [61], only ash content was used here as fixed carbon was not measured in the analyses done with the biogas plant biomasses. Besides, total and volatile solids did not have a significant correlation with LHV in the data from Phyllis2. Thus, Eq. 3.4 was used to evaluate the LHV of each feedstock used in the biogas plant (Table 3.6).

$$LHV_i = -0.1949 ASH_i + 18.916,\ R^2 = 0.84 \tag{3.4}$$

Table 3.6: Biomass composition and calculated lower heating values.

Biomass	TS [%]	ASH [% db]	LHV [MJ kg^{-1}]
Slurry	4.64	16.9	15.63
Manure	20.85	15.1	15.97
Sorghum	29.69	5.70	17.81
Triticale	35.25	6.15	17.72
Olive pomace	8.85	16.5	15.70
Shelled corn[a]	91	1.4	18.64
Corn cob	69.80	1.72	18.58
Corn stalk	35.99	4.38	18.06

[a] Composition from Phyllis2 [62]

Using the calculated energy content of each feedstock, the monthly η_{plant} was calculated for each case (Figure 3.6). During the year of 2023, the two biogas upgrading routes had similar values of energy efficiency. However, CSBP results were slightly superior to MEM. Indeed, the annual average of η_{plant} for CSBP, COGEN and MEM were respectively: 54.6%, 47.1% and 51.9%. The difference between CSBP and MEM can be explained in terms of heat production. In CSBP, part

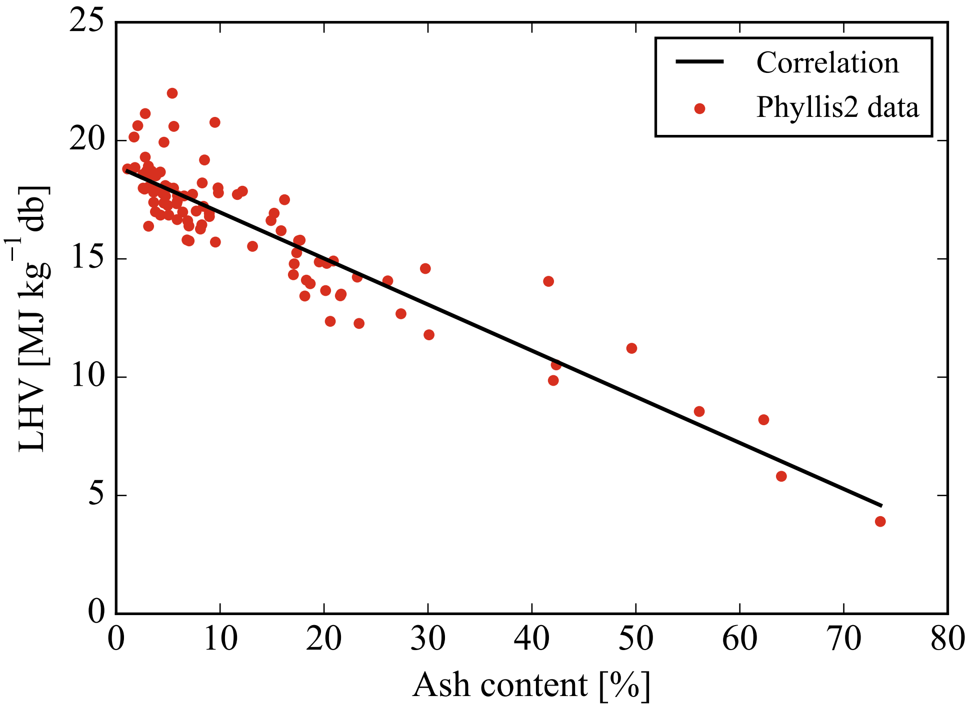

Figure 3.5: Lower heating value for different biomasses from Phyllis2 database [62].

of the biogas is used in a CHP unit, reducing biomethane output. However, this lower output was compensated by a lower electricity input and by the heat recovery in the cryogenic separation unit.

Regarding COGEN, even though the differences among the studied technologies were not elevated, a large fraction of energy output corresponded to heat (Table 3.4). However, only a small part of this thermal energy could be actually used (Figure 3.7). Indeed, the heat usage rates ranged from 18.1% in August to 66.8% in January in CSBP, while these values were between 5.3% and 35.6% in COGEN. This evidences the importance of having enough heat customers in case of large heat generation. For instance, in CSBP, the average heat use was 46.3% due to a relatively low heat demand in the neighbor industry and to the absence of another heat consumer. In COGEN, this was more noticeable, as only 18.2% of 12 000 MWh year^{-1} of thermal energy could be valorized.

Besides that, in many cases, thermal energy demand can be subjected to seasonal variations. Therefore, technologies that allow converting heat to cold can be useful in improving the thermal energy usage. For instance in CSBP, the ARS delivered 253 651 kWh of cool water to the glass industry, which resulted in an augmentation of up to 29.6% in heat usage in Summer (Figure 3.7).

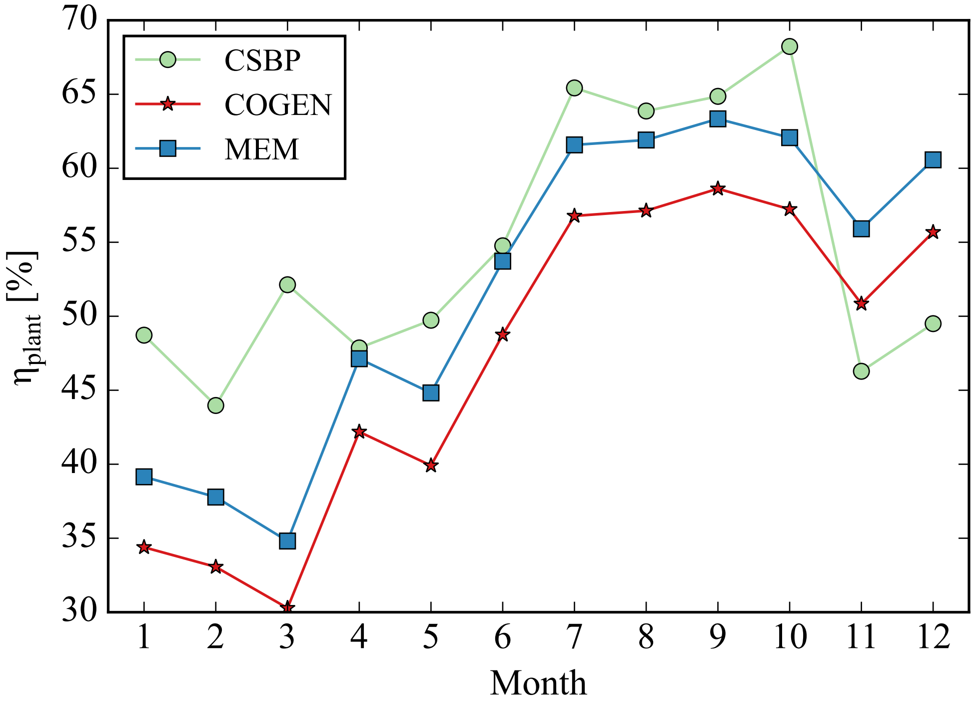

Figure 3.6: Monthly energy efficiency for each study case.

3.4 Environmental evaluation

A carbon footprint (CF) analysis was used to evaluate the environmental performance of each scenario. This kind of study is similar to a LCA, but it is focused in only one indicator: global warming potential (GWP), which is measured in kg CO_2 equivalents (kg CO_2-eq). This analysis was carried out considering the whole year of 2023.

Therefore, to calculate the inventories of each case, the values of inputs, outputs and emissions were summed for the entire year. 1 kg of CH_4 in clean biogas (kg CH_4-bg) was adopted as functional unit. This choice was made because the main product of each biogas valorization route is different. For instance, CSBP produces Bio-LNG, while COGEN produces heat and electricity. Besides that, as the digestion part was kept constant in all scenarios, this analysis quantifies the environmental impact of different biogas utilization means for the same amount of untreated biogas.

Based on the monthly inputs and outputs, the inventory of each scenario was calculated for the whole year of 2023 (Table 3.7). Regarding the biomass used, only the energy crops were considered

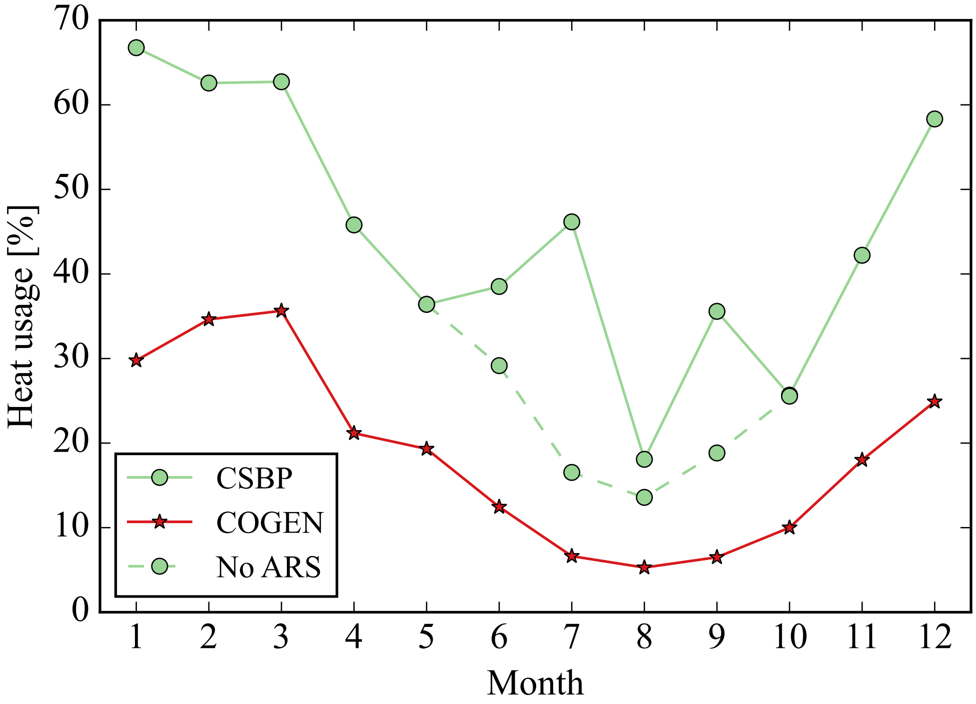

Figure 3.7: Monthly heat usage in CSBP and in COGEN. The heat usage in CSBP without ARS is shown with dotted lines.

in the inventory. The other feedstocks consisted of crop wastes, and, therefore, they were considered to be burden-free, following the cut-off method [63]. The nitrogen, phosphorous and potassium content of the digestate were obtained from chemical analyses carried out by the plant owners.

The emissions for each study case were estimated using emission factors from Ecoinvent database [67] mainly (Table 3.8). Alternatively, the values published by the Italian Environmental Agency (*Istituto superiore per la protezione e la ricerca ambientale* - ISPRA) were used for heat and electricity in Italy [68, 69]. For direct emissions (fossil CO_2 and fossil and biogenic CH_4), the values suggested by the Intergovernmental Panel on Climate Change (IPCC) were used [70].

The emissions of products were accounted as avoided emissions, which were included as negative values in the carbon footprint balance. These avoided emissions correspond to the GWP of an equivalent alternative. Heat and cold supplied to the neighbor industry could be replaced by an *in-situ* production. Thus, their emissions were taken as the ones to produce the same amount of heat or cold. More specifically to CSBP, the Bio-LNG would be replaced as truck fuel by diesel.

This was considered by taking the equivalent energy content of both fuels, including also a ratio of 0.79 between the energy efficiency of LNG and diesel engines [71, 72]. LCO2 was considered to be replaced by liquid CO_2 from Ecoinvent database. For COGEN, the electricity produced was considered to be injected to the grid, thus the emission factor of Italian electric grid was used. Finally, for MEM, as the biomethane would be injected into the gas grid, the value that corresponds to Italian natural gas was used. The use of digestate as fertilizer was accounted by taking a fertilizer substitute for each key nutrients in digestate (i.e. N, P_5O_2 and K_2O) and a 75% substitution efficiency of digestate compared to chemical fertilizers [73].

All the three scenarios yielded negative net emissions, exhibiting thus an environmental benefit regarding GWP (Figure 3.8). CSBP had, at the same time, the lowest value of net emissions and the highest positive emissions due to especially the use of natural gas in heat and power cogeneration. This fossil fuel use, however, was compensated by a higher Bio-LNG output and CO_2 valorization, which corresponded respectively to 66.7% and 24.1% of avoided emissions.

Although COGEN had the lowest posive emissions, its environmental performance depends strongly on the energy mix that constitutes the electricity production. Indeed, its positive emissions corresponded to around a third of those of CSBP. Taking the emission factor of electricity in France, for instance, which has a low GWP due to a major power fraction produced by nuclear plants, the net emissions of COGEN would drastically increase from -1.95 to -0.27 kg CO_2-eq. Besides, in this particular case, the heat exported corresponded to only a small fraction of the amount produced. If all thermal energy available could sold, net emissions would be reduced by up to -1.05 kg CO_2-eq kg^{-1} CH_4-bg, showing that heat recovery is also important for the environmental performance of heat and power cogeneration.

In the scenario with membrane upgrading, positive emissions were at an intermediary level between CSBP and COGEN, with a value 41.8% lower than the former. Despite of that, in absolute values, MEM's net emissions were only 11.3% lower than the one of CSBP, which indicates that the alternative with membrane upgrading can reach a similar level of environmental performance with lower emissions. The main difference between the upgrading routes came from CO_2 valorization in CSBP. Without it, the net emissions of this scenario would be at around -1.9 kg CO_2-eq kg^{-1} CH_4-bg, at the same level of COGEN. Therefore, implementing an alternative to valorize such gas

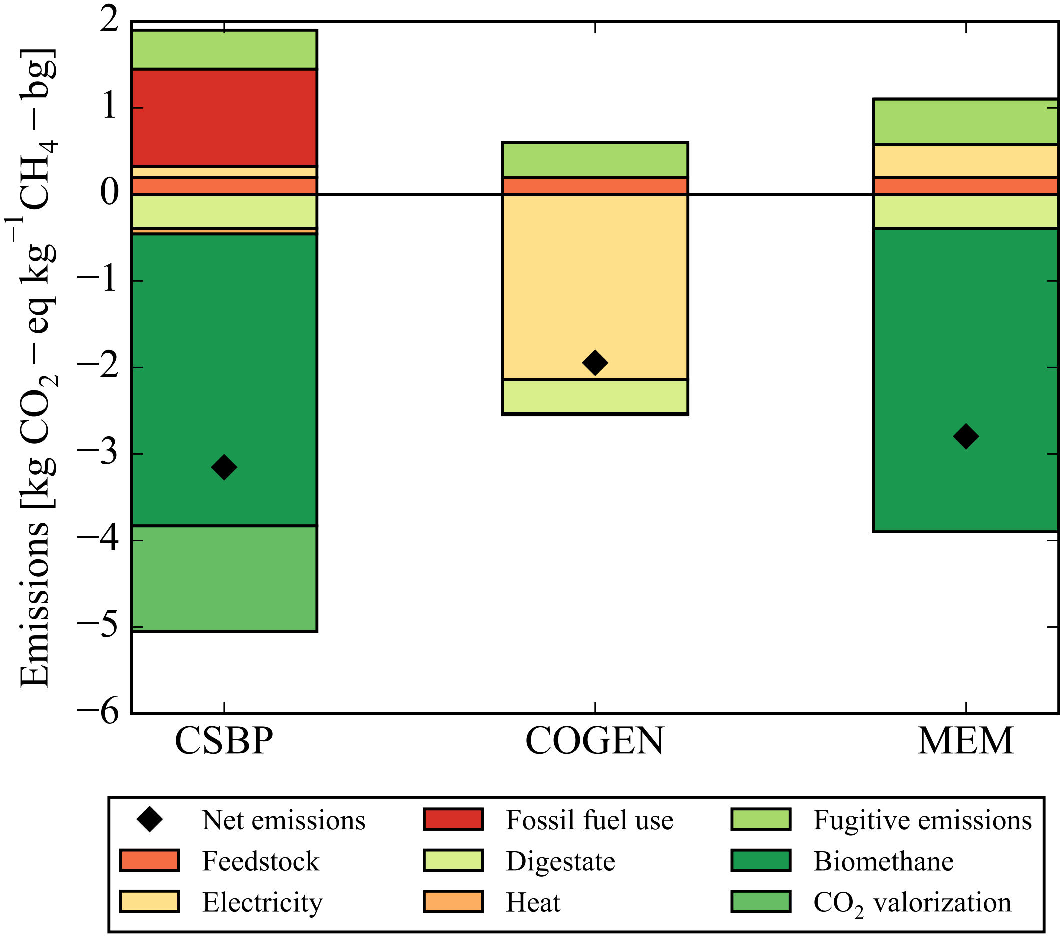

Figure 3.8: Emissions for each study case.

along with the membrane upgrading could achieve lower net emissions compared to CSBP or other classical biogas technologies.

3.4.1 Power-to-gas scenario

An improvement that could be done in MEM scenario is the addition of a catalytic methanation reactor (MET). In this unit, the off-gas of the membrane unit, which is rich in CO_2, would be sent to a methanation reactor, where it would be converted into CH_4 (Eq. 3.5 and Figure 3.9).

$$4H_2 + CO_2 \rightarrow CH_4 + 2H_2O \tag{3.5}$$

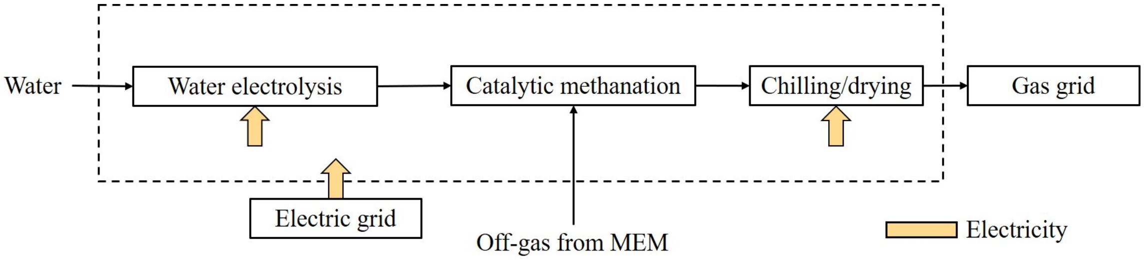

Figure 3.9: Process scheme of MET. The dotted lines delimits the system boundary and, in each box, arrows entering corresponds to inputs and exiting to outputs.

Based on the work of Goffart De Roeck *et al.* [53], a simplified inventory of such unit was estimated (Table 3.9). It was supposed that the methanation reaction would be carried out completely and that H_2 would be supplied at stoichiometric proportions. Electricity consumption and water used in the electrolyzer were estimated at 5 kWh Nm^{-3} H_2 and 0.22 kg H_2O kWh^{-1} respectively [53]. In the chilling step, electricity use was estimated considering 0.12 kWh kg^{-1} H_2O and, in the drying step, 0.04 kWh Nm^{-3} dry gas [53].

Regarding the emissions, this unit yielded a positive value of net emissions. Therefore, adding a methanation reactor to the MEM case would not be environmentally beneficial with current energy mix in Italy. Indeed, electricity corresponded to almost all emissions of this additional unit. However, the emission factor of electricity varies greatly from country to country. In addition, the power CF in Europe has been reducing in recent years due to an increase of renewable energies [74]. When analyzing each scenario's net emissions for different values of electricity EF, adding a methanation unit to MEM case becomes environmentally interesting for values below 0.14 kg CO_2-eq (Fig. 3.10). For countries which electricity has a lower EF or if the electrolyzer is powered by renewable sources, this power-to-gas technology could achieve a better environmental performance compared to a biomethane plant without CO_2 valorization.

3.5 Conclusions

Cooperativa Speranza's biogas plant achieved the highest energy efficiency and the lowest net emissions compared to classical biogas utilization routes. The absorption chiller installed in it allowed the valorization of thermal energy even during the summer months, when there was only demand for

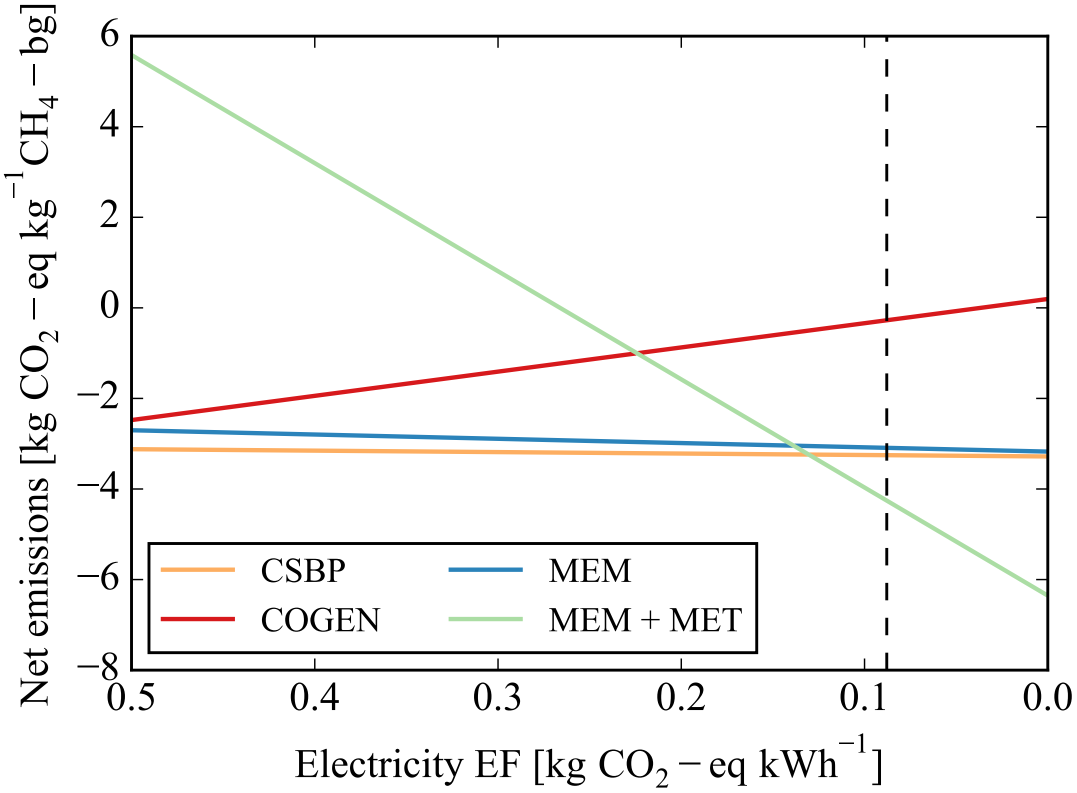

Figure 3.10: Net emissions as a function of emission factor of electricity for different scenarios. The dotted vertical line indicates the EF of French energy mix.

chilled water in the neighbor industry. Indeed, ARS could be an interesting solution to increase the heat usage in biogas plants. Moreover, regarding GWP, generating biomethane should be privileged over cogeneration using biogas in a scenario with decreasing emissions from electricity production. In this context, adding a catalytic methanation to the membrane upgrading plant could achieve lower GWP compared to CSBP depending on the source of the electricity used.

Table 3.7: Inventory data for each scenario.

Input	CSBP	COGEN	MEM
Electricity [kWh]	640 045		1 877 982
Digester feedstock			
Sorghum [kg]	9 372 160	9 372 160	9 372 160
Triticale [kg]	2 357 950	2 357 950	2 357 950
Biogas cleaning			
Activated carbon[1] [kg]	9 955		9 955
NG CHP			
Natural gas [kg]	575 448		
Output			
Electricity [kWh]		10 656 202	
Sold to glass industry			
Heat [kWh]	124 280	124 280	
Cold [kWh]	253 651		
Digester			
Biogenic CH_4 emissions[2] [kg]	19 928	19 928	19 928
Digestate [kg]	46 154 304	46 154 304	46 154 304
N content [kg]	142 155	142 155	142 155
P_2O_5 content [kg]	114 693	114 693	114 693
K_2O content [kg]	48 693	48 693	48 693
Cryogenic upgrading			
Biogenic CH_4 emissions[3] [kg]	9 269		
Bio-LNG [kg]	1 853 704		
LCO2 [kg]	3 318 800		
Membrane unit			
Biogenic CH_4 emissions[4] [kg]			18 166
Biomethane [kg]			1 798 447
NG CHP			
Fossil CH_4 emissions[5] [kg]	2 877		
Fossil CO_2 emissions [kg]	1 582 483		
BG CHP			
Biogenic CH_4 emissions[5] [kg]	798	9 964	
Biogas boiler			
Biogenic CH_4 emissions[5] [kg]			881

[1] Calculated considering 1.85 g activated carbon Nm^{-3} biogas [59]

[2] Biogas leakage in the plant assumed at 1% [11]

[3] A methane loss of 0.5% was assumed [9, 64]

[4] Methane losses in membrane assumed at 1% [59]

[5] A methane loss in combustion of 0.5% was adopted [65, 66]

Table 3.8: Emissions for each study case.

	Emissions [kg CO_2-eq]		
Input	CSBP	COGEN	MEM
Electricity	256 274		751 944
Digester feedstock			
Sorghum	303 511	303 511	303 511
Triticale	89 667	89 667	89 667
Biogas cleaning			
Activated carbon	8 201		8 201
NG CHP			
Natural gas	655 747		
Output			
Electricity		-4 266 743	
Sold to glass industry			
Heat	-26 223	-26 223	
Cold	-100 852		
Digester			
Biogenic CH_4 emissions	538 069	538 069	538 069
Digestate			
N content	-462 862	-462 862	-462 862
P_2O_5 content	-183 682	-183 682	-183 682
K_2O content	-137 358	-137 358	-137 358
Cryogenic upgrading			
Biogenic CH_4 emissions	250 250		
Bio-LNG	-6 732 764		
LCO2	-2 430 984		
Membrane unit			
Biogenic CH_4 emissions			490 486
Biomethane			-6 995 135
NG CHP			
Fossil CH_4 emissions	85 742		
Fossil CO_2 emissions	1 582 483		
BG CHP			
Biogenic CH_4 emissions	21 539	269 034	
Biogas boiler			
Biogenic CH_4 emissions			23 792
Emissions (+)	3 791 482	1 200 281	2 205 669
Avoided emissions (-)	-10 074 726	-5 076 869	-7 779 038
Net emissions	-6 283 243	-3 876 588	-5 573 369

Table 3.9: Inventory and emissions of MET.

Input	Inventory	Emissions [kg CO2-eq]
Electrolyzer		
Electricity [kWh]	45 176 466	18 088 657
Water [kg]	9 938 823	4 306
Methanation		
CO_2 [kg]	4 434 456	
CH_4 [kg]	18 166	
Chilling/drying		
Electricity [kWh]	526 754	210 912
Output		
Chilling/drying		
Syntethic CH_4	1 630 695	-6 342 658
Emissions (+)		18 303 875
Avoided emissions (-)		-6 342 658
Net emissions		11 961 217

CHAPTER 4

ANAEROBIC DIGESTER MODEL AND VALIDATION

Wet digestion using a CSTR digester is the most used technology in biogas plants across Europe. Here, the modeling of such kind of reactor is described. The kinetics were based on a modified version of ADM1 and the thermal description on an advanced thermal model from the literature.

4.1 AD kinetics

The reactions taking place inside the digester were described using an ADM1-derived model developed by Weinrich and Nelles [75], which was briefly described in Section 2.3. Here, a more detailed explanation is given.

Weinrich and Nelles [75] restructured ADM1 into 4 different versions with varying level of complexity. Here, the most complete one with fixed stoichiometry, noted as ADM1-W, was used. This model contains the four reaction stages of AD: hydrolysis, acidogenesis, acetogenesis and methanogenesis. Each one is further detailed in the following sections.

The modifications that were included to ADM1-W are:

- the cell decay reactions were rebalanced in order to fulfill the atomic conservation;
- sulfate reduction reactions were added to the kinetic model so that the H_2S production could be estimated, which was carried out by adding acetate and hydrogen uptake by sulfate reducing bacteria (SRB) [76];
- an inert carbohydrate compound (CHI) was added to account for inert fraction in lignocellulosic biomass [37, 77].

In total, 30 species and 23 reactions are involved in the kinetics (Tables 4.1 and 4.2).

Table 4.1: Species involved in AD kinetics.

Species	Notation	Molecular formula
Carbohydrates	CH	$C_6H_{10}O_5$
Proteins	PR	$C_5H_{7.625}O_{1.5}N_{1.25}$
Lipids	LI	$C_{51}H_{98}O_6$
Glucose	SU	$C_6H_{12}O_6$
Amino acids	AA	$C_5H_{9.625}O_{2.5}N_{1.25}$
Long-chain fatty acids	LCFA	$C_{16}H_{32}O_2$
Valeric acid	HVa	$C_5H_{10}O_2$
Butyric acid	HBu	$C_4H_8O_2$
Propionic acid	HPr	$C_3H_6O_2$
Acetic acid	HAc	$C_2H_4O_2$
Hydrogen	$\mathrm{H_2}$	H_2
Methance	$\mathrm{CH_4}$	CH_4
Carbon dioxide	$\mathrm{CO_2}$	CO_2
Ammonia	$\mathrm{NH_3}$	NH_3
Water	$\mathrm{H_2O}$	H_2O
Glucose acidogens	$\mathrm{X_{SU}}$	$C_5H_7O_2N$
Amino acids acidogens	$\mathrm{X_{AA}}$	$C_5H_7O_2N$
LCFA acidogens	$\mathrm{X_{LCFA}}$	$C_5H_7O_2N$
Valeric acid acetogens	$\mathrm{X_{HVa}}$	$C_5H_7O_2N$
Butyric acid acetogens	$\mathrm{X_{HBu}}$	$C_5H_7O_2N$
Propionic acid acetogens	$\mathrm{X_{HPr}}$	$C_5H_7O_2N$
Acetoclastic methanogens	$\mathrm{X_{HAc}}$	$C_5H_7O_2N$
Hydrogenotrophic methanogens	$\mathrm{X_{H2}}$	$C_5H_7O_2N$
Anions	AN	AN^{-a}
Cations	CAT	CAT^{+a}
Inert carbohydrates	CHI	$C_6H_{10}O_5$
Sulfate	$\mathrm{H_2SO_4}$	H_2SO_4
Hydrogen sulfide	$\mathrm{H_2S}$	H_2S
Acetoclastic sulfate-reducing bacteria	$\mathrm{X_{ASRB}}$	$C_5H_7O_2N$
Hydrogenotrophic sulfate-reducing bacteria	$\mathrm{X_{HSRB}}$	$C_5H_7O_2N$

[a] These species do not participate in any reactions, they are only used to estimate the pH.

Table 4.2: Reactions involved in AD kinetics.

Reaction	Notation
Carbohydrates hydrolysis	HY-CH
Proteins hydrolysis	HY-PR
Lipids hydrolysis	HY-LI
Glucose acidogenesis	AI-SU
Amino acids acidogenesis	AI-AA
Long-chain fatty acids acidogenesis	AI-LCFA
Valeric acid acetogenesis	AE-HVa
Butyric acid acetogenesis	AE-HBu
Propionic acid acetogenesis	AE-HPr

Continued on next page

Table 4.2 – *Continued from previous page*

Reaction	Notation
Acetoclastic methanogenesis	ME-HAc
Hydrogenotrophic methanogenesis	ME-H_2
Acetoclastic sulfate reduction	ASRB
Hydrogenetropic sulfate reduction	HSRB
Glucose acidogens decay	DE-SU
Amino acids acidogens decay	DE-AA
LCFA acidogens decay	DE-LCFA
Valeric acid acetogens decay	DE-HVa
Butyric acid acetogens decay	DE-HBu
Propionic acid acetogens decay	DE-HPr
Acetoclastic methanogens decay	DE-HAc
Hydrogenotrophic methanogens decay	DE-H_2
Acetoclastic sulfate-reducing bacteria decay	DE-ASRB
Hydrogenotrophic sulfate-reducing bacteria decay	DE-HSRB

4.1.1 Hydrolysis

In this stage, three reactions take place: carbohydrates hydrolysis (Eq. 4.1), proteins hydrolysis (Eq. 4.2) and lipids hydrolysis (Eq. 4.3). The rates of these reactions were calculated using a first-order kinetic equation as a function of their respective substrates concentrations (Eqs. 4.4-4.6).

$$C_6H_{10}O_5 + H_2O \rightarrow C_6H_{12}O_6 \tag{4.1}$$

$$C_5H_{7.625}O_{1.5}N_{1.25} + H_2O \rightarrow C_5H_{9.625}O_{2.5}N_{1.25} \tag{4.2}$$

$$C_{51}H_{98}O_6 + 0.538\ CO_2 + 2.538\ H_2O \rightarrow 0.604\ C_6H_{12}O_6 + 2.995\ C_{16}H_{32}O_2 \tag{4.3}$$

$$r_{HY-CH} = k_{HY-CH}C_{CH} \tag{4.4}$$

$$r_{HY-PR} = k_{HY-PR}C_{PR} \tag{4.5}$$

$$r_{HY-LI} = k_{HY-LI} C_{LI} \tag{4.6}$$

4.1.2 Acidogenesis

The monomers originated from the macromolecules cleavage in the hydrolysis step are broken down to volatile fatty acids in the acidogenesis step. This stage comprehends: glucose acidogenesis (Eq. 4.7), amino acids acidogenesis (Eq. 4.8), LCFA acidogenesis (Eq. 4.9). These reactions take place inside the cells and they were calculated using a Monod-type equation as a function of the inhibited growth rate, μ (Eqs. 4.10-4.12). In these equations, I corresponds to the inhibition factor, which varies between 0 and 1 and represents the reaction impairment effect due to non-ideal reaction conditions; and K_S is the half-saturation constant.

$$\begin{aligned} 8.33\, C_6H_{12}O_6 + NH_3 + 2.64\, H_2O \rightarrow & 1.17\, C_4H_8O_2 + 3.48\, C_3H_6O_2 + 9.23\, C_2H_4O_2 \\ & + 17.10\, H_2 + 11.46\, CO_2 + C_5H_7O_2N \end{aligned} \tag{4.7}$$

$$\begin{aligned} 11.90\, C_5H_{9.625}O_{2.5}N_{1.25} + 21.20\, H_2O \rightarrow & 2.02\, C_5H_{10}O_2 + 2.98\, C_4H_8O_2 \\ & + 0.82\, C_3H_6O_2 + 11.43\, C_2H_4O_2 + 6.87\, H_2 \\ & + 7.24\, CO_2 + C_5H_7O_2N \end{aligned} \tag{4.8}$$

$$3.62\, C_{16}H_{32}O_2 + 1.86\, CO_2 + NH_3 + 45.54\, H_2O \rightarrow 27.42\, C_2H_4O_2 + 47\, H_2 + C_5H_7O_2N \tag{4.9}$$

$$r_{AI-SU} = \mu_{SU} \frac{C_{SU}}{K_{S,\,SU} + C_{SU}} C_{XSU} I_{AI-SU} \tag{4.10}$$

$$r_{AI-AA} = \mu_{AA} \frac{C_{AA}}{K_{S,\ AA} + C_{AA}} C_{XAA} I_{AI-AA} \tag{4.11}$$

$$r_{AI-LCFA} = \mu_{LCFA} \frac{C_{LCFA}}{K_{S,\ LCFA} + C_{LCFA}} C_{XLCFA} I_{AI-LCFA} \tag{4.12}$$

In the inhibition factors evaluation, NH_3 was considered a co-substrate and it was included the effect of pH as well (Eqs. 4.13-4.15). For LCFA acidogenesis, hydrogen inhibition effect was included (Eq. 4.15).

$$I_{AI-SU} = \frac{K_{ph,\ aa}^{n_{aa}}}{K_{ph,\ aa}^{n_{aa}} + {C_{H^+}^{L}}^{n_{aa}}} \frac{C_{NH_3}^{L}}{C_{NH_3}^{L} + K_{S,\ IN}} \tag{4.13}$$

$$I_{AI-AA} = \frac{K_{ph,\ aa}^{n_{aa}}}{K_{ph,\ aa}^{n_{aa}} + {C_{H^+}^{L}}^{n_{aa}}} \frac{C_{NH_3}^{L}}{C_{NH_3}^{L} + K_{S,\ IN}} \tag{4.14}$$

$$I_{AI-LCFA} = \frac{K_{ph,\ aa}^{n_{aa}}}{K_{ph,\ aa}^{n_{aa}} + {C_{H^+}^{L}}^{n_{aa}}} \frac{C_{NH_3}^{L}}{C_{NH_3}^{L} + K_{S,\ IN}} \frac{K_{I,\ LCFA}}{K_{I,\ LCFA} + C_{H_2}^{L}} \tag{4.15}$$

$K_{ph,aa}$ and n_{aa} that appear in the pH inhibition effect were calculated using Eqs. 4.16 and 4.17.

$$n_{aa} = \frac{3}{pH_{UL,aa} - pH_{LL,aa}} \tag{4.16}$$

$$K_{ph,aa} = 10^{-\frac{pH_{UL,aa} + pH_{LL,aa}}{2}} \tag{4.17}$$

4.1.3 Acetogenesis

The VFAs produced in acidogenesis are then converted to acetic acid in the acetogenesis reactions, which includes: valeric acid acetogenesis (Eq. 4.18), butyric acid acetogenesis (Eq. 4.19), and propionic acid acetogenesis (Eq. 4.20). Their reaction rates were calculated using Eqs. 4.21-4.23. Inhibition effects included NH_3 as co-substrate, pH effect and H_2 inhibition (Eqs. 4.24-4.26).

$$\begin{aligned}12.82\,C_5H_{10}O_2 + 1.44\,CO_2 + NH_3 + 21.94\,H_2O \rightarrow & 12.09\,C_3H_6O_2 + 12.14\,C_2H_4O_2 \\ & + 23.5\,H_2 + C_5H_7O_2N\end{aligned} \tag{4.18}$$

$$16.67\,C_4H_8O_2 + CO_2 + NH_3 + 29.33\,H_2O \rightarrow 31.33\,C_2H_4O_2 + 31.33\,H_2 + C_5H_7O_2N \tag{4.19}$$

$$\begin{aligned}35.71\,C_3H_6O_2 + NH_3 + 66.46\,H_2O \rightarrow & 34.21\,C_2H_4O_2 + 103.21\,H_2 + 33.75\,CO_2 \\ & + C_5H_7O_2N\end{aligned} \tag{4.20}$$

$$r_{AE-HVa} = \mu_{HVa} \frac{C_{HVa}}{K_{S,\,HVa} + C_{HVa}} \frac{C_{HVa}}{C_{HVa} + C_{HBu}} C_{XHVa} I_{AE-HVa} \tag{4.21}$$

$$r_{AE-HBu} = \mu_{HBu} \frac{C_{HBu}}{K_{S,\,HBu} + C_{HBu}} \frac{C_{HBu}}{C_{HBu} + C_{HVa}} C_{XHBu} I_{AE-HBu} \tag{4.22}$$

$$r_{AE-HPr} = \mu_{HPr} \frac{C_{HPr}}{K_{S,\,HPr} + C_{HPr}} C_{XHPr} I_{AE-HPr} \tag{4.23}$$

$$I_{AE-HVa} = \frac{K_{ph,\,aa}^{n_{aa}}}{K_{ph,\,aa}^{n_{aa}} + {C_{H^+}^{L}}^{n_{aa}}} \frac{C_{NH_3}^{L}}{C_{NH_3}^{L} + K_{S,\,IN}} \frac{K_{I,\,C4C5}}{K_{I,\,C4C5} + C_{H_2}^{L}} \tag{4.24}$$

$$I_{AE-HBu} = \frac{K_{ph,\,aa}^{n_{aa}}}{K_{ph,\,aa}^{n_{aa}} + {C_{H^+}^{L}}^{n_{aa}}} \frac{C_{NH_3}^{L}}{C_{NH_3}^{L} + K_{S,\,IN}} \frac{K_{I,\,C4C5}}{K_{I,\,C4C5} + C_{H_2}^{L}} \tag{4.25}$$

$$I_{AE-HPr} = \frac{K_{ph,\,aa}^{n_{aa}}}{K_{ph,\,aa}^{n_{aa}} + {C_{H^+}^{L}}^{n_{aa}}} \frac{C_{NH_3}^{L}}{C_{NH_3}^{L} + K_{S,\,IN}} \frac{K_{I,\,HPr}}{K_{I,\,HPr} + C_{H_2}^{L}} \tag{4.26}$$

4.1.4 Methanogenesis

Two methane producing reactions were included: acetoclastic methanogenesis (Eq. 4.27) and hydrogenotrophic methanogenesis (Eq. 4.28). Their reaction rates were estimated with Eqs. 4.29 and 4.30. F_K corresponds to a short-term effect of temperature variations [78], which is further described in Section 4.1.7.

$$50\,C_2H_4O_2 + NH_3 \rightarrow 47.5\,CH_4 + 47.5\,CO_2 + 3\,H_2O + C_5H_7O_2N \tag{4.27}$$

$$16.67\,H_2 + 44.17\,CO_2 + NH_3 \rightarrow 39.17\,CH_4 + 86.33\,H_2O + C_5H_7O_2N \tag{4.28}$$

$$r_{ME-HAc} = \mu_{HAc}\frac{C_{HAc}}{K_{S,\,HAc} + C_{HAc}}C_{XHAc}I_{ME-HAc}F_K\left(T^L,\,T_a\right) \tag{4.29}$$

$$r_{ME-H2} = \mu_{H_2}\frac{C_{H_2}}{K_{S,\,H_2} + C_{H_2}}C_{XH_2}I_{ME-H_2}F_K\left(T^L,\,T_a\right) \tag{4.30}$$

The inhibition factors were calculated using Eqs. 4.31 and 4.32, in which it was also included the effect of hydrogen sulfide in the solution. I_{H_2S} was estimated according to the approach suggested by Pokorna-Krayzelova *et al.* [79] (Eq. 4.33). The evaluation of the non-ionized H_2S concentration, C_{free,H_2S} is explained in Section 4.1.8.

$$I_{ME-HAc} = \frac{K_{ph,\,ac}^{n_{ac}}}{K_{ph,\,ac}^{n_{ac}} + {C_{H+}^{L}}^{n_{ac}}}\frac{C_{NH_3}^{L}}{C_{NH_3}^{L} + K_{S,\,IN}}\frac{K_{I,\,NH_3}}{K_{I,\,NH_3} + C_{free\ NH_3}^{L}}I_{H_2S} \tag{4.31}$$

$$I_{ME-H2} = \frac{K_{ph,\,h2}^{n_{h2}}}{K_{ph,\,h2}^{n_{h2}} + {C_{H+}^{L}}^{n_{h2}}}\frac{C_{NH_3}^{L}}{C_{NH_3}^{L} + K_{S,\,IN}}I_{H_2S} \tag{4.32}$$

$$I_{H_2S} = \begin{cases} \left(1 - \frac{C^L_{free\ H_2S}}{K_{I,\ H_2S}}\right)^{n_{I,\ H_2S}}, \ C^L_{free\ H_2S} < K_{I,\ H_2S} \\ 10^{-6},\ C^L_{free\ H_2S} \geq K_{I,\ H_2S} \end{cases} \tag{4.33}$$

$K_{ph,\ h2}$ and n_{h2} were evaluated with Eqs. 4.34 and 4.35 respectively.

$$K_{ph,h2} = 10^{-\frac{pH_{UL,h2}+pH_{LL,h2}}{2}} \tag{4.34}$$

$$n_{h2} = \frac{3}{pH_{UL,h2} - pH_{LL,h2}} \tag{4.35}$$

4.1.5 Sulfate reduction

In anaerobic digestion, sulfate is biochemically reduced to hydrogen sulfide. As this contaminant was not accounted for in ADM1-W despite being relevant in agricultural biogas plants [80], the sulfate reduction reactions were added (Eqs. 4.36 and 4.37). Similarly to the work of Fedorovich *et al.* [81], H_2SO_4 was used to represent the sulfate in the digestate, even though it would be actually present in its ionized forms as HSO_4^- and SO_4^{2-}. The reactions rates were calculated with Eqs. 4.38 and 4.39, and the inhibition factors with Eqs. 4.40 and 4.41. I_{H_2S} was estimated with Eq. 4.33.

$$\begin{aligned} 71.43\,C_2H_4O_2 + NH_3 + 69.21 H_2SO_4 \rightarrow & 138\,CO_2 + 141.86\,H_2O + 69.21 H_2S \\ & + C_5H_7O_2N \end{aligned} \tag{4.36}$$

$$0.125\,H_2 + 5\,CO_2 + NH_3 + 28.75 H_2SO_4 \rightarrow 123\,H_2O + 28.75 H_2S + C_5H_7O_2N \tag{4.37}$$

$$r_{ASRB} = \mu_{ASRB} \frac{C_{HAc}}{K_{S,\ ASRB} + C_{HAc}} \frac{C_{H_2SO_4}}{K_{S,\ H_2SO_4,\ ASRB} + C_{H_2SO_4}} C_{XASRB} I_{ASRB} \tag{4.38}$$

$$r_{HSRB} = \mu_{HSRB} \frac{C_{H_2}}{K_{S,\ HSRB} + C_{H_2}} \frac{C_{H_2SO_4}}{K_{S,\ H_2SO_4,\ HSRB} + C_{H_2SO_4}} C_{XHSRB} I_{HSRB} \tag{4.39}$$

$$I_{ASRB} = \frac{K_{ph,\ ac}^{n_{ac}}}{K_{ph,\ ac}^{n_{ac}} + {C_{H^+}^{L}}^{n_{ac}}} \frac{C_{NH_3}^{L}}{C_{NH_3}^{L} + K_{S,\ IN}} I_{H_2S} \tag{4.40}$$

$$I_{HSRB} = \frac{K_{ph,\ h2}^{n_{h2}}}{K_{ph,\ h2}^{n_{h2}} + {C_{H^+}^{L}}^{n_{h2}}} \frac{C_{NH_3}^{L}}{C_{NH_3}^{L} + K_{S,\ IN}} I_{H_2S} \tag{4.41}$$

4.1.6 Cell decay

Several reactions of AD are accompanied by microorganism cell growth. The death and degradation of these bacterial biomass are represented by the cell decay reactions (Eq. 4.42), which were adopted for each microorganism species (e.g. X_{SU}, X_{AA}, etc.). Compared to the reaction used by Weinrich and Nelles [75], H_2O and CO_2 were added to the reactions to fulfill the atomic conservation. The rates of these reactions were calculated with a first order kinetic equation (Eqs. 4.43-4.51). The same kinetic constant value was used in all cell decay reactions.

$$\begin{aligned} C_5H_7O_2N + 0.158\ H_2O \rightarrow & 0.326\ CO_2 + 0.007\ C_{51}H_{98}O_6 + 0.800\ C_5H_{7.625}O_{1.5}N_{1.25} \\ & + 0.053\ C_6H_{10}O_5 \end{aligned} \tag{4.42}$$

$$r_{DE-SU} = k_{DE} C_{X_{SU}} \tag{4.43}$$

$$r_{DE-AA} = k_{DE} C_{X_{AA}} \tag{4.44}$$

$$r_{DE-LCFA} = k_{DE} C_{X_{LCFA}} \tag{4.45}$$

$$r_{DE-HBu} = k_{DE} C_{X_{HBu}} \tag{4.46}$$

$$r_{DE-HPr} = k_{DE} C_{X_{HPr}} \tag{4.47}$$

$$r_{DE-HAc} = k_{DE} C_{X_{HAc}} \tag{4.48}$$

$$r_{DE-H2} = k_{DE} C_{X_{H2}} \tag{4.49}$$

$$r_{DE-ASRB} = k_{DE} C_{X_{ASRB}} \tag{4.50}$$

$$r_{DE-HSRB} = k_{DE} C_{X_{HSRB}} \tag{4.51}$$

4.1.7 Temperature effect on kinetics

In ADM1-W, two sets of kinetic parameters are provided: one for mesophilic (310.15 K) and another one for thermophilic digestion (328.15 K). For each temperature regime, these values are considered constant. However, the reaction rates actually are variable with temperature fluctuations [82], but such variations are not easily quantifiable [83].

The Arrhenius Law was used to evaluate the kinetic constant at different temperatures for the hydrolysis reactions (Eq. 4.52). The value of 64 kJ mol^{-1} was adopted for the activation energy of all hydrolysis reactions, which corresponds to an average value obtained for different biowastes [84] and the frequency factors were calculated so that the kinetic constants corresponded to the ones provided in ADM1-W.

Table 4.3: Calculated kinetic parameters

Parameter	Unit	Value
$A_{0,\ HY-CH}$	s^{-1}	$1.74\ 10^5$
$A_{0,\ HY-PR}$	s^{-1}	$1.39\ 10^5$
$A_{0,\ HY-LI}$	s^{-1}	$6.96\ 10^4$
α_{AI-SU}	$d^{-1}\ K^{-1}$	0.2
α_{AI-AA}	$d^{-1}\ K^{-1}$	0.08
$\alpha_{AI-LCFA}$	$d^{-1}\ K^{-1}$	0.012
α_{AE-HVa}	$d^{-1}\ K^{-1}$	0.03
α_{AE-HBu}	$d^{-1}\ K^{-1}$	0.03
α_{AE-HPr}	$d^{-1}\ K^{-1}$	0.014
α_{ME-HAc}	$d^{-1}\ K^{-1}$	0.02
α_{ME-H_2}	$d^{-1}\ K^{-1}$	0.02

$$k_j = A_{0,\ j} exp\left(-\frac{E_{a_j}}{RT^L}\right) \tag{4.52}$$

Regarding the other bioreactions, the same methodology used in BioModel was employed [40, 41]. Thus, the maximum growth rates were considered to increase linearly with temperature until a maximum value, at T^L_{opt}, from which they decrease also linearly until T^L_{max}, when the growth rates reach zero (Eq. 4.53). The value of $\alpha_{R,j}$ was estimated in such way that the growth rates coincided with the suggested values for mesophilic and for thermophilic temperatures. The optimal temperature was adopted at 328.15 K and the maximal at 338.15 K [40]. The cell decay reactions were assumed to not vary with temperature. The calculated kinetic parameters are summarized in Table 4.3.

$$\begin{cases} \mu_j = \mu_{310.15\ K,\ j} + \alpha_{R,\ j}\left(T^L - 310.15\right),\ T^L < T^L_{opt} \\ \mu_j = \mu_{opt,\ j}\frac{T^L_{max} - T^L}{T^L_{max} - T^L_{opt}},\ T^L_{max} > T^L \\ \mu_j = 0,\ T \geq T^L_{max} \end{cases} \tag{4.53}$$

Besides that, it has been evidenced that quick variations of temperature can significantly impair the bioreactions inside the digester [82, 85]. Therefore, an inhibition factor that accounts the effect of short-term variations of the temperature was included in the estimation of the reaction rates of the two methanogenesis reactions (Eq. 4.54) [85], which have been pointed out as the reactions involving the microorganism groups the most sensitive to temperature changes [85]. This factor, F_K, represents the inhibition that occurs when the reaction temperature is different from the one at which the microorganisms are adapted. The long-term adaption to new reaction conditions is represented by T_a, the temperature to which the microorganisms are adapted, which was evaluated as a dynamic variable that continuously shifts towards the digestate temperature T^L (Eq. 4.55). The parameters τ_a and s_{hg} were taken as, respectively, 30 d and 5 K [85].

$$F_K\left(T^L,\, T_a\right) = exp\left(-\frac{\left(T^L - T_a\right)^2}{2\sigma_K^2}\right),\ \sigma_K = \left(-\frac{s_{hg}^2}{2ln(0.5)}\right)^{0.2} \tag{4.54}$$

$$\frac{dT_a}{dt} = \frac{T^L - T_a}{\tau_a} \tag{4.55}$$

4.1.8 pH estimation

The pH is another factor that influences the bioreactions inside the digester [33, 86]. This property was calculated through a charge balance in digestate (Eqs. 4.56-4.58). In these equations, the molar concentrations were converted to mol L^{-1}.

$$pH = log_{10}\left(C_{H^+}\right) \tag{4.56}$$

$$\begin{aligned} \Phi_{pH} &= C_{OH^-} - C_{H^+} = \\ &= C_{CAT} + C_{NH_4^+} - C_{AN} - C_{HCO_3^-} - 2C_{CO_3^{2-}} - C_{Ac} - C_{Pr} - C_{Bu} + \\ &\quad - C_{Va} - C_{HS^-} - C_{HSO_4^-} - 2C_{SO_4^{2-}} \end{aligned} \tag{4.57}$$

$$C_{H^+} = -\frac{\Phi_{pH}}{2} + \frac{1}{2}\cdot\sqrt{\Phi_{pH}^2 + 4\cdot K_W} \tag{4.58}$$

In acid-base reactions, the total concentration of each compound was obtained from the mass balances and the amount in each ionic form was estimated considering the chemical equilibrium.

Using HAc as an example, the concentration of ions acetate, Ac^{-1}, was calculated as a function of C_{HAc} and C_{H^+} (Eq. 4.59), and the acid in its free form was estimated as the difference between the acid in its free form and its dissociated form (Eq. 4.60). This approach was equally used for other acids and, analogously, for ammonia.

$$C_{Ac^-} = \frac{C^L_{HAc} \cdot Ka_{HAc}}{C_{H^+} + Ka_{HAc}} \tag{4.59}$$

$$C^{free}_{HAC} = C^L_{HAC} - C_{AC^-} \tag{4.60}$$

However, the acid-base reactions of CO$_2$ in water involves two reactions. Thus, Eqs. 4.61 and 4.62 were used to quantify $C_{HCO_3^-}$ and $C_{CO_3^{2-}}$.

$$C_{HCO_3^+} = \frac{Ka_{1,\,CO_2} \cdot C^L_{CO_2}}{C_{H^+} + Ka_{2,\,CO_2} - \frac{C_{H^+} \cdot Ka_{2,\,CO_2}}{C_{H^+} + Ka_{2,\,CO_2}}} \cdot \left(1 - \frac{Ka_{2,\,CO_2}}{C_{H^+} + Ka_{2,\,CO_2}}\right) \tag{4.61}$$

$$C_{CO_3^{2-}} = \frac{Ka_{2,\,CO_2}}{C_{H^+} + Ka_{2,\,CO_2}} \cdot \frac{Ka_{1,\,CO_2} \cdot C^L_{CO_2}}{C_{H^+} + Ka_{2,\,CO_2} - \frac{C_{H^+} \cdot Ka_{2,\,CO_2}}{C_{H^+} + Ka_{2,\,CO_2}}} \tag{4.62}$$

4.2 Digester model

The digester was modeled considering a wet digestion technology with a double-membrane gasholder (Figure 4.1). Thus, a 0-D model approach was used to represent each part of the digester: liquid phase (L), gas phase (G) and the air layer inside the zone between the two covers (A). In all these parts, a perfect mixing was assumed. In the gas phases (i.e. G and A), it was adopted an ideal gas behavior.

4.2.1 Material balances

In the liquid and the gas phases, partial mass balances were applied for each component i (Eqs. 4.63 and 4.64). The same was done for air in A (Eq. 4.65).

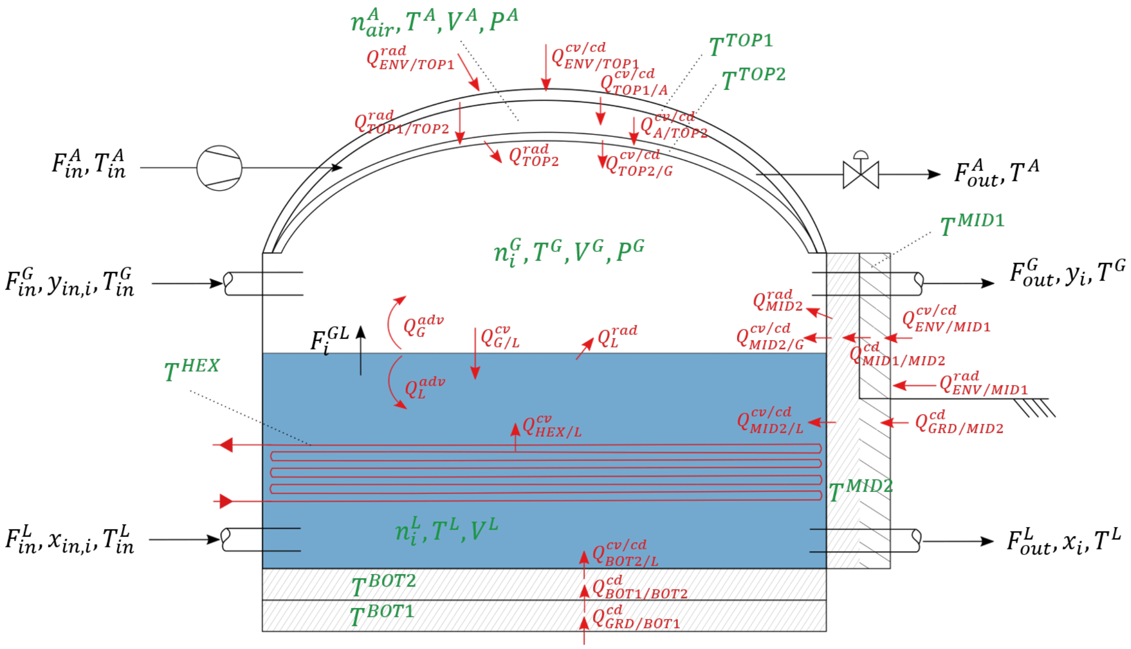

Figure 4.1: Model scheme of a digester with a double-membrane gasholder. Material streams are represented by black arrows, the energy flows are in red, and the main variables in green.

$$\frac{dn_i^L}{dt} = F_{in}^L x_{in,i} - F_{out}^L x_i + \sum_j \nu_{i,\,j} r_j V^L - F_i^{GL} \tag{4.63}$$

$$\frac{dn_i^G}{dt} = F_{in}^G y_{in,i} - F_{out}^G y_{out,i} + F_i^{GL} \tag{4.64}$$

$$\frac{dn_{air}^A}{dt} = F_{in}^A - F_{out}^A \tag{4.65}$$

The molar fractions in L and in G were calculated from the molar quantities in each phase (Eqs. 4.66 and 4.67). The inlet flow rates F_{in}^L and F_{in}^G were either model parameters or calculated from the outlet of another unit. For example, with two digesters in series, the inlet of the second one corresponds to the outlet of the first. The evaluation of outlet flow rates is explained in Section 4.5. In the air layer, the inlet was calculated considering a blower and the outlet a valve, and they are further developed in Section 4.4.

In the chemical reaction term, the stoichiometric coefficients and the reaction rates were evaluated according to Section 4.1. The mass transfer between the gas and liquid phases was accounted for in F_i^{GL}, which calculation is explained in Section 4.2.2. The molar concentrations were estimated from the molar quantities and the phase volumes (Eqs. 4.68 and 4.69).

$$x_i = \frac{n_i^L}{\sum_\iota n_\iota^L} \tag{4.66}$$

$$y_i = \frac{n_i^G}{\sum_\iota n_\iota^G} \tag{4.67}$$

$$C_i^L = \frac{n_i^L}{V^L} \tag{4.68}$$

$$C_i^G = \frac{n_i^L}{V^G} \tag{4.69}$$

In total, it was considered 30 species in the liquid phase (the same as in Table 4.1) and 6 in the gas phase (H_2, CH_4, CO_2, NH_3, H_2O, H_2S).

4.2.2 Mass transfer

The mass transfer flow rate between the liquid and the gas phase, F_i^{GL}, was evaluated considering that the diffusion in the liquid phase was the limiting step, the equilibrium concentration in the liquid phase being described by Henry's Law for each component i solutilized in water (Eq. 4.70). In the literature, the mass transfer coefficients, k_La_i, were either considered as constant values [33, 39] or calibrated with other model parameters [87, 88]. In large scale anaerobic digesters, there are different stirrer configurations, which can vary, for instance, on the number of stirrers, the rotation speed, type and size of the devices [89]. For this reason, the use of empirical correlations that relates the stirrer dimension to the mass transfer coefficient values [90] would be difficult. Thus, in this study, a mass transfer coefficient of 55 d^{-1} was taken for the CO_2 [91] and the values for the other solutes were corrected according to their diffusivities in the gas phase [92].

$$F_i^{GL} = k_La_iV^L\left(C_i^L - K_{H,\,i}P_i\right),\ i \neq H_2O \tag{4.70}$$

For the mass transfer of water the analogy between heat and mass transfer was employed considering natural convection over the liquid to estimate the mass transfer coefficient k_G [93]. It was used a correlation for natural convection over an horizontal plat (Appendix B.1.1), replacing Nu by Sh, Gr by Gr_m, and Pr by Sc [93]. Moreover, as water is the solvent, the limiting step was adopted to be in the gas phase (Eq. 4.71). The mass transfer surface was adopted as the circle formed by the digester's internal diameter ID (Eq. 4.72).

$$F_{H_2O}^{GL} = k_G A_{GL} \left(C_{sat,\ H_2O}^{G} - C_{H_2O}^{G} \right) \tag{4.71}$$

$$A_{GL} = \frac{\pi ID^2}{4} \tag{4.72}$$

4.2.3 Energy balances

The temperatures of each part (L, G and A) were evaluated through energy balances on each phase (Eqs. 4.73-4.75). Additionally, energy balances were applied to the digester's structure to represent their thermal inertia. The structure was composed by: two wall layers ($MID1$ and $MID2$), two floor layers ($BOT1$ and $BOT2$), two covers in the double membrane gasholder ($TOP1$ and $TOP2$), and the heat exchanger's tube (HEX), as depicted in Figure 4.1. $MID2$ correspond to the inner layer of the above-ground walls and the integrality of the underground part. The energy conservation equation to each of the digester's elements are shown in Eqs. 4.76-4.82.

The heat flow rates appearing in the energy balance equations, Q, correspond to the different heat transfers of each body with the surrounding materials or phases. The calculations of these terms are explained in Section 4.3. Liquid and gas mixtures were considered ideal and it was assumed that all gases were ideal as well. The enthalpy reference of each component i was set to 0 for the standard state and the enthalpies were then evaluated as enthalpy variations (depending on the temperature) from this standard state. In case of gases dissolved in liquid phase (CH_4, CO_2, NH_3, H_2, H_2S), the hydration enthalpy was supposed constant at the temperature range used in the model. The physical-chemical properties used to calculate the enthalpies and other parameters used in the model were obtained from various sources [93, 94, 95, 96, 97, 98].

The gas and liquid inlet temperatures are either model parameters or obtained from the result of another unit (e.g. digesters in series). The air inlet temperature was adopted equal as the external air temperature, which was obtained from meteorological data.

$$\begin{aligned}\sum_i n_i^L Cp_i^L \frac{dT^L}{dt} =& \sum_i F_{in}^L x_{in,i} \left(\tilde{H}_i^L \left(T_{in}^L \right) - \tilde{H}_i^L \left(T^L \right) \right) - \sum_j \Delta \tilde{H}_{R,\,j} r_j V^L + \dot{W}_s \\ &+ Q_L^{adv} + Q_{MID2/L}^{cv/cd} + Q_{BOT2/L}^{cv/cd} + Q_{G/L}^{cv} - Q_L^{rad} + Q_{HEX/L}^{cv}\end{aligned} \tag{4.73}$$

$$\begin{aligned}\sum_i n_i^G Cv_i^G \frac{dT^G}{dt} =& \sum_i F_{in}^G y_{in,i} \left(\tilde{H}_i^G \left(T_{in}^G \right) - \tilde{H}_i^G \left(T^G \right) \right) \\ &+ RT^G \sum_i \left(F_i^{GL} + F_{in}^G y_{in,i} - F_{out}^G y_i \right) + Q_G^{adv} \\ &+ Q_{MID2/G}^{cv/cd} + Q_{TOP2/G}^{cv/cd} - Q_{G/L}^{cv}\end{aligned} \tag{4.74}$$

$$n^A Cv^A \frac{dT^A}{dt} = F_{in}^A Cp^A \left(T_{in}^A - T^A \right) + RT^A \left(F_{in}^A - F_{out}^A \right) + Q_{TOP1/A}^{cv/cd} - Q_{A/TOP2}^{cv/cd} \tag{4.75}$$

$$\begin{aligned}m^{TOP1} Cp^{TOP1} \frac{dT^{TOP1}}{dt} =& Q_{ENV/TOP1}^{rad} + Q_{ENV/TOP1}^{cv/cd} - Q_{TOP1/TOP2}^{rad} \\ &- Q_{TOP1/A}^{cv/cd}\end{aligned} \tag{4.76}$$

$$m^{TOP2} Cp^{TOP2} \frac{dT^{TOP2}}{dt} = Q_{TOP1/TOP2}^{rad} + Q_{A/TOP2}^{cv/cd} - Q_{TOP2/G}^{cv/cd} - Q_{TOP2}^{rad} \tag{4.77}$$

$$m^{MID1}Cp^{MID1}\frac{dT^{MID1}}{dt} = Q^{cv/cd}_{ENV/MID1} - Q^{cd}_{MID1/MID2} \tag{4.78}$$

$$\begin{aligned} m^{MID2}Cp^{MID2}\frac{dT^{MID2}}{dt} =& Q^{cd}_{GRD/MID2} + Q^{cd}_{MID1/MID2} - Q^{cv/cd}_{MID2/G} \\ & - Q^{cv/cd}_{MID2/L} - Q^{rad}_{MID2} \end{aligned} \tag{4.79}$$

$$m^{BOT1}Cp^{BOT1}\frac{dT^{BOT1}}{dt} = Q^{cd}_{GRD/BOT1} - Q^{cd}_{BOT1/BOT2} \tag{4.80}$$

$$m^{BOT2}Cp^{BOT2}\frac{dT^{BOT2}}{dt} = Q^{cd}_{BOT1/BOT2} - Q^{cv/cd}_{BOT2/L} \tag{4.81}$$

$$m^{HEX}Cp^{HEX}\frac{dT^{HEX}}{dt} = Q^{cv}_{HW/HEX} - Q^{cv}_{HEX/L} \tag{4.82}$$

4.3 Thermal model

The digester's thermal model correspond to a resistance-capacitance approach [99], where the energy balances evaluate the energy accumulation and the thermal flows are calculated using heat transfer resistances. Similarly to the work of Avila-Lopez *et al.* [47], energy conservation equations were applied to many parts of the reactor structure, as seen in Section 4.2.3 (Eqs. 4.76-4.81). Here, the calculations of heat flow rate terms are described.

4.3.1 Conduction and convection

Conduction, convection and their combined effect in the heat transfer effect were computed considering the total resistance to heat transfer. Between the gas and liquid phases, it was assumed only a convective resistance (Eq. 4.83). In the heat transfer between the heat exchanger's tubes, the conduction in the tubes was neglected. The calculation of $Q^{cv}_{HEX/L}$ is detailed in Section 4.3.4.

$$Q^{cv}_{G/L} = \frac{T^G - T^L}{R^{cv}_{th,G/L}} \tag{4.83}$$

Between the wall and the floor layers, the conduction flow rate was calculated from the sum of thermal resistances in each body (Eqs. 4.84 and 4.85). The heat interactions with the ground (i.e. $GRD/BOT1$ and $GRD/MID2$) are described in Section 4.3.5.

$$Q^{cd}_{MID1/MID2} = \frac{T^{MID1} - T^{MID2}}{R^{cd}_{th,MID1} + R^{cd}_{th,MID2}} \tag{4.84}$$

$$Q^{cd}_{BOT1/BOT2} = \frac{T^{BOT1} - T^{BOT2}}{R^{cd}_{th,BOT1} + R^{cd}_{th,BOT2}} \tag{4.85}$$

In case where there was conduction and convection, their respective resistances were summed. This was applied to the following pairs: $BOT2/L$ (Eq. 4.86), $MID2/L$ (Eq. 4.87), $MID2/G$ (Eq. 4.88), $ENV/MID1$ (Eq. 4.89), $TOP2/G$ (Eq. 4.90), $A/TOP2$ (Eq. 4.91), $TOP1/A$ (Eq. 4.92), $ENV/TOP1$ (Eq. 4.93).

$$Q^{cv/cd}_{BOT2/L} = \frac{T^{BOT2} - T^L}{R^{cv}_{th,BOT2/L} + R^{cd}_{th,BOT2}} \tag{4.86}$$

$$Q^{cv/cd}_{MID2/L} = \frac{T^{MID2} - T^L}{R^{cv}_{th,MID2/L} + R^{cd}_{th,MID2}} \tag{4.87}$$

$$Q^{cv/cd}_{MID2/G} = \frac{T^{MID2} - T^G}{R^{cv}_{th,MID2/G} + R^{cd}_{th,MID2}} \tag{4.88}$$

$$Q^{cv/cd}_{ENV/MID1} = \frac{T^{ENV} - T^{MID1}}{R^{cv}_{th,ENV/MID1} + R^{cd}_{th,MID1}} \tag{4.89}$$

$$Q^{cv/cd}_{TOP2/G} = \frac{T^{TOP2} - T^G}{R^{cv}_{th,TOP2/G} + R^{cd}_{th,TOP2}} \tag{4.90}$$

$$Q_{A/TOP2}^{cv/cd} = \frac{T^{A} - T^{TOP2}}{R_{th,A/TOP2}^{cv} + R_{th,TOP2}^{cd}} \tag{4.91}$$

$$Q_{TOP1/A}^{cv/cd} = \frac{T^{TOP1} - T^{A}}{R_{th,TOP1/A}^{cv} + R_{th,TOP1}^{cd}} \tag{4.92}$$

$$Q_{ENV/TOP1}^{cv/cd} = \frac{T^{ENV} - T^{TOP1}}{R_{th,ENV/TOP1}^{cv} + R_{th,TOP1}^{cd}} \tag{4.93}$$

The conductive thermal resistances, R_{th}^{cd}, were evaluated using geometry-based equations [93]. The wall layers were described as cylindrical layers (Eq. 4.94), while the other bodies (floor and cover) were evaluated considering conduction through a flat plate (Eq. 4.95). Although the cover has a spherical shape, it can be considered a flat object because its thickness is much smaller than its radius.

$$R_{th}^{cd,cyl} = \frac{ln\left(\frac{OR}{IR}\right)}{2\pi\lambda HT_{MID}} \tag{4.94}$$

$$R_{th}^{cd,plt} = \frac{\delta}{\lambda A} \tag{4.95}$$

On the other hand, the convective thermal resistances, R_{th}^{cv}, were calculated as a function of the heat transfer coefficient, h (Eq. 4.96), which were estimated from empirical correlations (Appendix B).

$$R_{th}^{cv} = \frac{1}{h\ A} \tag{4.96}$$

Overall, the convective heat transfer coeffients, h, were described using natural convection correlations. As in the work of Avila-Lopez *et al.* [47], the coefficients related to the heat transfer between the cover and the biogas ($TOP2/G$), the biogas and the digestate (G/L), the air layer and the covers ($TOP1/A$ and $A/TOP2$), and the external environment and the outer cover ($ENV/TOP1$) were calculated considering natural convection with a horizontal plate (Eqs. B.9 and B.10). Besides, this method was employed to evaluate the energy transfer between the floor and the digestate

($BOT2/L$) as well. The heat convection between the walls and the digestate ($MID2/L$), the biogas ($MID2/G$), or the external air ($ENV/MID1$) were computed considering the interaction with a vertical plate (Eq. B.11).

In situations where there was also the occurrence of forced convection, the coefficients for mixed correlations were used (Eq. 4.97), as it could happen a shift between the predominance of each phenomenon according to operational conditions.The forced convection heat transfer coefficients, h_{for}, were calculated as in the work of Avila-Lopez *et al.* [47]. The energy flow between the external air and the cover ($ENV/TOP1$) was described with a correlation for a flat plat, and between the environment with the walls ($ENV/MID1$) with one for a cylinder in cross a flow. External air conditions (i.e. temperature and wind speed) that are used in this approach were obtained from meteorological data.

$$h = \left(h_{for}^3 + h_{nat}^3\right)^{1/3} \tag{4.97}$$

To evaluate h_{for} inside the air layer (A), the zone delimited by the two cover layers ($TOP1$ and $TOP2$) was described as a non-circular duct. Nu was evaluated using correlations for internal flow in a circular duct. However, the tube diameter was replaced by the hydraulic diameter (Eq. 4.98) as characteristic length in these equations (Eqs. B.15 and B.16).

$$D_h = \frac{4A_{duct}}{Per} \tag{4.98}$$

As a simplification, the central cross-section of the air zone was taken as reference (Figure 4.2). The surface, A_{duct}, was calculated as the difference of two disk segments, and the perimeter, Per, as the sum of their arc lengths. To estimate an average air velocity inside the air layer, the average volumetric flow rate was divided by A_{duct}.

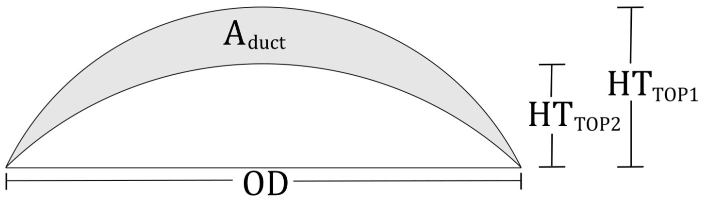

Figure 4.2: Cross-section of the central part of the covers.

4.3.2 Advection

The advection heat terms refer to the energy flow related to the mass transfer between the gas and the liquid phases. They include both the energy carried by the material stream and the latent heat involved in the phase changes (i.e. vaporization and condensation). In the liquid phase, Q_L^{adv} was calculated as a function of the direction of the mass transfer of each compound (Eqs. 4.99 and 4.100), and, in the gas phase, Q_G^{adv} was evaluated analogously (Eqs. 4.101 and 4.102).

$$Q_L^{adv} = -\sum_i \Delta\tilde{H}_{L,\,i}^{adv} F_i^{GL} \tag{4.99}$$

$$\Delta\tilde{H}_{L,\,i}^{adv} = \begin{cases} \tilde{H}_i^G\left(T^L\right) - \tilde{H}_i^L\left(T^L\right), & F_i^{GL} > 0 \\ \tilde{H}_i^L\left(T^G\right) - \tilde{H}_i^L\left(T^L\right), & F_i^{GL} < 0 \end{cases} \tag{4.100}$$

$$Q_G^{adv} = \sum_i \Delta\tilde{H}_{G,\,i}^{adv} F_i^{Gl} \tag{4.101}$$

$$\Delta\tilde{H}_{G,\,i}^{adv} = \begin{cases} \tilde{H}_i^G\left(T^L\right) - \tilde{H}_i^G\left(T^G\right), & F_i^{GL} > 0 \\ \tilde{H}_i^G\left(T^G\right) - \tilde{H}_i^G\left(T^G\right), & F_i^{GL} < 0 \end{cases} \tag{4.102}$$

4.3.3 Radiation

Two kinds of heat exchange through radiation were considered: internal and external. The former corresponded to the exchanges between the surfaces inside the digester ($TOP2$, $MID2$ and L, or $TOP1/TOP2$) and the latter considered the infrared exchanges with the surroundings and the energy uptake from solar light. Although anaerobic digesters typically work at mild conditions of temperatures, internal radiations account for a significant part of heat losses from the digestate [47, 50]. The reason for such effect is that the surface areas in industrial digesters are elevated.

Regarding the internal exchanges, the digester's interior was considered a three-surface enclosure constituted by the walls ($MID2$), the liquid surface (L) and the inner cover ($TOP2$) (Figure 4.3). It was assumed that biogas was not a participant medium, thus the gas effect on radiation was neglected. The radiation energy flow rate leaving each of these surfaces was estimated as a function of their respective view factors, surface areas and temperatures (Eqs. 4.103-4.105). These equations form a 3-equation linear system, which solution for J_L, J_{TOP2} and J_{MID2} allowed estimating Q_L^{rad}, Q_{TOP2}^{rad} and Q_{MID2}^{rad}. The view factors were evaluated according to the digester's dimensions considering a geometry of a cylinder with a spherical cap on its top [100].

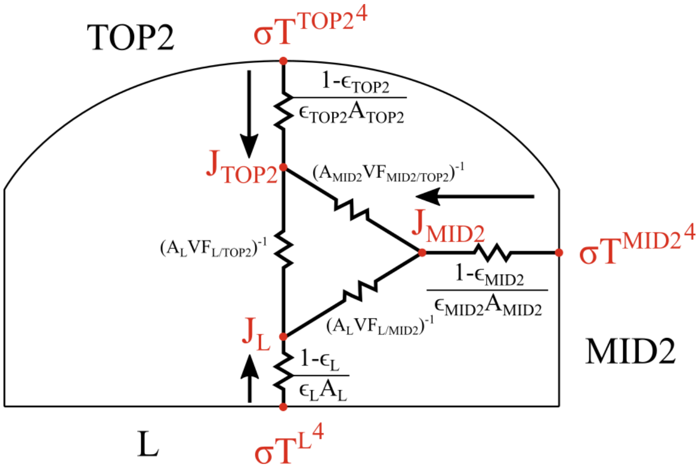

Figure 4.3: Representation of the three-surface formed by L, $MID2$ and $TOP2$ for internal radiation calculation.

$$Q_L^{rad} = \frac{\sigma T^{L^4} - J_L}{(1-\epsilon_L)\,/\,(\epsilon_L A_L)} = A_L VF_{L/TOP2}\,(J_L - J_{TOP2}) + A_L VF_{L/MID2}\,(J_L - J_{MID2}) \tag{4.103}$$

$$Q_{TOP2}^{rad} = \frac{\sigma T^{TOP2^4} - J_{TOP2}}{(1-\epsilon_{TOP2})\,/\,(\epsilon_{TOP2} A_{TOP2})} = A_L VF_{L/TOP2}\,(J_{TOP2} - J_L) + A_{MID2} VF_{MID2/TOP2}\,(J_{TOP2} - J_{MID2}) \tag{4.104}$$

$$Q^{rad}_{MID2} = \frac{\sigma T^{MID2^4} - J_{MID2}}{(1-\epsilon_{MID2})\,/\,(\epsilon_{MID2}A_{MID2})} = A_{MID2}VF_{MID2/L}\left(J_{MID2} - J_L\right) + A_{MID2}VF_{MID2/TOP2}\left(J_{MID2} - J_{TOP2}\right) \tag{4.105}$$

Similarly, the radiative exchange between the two membranes that constitute the digester's cover was evaluated considering it as an enclosure as well. In this case, however, it is formed by only two surfaces. Thus, the heat flow rate between the two covers ($TOP1/TOP2$) was evaluated according to such geometry (Eq. 4.106). The view factors were calculated using the reciprocity and the summation relations [93].

$$Q^{rad}_{TOP1/TOP2} = \frac{\sigma\left(T^{TOP1^4} - T^{TOP2^4}\right)}{\frac{1-\epsilon_{TOP1}}{\epsilon_{TOP1}A_{TOP1}} + \frac{1}{A_{TOP1}VF_{TOP1/TOP2}} + \frac{1-\epsilon_{TOP2}}{\epsilon_{TOP2}A_{TOP2}}} \tag{4.106}$$

Regarding the radiative heat exchange with the external environment, it was separated into infrared emissions and solar irradiance uptake. The first one was computed considering two terms: exchange with the sky, at T^{sky}, and with the environment, at T^{env} (Eqs. 4.107 and 4.108). The view factor to the sky was calculated using the same expression used in the work of Avila-Lopez *et al.* [47] (Eq. 4.109). The sky temperature was estimated as a function of external air temperature (Eq. 4.110) [101], and the ground and the surroundings were assumed to be both at equilibrium with the environment.

$$Q^{rad,env}_{ENV/MID1} = A_{MID1}\sigma\epsilon_{MID1}\left(VF^{sky}_{MID1}\left(T^{sky^4} - T^{MID1^4}\right) + \left(1 - VF^{sky}_{MID1}\right)\left(T^{env^4} - T^{MID1^4}\right)\right) \tag{4.107}$$

$$Q^{rad,\ env}_{ENV/TOP1} = A_{TOP1}\sigma\epsilon_{TOP1}\left(VF^{sky}_{TOP1}\left(T^{sky^4} - T^4_{TOP1}\right) + \left(1 - VF^{sky}_{TOP1}\right)\left(T^{env^4} - T^{TOP1^4}\right)\right) \tag{4.108}$$

$$VF^{sky} = 0.5\left(1 + cos\left(\psi\right)\right)\sqrt{0.5\left(1 + cos\left(\psi\right)\right)} \tag{4.109}$$

$$T^{sky} = 0.0552T^{env^{1.5}} \tag{4.110}$$

The cover, however, was treated as a spherical cap. Therefore, its view factor was obtained through integration over its surface from the cover's base until its summit (Eq. 4.111).

$$VF^{sky}_{TOP1} = \left[\frac{0.282843cos^2\left(\psi/2\right)\left(cos\left(\psi\right)+1\right)^{1.5}}{cos\left(\psi\right)}\right]^{0}_{\psi_0} \tag{4.111}$$

Besides irradiating to the environment, the external surfaces have also an energy uptake from the sun. The solar irradiance has two different parts: direct and diffuse radiation. The former is quantified from meteorological data on direct normal irradiance (DNI), which depends on the solar position and comprises the direct sunlight received. The diffuse horizontal irradiance (DHI) was used to characterize the latter and it was obtained from meteorological data as well. This energy flow is formed by the scattering of sunlight through the atmosphere and, thus, it does not have a preferential path. Therefore, the equivalent horizontal area of a tilted surface was calculated using an isotropic model [102]. A^{DHI}_{MID1} was calculated considering that the walls are perpendicular to the ground (Eq. 4.112). On the other hand, the equivalent surface of the cover was obtained by integrating the isotropic equation [102] over the cover's surface from its base (θ_0) to its top ($\pi/2$) (Eq. 4.113).

$$A^{DHI}_{MID1} = \frac{A_{MID2}}{2} \tag{4.112}$$

$$A^{DHI}_{TOP2} = \pi R^2_{cap}\left[sin(\theta) - 0.5cos^2(\theta)\right]^{\pi/2}_{\theta_0} \tag{4.113}$$

Unlike DHI, the DNI value represents the energy received by a surface perpendicular to the solar beam. The solar elevation angle (i.e. complement of the zenith) was calculated based on the simulation time and geographical coordinates (i.e. latitude and longitude) [47, 49, 50]. In this case, the equivalent surface is the projection onto the plane that is normal to the solar beam. The wall's projection was assessed by considering that only one side is illuminated by direct sunlight (Eq. 4.114). The cover's projection was estimated as a function of the altitude angle by integrating the sunlit zone (Eqs. 4.115 and 4.116).

$$A_{MID1}^{DNI} = HT_{wall,\ ag} OD sin(\alpha) \tag{4.114}$$

$$A_{TOP1}^{DNI} = \int_{0}^{z_{lim}} \left(\sqrt{R_{cap}^2 - z^2} - h_{base} sin(\alpha) + \sqrt{R_{cap}^2 - h_{base}^2 - z^2} \right) dz \tag{4.115}$$

$$z_{lim} = \sqrt{\frac{R_{cap}^2 - h_{base}^2}{sin^2(\alpha)}} \tag{4.116}$$

Finally, the radiative energy uptake from solar light was determined by summing the contributions of DNI and DHI (Eqs. 4.117 and 4.118). The total external radiative heat transfer is the sum of the contributions from solar and infrared emissions (Eqs. 4.119 and 4.120).

$$Q_{ENV/MID1}^{rad,\ sun} = \alpha_{MID1} \left(A_{MID1}^{DHI} DHI + A_{MID1}^{DNI} DNI \right) \tag{4.117}$$

$$Q_{ENV/TOP1}^{rad,\ sun} = \alpha_{TOP1} \left(A_{TOP1}^{DHI} DHI + A_{TOP1}^{DNI} DNI \right) \tag{4.118}$$

$$Q_{ENV/MID1}^{rad} = Q_{ENV/MID1}^{rad,\ sun} + Q_{ENV/MID1}^{rad,\ env} \tag{4.119}$$

$$Q_{ENV/TOP1}^{rad} = Q_{ENV/TOP1}^{rad,\ sun} + Q_{ENV/TOP1}^{rad,\ env} \tag{4.120}$$

4.3.4 Heat exchanger

In this model, it was considered that the heat exchanger that provides the required heat to the digester consisted of submerged tubes. Thus, these were characterized by their length, and internal and external diameters (Figure 4.4). The approach used was similar to the one employed in the work of Evola *et al.* [103], where an energy balance was applied on the heat exchanger's tubes (Eq. 4.82, repeated below for convenience). The heat conduction inside the tube material was considered to be relatively fast. Consequently, its temperature was assumed to be uniform throughout the tubes.

$$m^{HEX}\hat{C}p^{HEX}\frac{dT^{HEX}}{dt} = Q^{cv}_{HW/HEX} - Q^{cv}_{HEX/L} \tag{4.82 revisited}$$

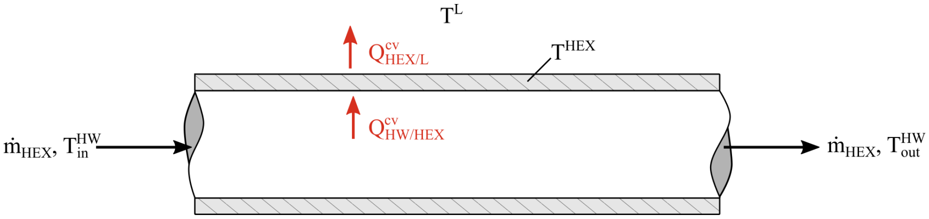

Figure 4.4: Representation of the heat exchanger. Heat fluxes involved are in red

The heat transfer coefficient inside the heat exchanger's tube was evaluated as a function of the hot water mass flow rate and temperature (Eq. 4.121). The hot water outlet temperature was calculated considering that the thermal energy transferred could be described using a LMTD equation (Eq. 4.122). The convective heat transfer coefficient, h^{HEX}_{for}, was calculated considering forced convection inside a tube using Gnielinski's correlation (Eq. B.17) and Petukhov's equation (Eq. B.18).

$$Q^{cv}_{HW/HEX} = \dot{m}_{HEX}\hat{C}_{P,H_2O}\left(T^{HW}_{in} - T^{HW}_{out}\right) \tag{4.121}$$

$$\dot{m}_{HEX}\hat{C}_{P,H_2O}\left(T^{HW}_{in} - T^{HW}_{out}\right) = h^{HEX}_{for}A_{HEX}\frac{\left(T^{HW}_{in} - T^{HEX}\right) - \left(T^{HW}_{out} - T^{HEX}\right)}{ln\left(\frac{T^{HW}_{in} - T^{HEX}}{T^{HW}_{out} - T^{HEX}}\right)} \tag{4.122}$$

$$\begin{aligned} Q^{cv}_{HW/HEX} =& \dot{m}_{HEX}\hat{C}_{P,H_2O}\left(T^{HW}_{in} - T^{HW}_{out}\right) \\ =& h^{HEX}_{for}A_{HEX}\frac{\left(T^{HW}_{in} - T^{HEX}\right) - \left(T^{HW}_{out} - T^{HEX}\right)}{ln\left(\frac{T^{HW}_{in} - T^{HEX}}{T^{HW}_{out} - T^{HEX}}\right)} \end{aligned} \tag{4.123}$$

Throughout the simulations, the digestate temperature was maintained near its set value by adjusting the mass flow rate of hot water inside the heat exchanger using a P-controller to determine its flow rate while its inlet temperature was kept constant (Eq. 4.124). For each simulation, the control parameters were calibrated manually.

$$\dot{m}_{HEX} = \dot{m}_{bias} + k_{gain}\left(T^{L}_{set} - T^{L}\right) \tag{4.124}$$

Outside the tube, $Q^{cv}_{HEX/L}$ was computed considering that the dominant mean of heat transfer inside the digestate was natural convection (Eq. 4.125), and the heat transfer coefficient using the correlation of Churchill and Chu for natural convection over a horizontal tube (Eq. B.12).

$$Q^{cv}_{HEX/L} = h^{HEX}_{nat}A_{HEX}\left(T^{HEX} - T^{L}\right) \tag{4.125}$$

4.3.5 Heat losses to the ground

The heat losses to the ground were estimated according to the norm ISO 13 370 for dynamic calculation [104]. In this methodology, the heat flow rate is evaluated considering a virtual layer that consists of a soil layer of 0.5 m with a virtual temperature at its boundary. This last parameter, T^{vi}, was evaluated according to the monthly average heat loss to the ground, $\bar{Q}_m$ (Eq. 4.126).

$$T^{vi} = \bar{T}^{L} - \frac{\bar{Q}_m}{AU} \tag{4.126}$$

$\bar{Q}_m$ was calculated through a correction of the yearly average heat transfer using the monthly average temperature, $\bar{T}_m$ (Eq. 4.127). This temperature value was estimated as a function of the monthly temperature amplitude, the average temperature and the time of the year with the minimum yearly temperature, $hoy_{T_{min}}$ (Eq. 4.128). In this equation, hoy corresponds to the simulation time converted to hours. All the values used were obtained from local weather data.

$$\bar{Q}_m = AU\left(T^L - \bar{T}_y^{ENV}\right) + H_{PE}\left(\bar{T}_y^{ENV} - \bar{T}_m^{ENV}\right) \tag{4.127}$$

$$\bar{T}_m = \bar{T}_y - \frac{T_{m,max} - T_{m,min}}{2} cos\left(2\pi\frac{hoy - hoy_{T_{min}}}{8760}\right) \tag{4.128}$$

The thermal transmittance, U, used in Eq. 4.127 was estimated with the method for basements [104]. In fact, the term AU was calculated as the sum of the contributions of the floor and the walls (Eq. 4.129). Defining B as a characteristic length (Eq. 4.130), d_f as the total equivalent thickness of the floor (Eq. 4.131), and d_{wb} the total equivalent thickness of the underground walls (Eq. 4.132), the heat transmittances were evaluated using Eqs. 4.133 and 4.134 for the ground and the walls respectively.

$$AU = A_{disk}\left(OD\right)U_{GRD/BOT} + A_{lat,cyl}\left(OD, HT_{MID,ug}\right)U_{GRD/MID} \tag{4.129}$$

$$B = \frac{A_{disk}\left(OD\right)}{0.5Per_{disk}\left(OD\right)} \tag{4.130}$$

$$d_f = \delta_{MID} + \lambda_{soil}\left(\frac{1}{h_{nat,BOT2/L}} + \frac{\delta_{BOT1}}{\lambda_{BOT1}} + \frac{\delta_{BOT2}}{\lambda_{BOT2}}\right) \tag{4.131}$$

$$d_{wb} = \lambda_{soil}\left(\frac{1}{h_{nat,MID2/L}} + \frac{\delta_{MID1}}{\lambda_{MID1}} + \frac{\delta_{MID2}}{\delta_{MID2}}\right) \tag{4.132}$$

$$U_{GRD/BOT} = \begin{cases} \frac{2\lambda_{soil}}{\pi B + d_f + 0.5HT_{MID}^{ug}} ln\left(\frac{\pi B}{d_f + 0.5HT_{MID}^{ug}} + 1\right), & d_f + 0.5HT_{MID}^{ug} < B \\ \frac{\lambda_{soil}}{0.457B + d_f + 0.5HT_{MID}^{ug}}, & d_f + 0.5HT_{MID}^{ug} \geq B \end{cases} \tag{4.133}$$

$$U_{GRD/MID} = \frac{2\lambda_{soil}}{\pi HT^{ug}_{MID}} \left(1 + \frac{0.5 d_f}{d_f + HT^{ug}_{MID}}\right) \tag{4.134}$$

H_{PE} of Eq. 4.127 corresponds to the periodical heat transfer coefficient, which was calculated with Eq. 4.135. The periodic penetration depth, L_{pen}, was calculated as a function of properties of the soil (Eq. 4.136).

$$\begin{aligned} H_{PE} =& 0.37 Per_{disk}(OD)\lambda_{soil} \\ & \left(e^{-\frac{HT^{ug}_{MID}}{L_{pen}}} + ln\left(\frac{L_{pen}}{d_f} + 1\right) + 2\left(1 - e^{-\frac{HT_{MID}}{L_{pen}}} ln\left(\frac{L_{pen}}{d_{wb}} + 1\right)\right)\right) \end{aligned} \tag{4.135}$$

$$L_{pen} = \sqrt{\frac{3.15\ 10^7\ \lambda_{soil}}{\pi \rho_{soil} \hat{C}_{P,soil}}} \tag{4.136}$$

To evaluate the heat losses to the ground, the effective thermal resistances of the ground were estimated from the thermal transmittances and the thermal resitance of the floor and the walls (Eqs. 4.137 and 4.138).

$$R_{th}^{GRD/BOT} = \frac{\frac{1}{U_{GRD/BOT}} - \frac{1}{h_{nat,BOT2/L}} - \frac{\delta_{BOT1}}{\lambda_{BOT1}} - \frac{\delta_{BOT2}}{\lambda_{BOT2}}}{A_{disk}(OD)} \tag{4.137}$$

$$R_{th}^{GRD/MID} = \frac{\frac{1}{U_{GRD/MID}} - \frac{1}{h_{nat,MID2/L}} - \frac{\delta_{MID1}}{\lambda_{MID1}} - \frac{\delta_{MID2}}{\lambda_{MID2}}}{A_{lat,cyl}(OD, HT^{ug}_{MID})} \tag{4.138}$$

Finally, the heat transfer flow rates were estimated using these thermal resistances (Eqs. 4.139 and 4.140).

$$Q^{cd}_{GRD/BOT1} = \frac{T^{vi} - T^{BOT1}}{R_{th}^{GRD/BOT} + 0.5\frac{\delta_{BOT1}}{\lambda_{BOT1} A_{disk}(OD)}} \tag{4.139}$$

$$Q^{cd}_{GRD/MID2} = \frac{T^{vi} - T^{MID2}}{R_{th}^{GRD/MID} + 0.5\frac{ln(\frac{OR}{IR})}{2\pi HT^{ug}_{MID}}} \tag{4.140}$$

4.3.6 Reaction heat

In general, the heat of reaction was computed as a function of the partial enthalpies of the participating species (Eq. 4.141). In ADM1-W, however, the macromolecules of carbohydrates and proteins do not have a defined molecular structure and, thus, their formation enthalpies are not defined. For these compounds, such values were estimated from the standard hydrolysis heat of glycosidic [105] and of peptide bonds [106] respectively. In the case of lipids, the tripalmitin was used as a reference molecule [33, 39]. Thus, the properties of such compound were used [107]. For amino acids, glutamine ($C_5H_{10}O_3N_2$) was used as reference molecule [95, 108, 109] as this compound has the closest molecular formula to AA ($C_5H_{9.625}O_{2.5}N_{1.25}$). The reaction heats calculated at 298.15 K are exhibited in Table 4.4.

$$\Delta\tilde{H}_{R,\,j}\left(T^L\right) = \sum_i \nu_{i,\,j}\tilde{H}_i^L\left(T^L\right) \tag{4.141}$$

Table 4.4: Standard reaction heats at 298.15 K

Parameter	$\Delta\tilde{H}_{R,\,j}\left[kJ\ mol^{-1}\right]$
HY-CH	- 4.00
HY-PR	- 7.50
HY-LI	+ 93.40
AI-SU	- 30.93
AI-AA	+ 229.59
AI-LCFA	+ 929.69
AE-HVa	+ 115.17
AE-HBu	+ 116.24
AE-HPr	+ 198.56
ME-HAc	+ 17.92
ME-H_2	- 62.26
HAc SRB	- 99.16
H_2 SRB	- 89.54
Cell decay	-237.90

4.4 Gasholder model

It was considered that the biogas is stored in an air-inflated double-membrane gasholder, which is one of the most widespread structures in biogas plants [110]. This gasholder consists of two polymeric membranes that delimits an air layer (A) and another one with biogas (G) (Figure 4.5). The former is kept inflated by continuous air injection through a blower (F_{in}^{A} in Eq. 4.65). The working range of the blower curve was modeled as a quadratic function (Eqs. 4.142 and 4.143). If not stated otherwise, the polynomial coefficients used for a, b, and c were respectively: - 1.77 10^{-5}, 1.60 10^{-2}, and 3.93. The volumetric flow rate is calculated in $Nm^3\ h^{-1}$ and the overpressure inside the air layer, ΔP, is used in mbar.

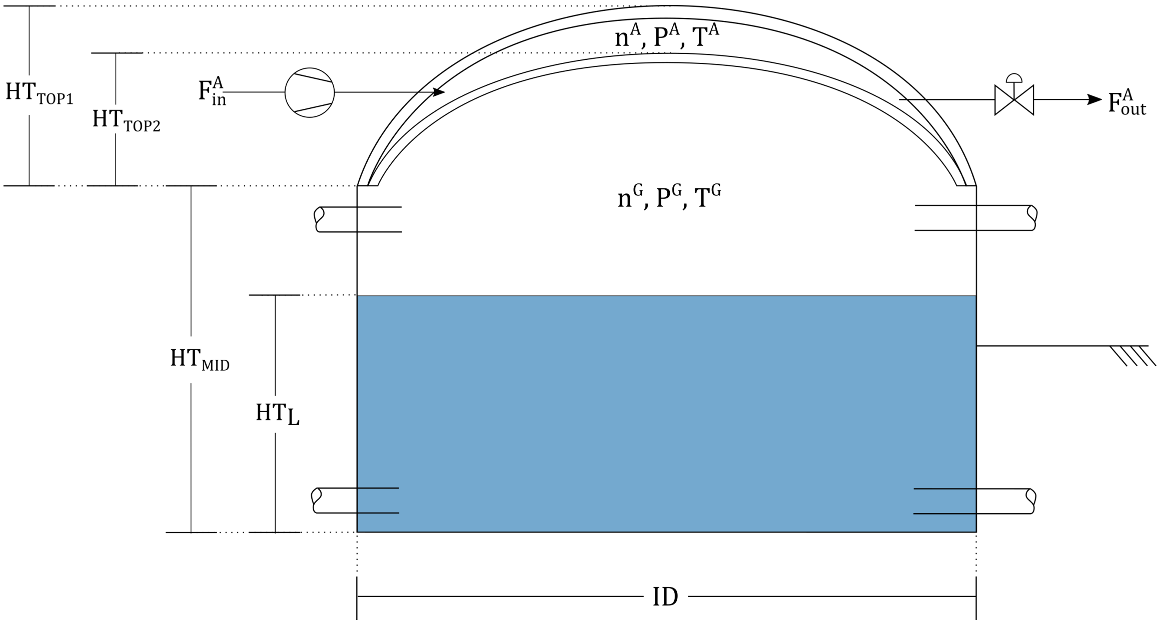

Figure 4.5: Representation of the double-membrane gasholder.

$$\Delta P = a\dot{V}_{in}^{A^2} + b\dot{V}_{in}^{A} + c \tag{4.142}$$

$$\dot{V}_{in}^{A} = \frac{-b - \sqrt{b^2 - 4a\left(c - \Delta P\right)}}{2a} \tag{4.143}$$

The air outlet flow rate was estimated with a valve equation (Eq. 4.144). The valve constant generally used was 380 $Nm^3\ h^{-1}\ mbar^{-0.5}$. The operating pressure of the double-membrane is given by the intersection of the blower and the valve curves (Figure 4.6).

$$\dot{V}^{A}_{out} = C_V \sqrt{\Delta P} \tag{4.144}$$

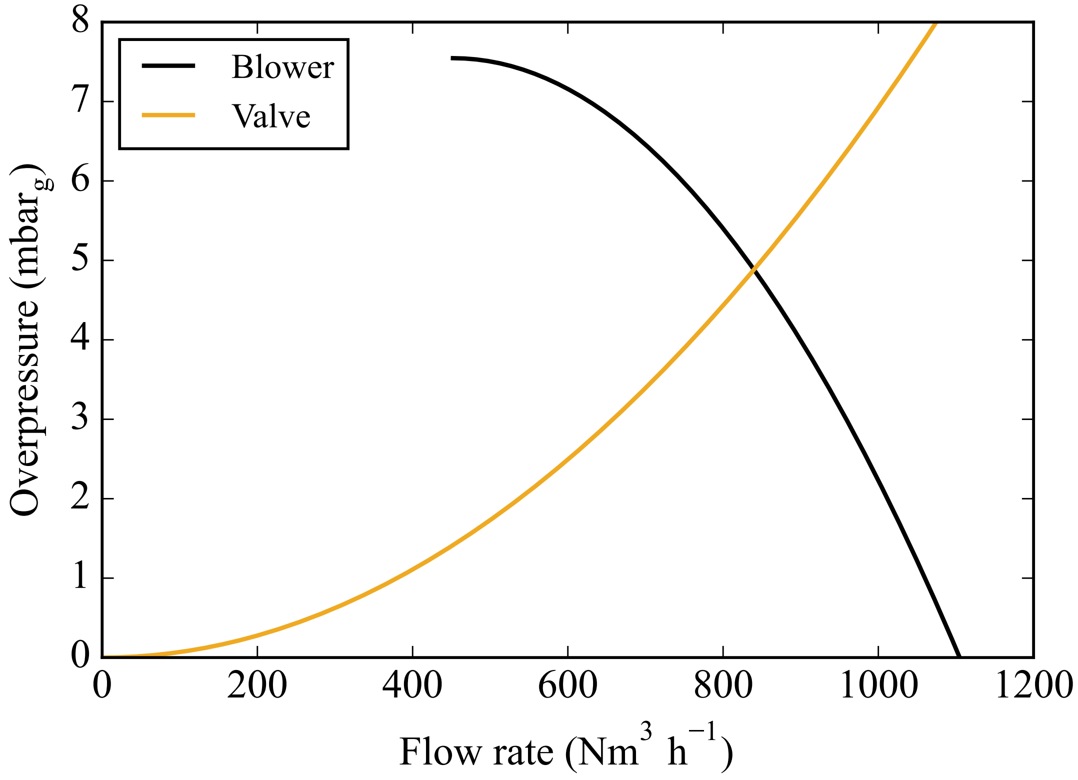

Figure 4.6: Air blower and valve curves with standard coefficient values. The operating conditions are given by the intersection of both curves (ΔP = 4.88 mbar and $\dot{V}^{A}$ = 839.8 Nm^3 h^{-1}).

The air layer was assumed to be always fully inflated. Therefore, its height, H_{TOP1}, was considered constant, which implicates that the total volume of the digester is constant as well (Eq. 4.145). Regarding the biogas layer, two regimes were considered: isochoric and mobile. The former corresponds to when the air volume is at its threshold values, either maximum or minimum. In this case, the intermediary membrane, $TOP2$, behaved as a rigid wall. Thus, the pressures of each compartment were calculated directly from the ideal gas law (Eqs. 4.146 and 4.147), with V^A at either V^A_{min} or V^A_{max}.

$$V^{Total} = V^A + V^G + V^L = cte \tag{4.145}$$

$$P^A = \frac{n^A R T^A}{V^A} \tag{4.146}$$

$$P^G = \frac{n^G R T^G}{V^G} \tag{4.147}$$

If the air volume was within its threshold values, $TOP2$ was considered to be freely mobile. All forces related to membrane weight or its displacement were neglected. Consequently, the pressures in both sides were considered as equal (i.e. $P^A = P^G$). From this, pressures and volumes could be evaluated considering ideal gas behavior (Eqs. 4.146-4.148).

$$V^A = \left(V^{Total} - V^L\right) \frac{n^A T^A}{n^A T^A + n^G T^G} \tag{4.148}$$

The threshold values of V^A were set by imposing minimum and maximum values to HT_{TOP2}. While its minimum was considered to be 0.5 m, its maximal value was estimated as 0.85 HT_{TOP1}, based on the ratio of usable and total volumes from a gasholder catalog [111]. The volume delimited by the cover was calculated considering it is a spherical cap (Eq. 4.149, with V_{cap} from Eq. A.2).

$$V^A = V_{cap}\left(ID,\ HT_{TOP1}\right) - V_{cap}\left(ID,\ HT_{TOP2}\right) \tag{4.149}$$

4.4.1 Gas storage control

If more than one gasholder is present, an active gas management was employed to keep all gas storages at a similar filling level [112]. The digester with the highest pressure is the main biogas storage (Fig. 4.7). The operating point of the double-membrane is kept constant. However, the pressure of the secondary ones is controlled in order to adjust the biogas flow rate between the digesters. The gas filling level, LVL^G, was calculated considering only the volume inside the spherical cap delimited by $TOP2$ (Eq. 4.150). In doing so, LVL^G does not vary with the liquid level inside the digester. Moreover, the gas volume inside the cylindrical part of the digester does not serve as storage for the biogas.

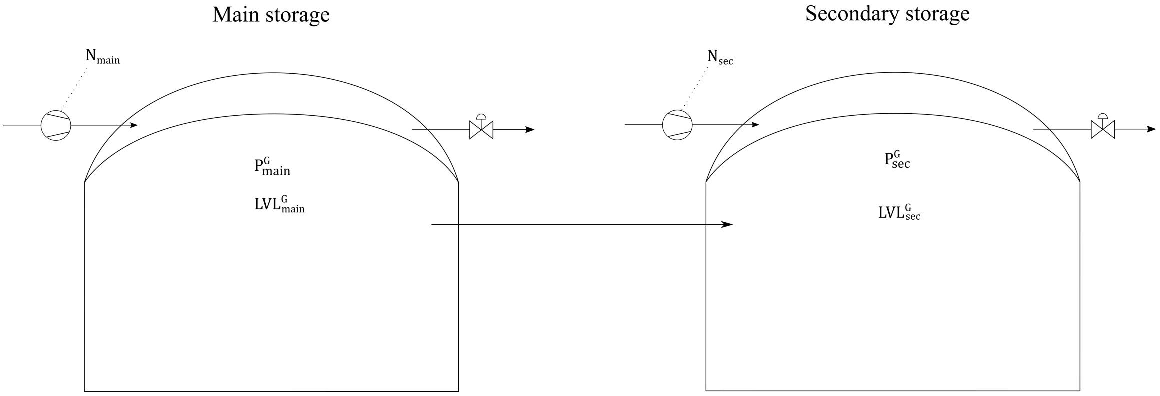

Figure 4.7: Two digesters in series. The gasholder with the highest pressure is the main gas storage.

$$LVL^G = \frac{V^G - \pi \left(HT_{MID} - HT_L\right) \frac{ID^2}{4}}{V_{cap}\left(ID,\ HT_{TOP1,max}\right)} \tag{4.150}$$

The gas flow rate between the digesters was calculated considering a flow inside a tube. The fluid velocity, u^G, was calculated from the pressure difference and the friction losses inside the tube (Eq. 4.151), and the molar flow rate, F^G_{pipe}, from the ideal gas law (Eq. 4.152).

$$P^G_{main} - P^G_{sec} = \frac{\rho^G u^{G^2}}{2} \left(\sum \zeta + 4f \frac{L_{pipe}}{ID_{pipe}} \right) \tag{4.151}$$

$$F^G_{pipe} = u^G \frac{\pi ID^2_{pipe}}{4} \frac{P^G}{RT^G} \tag{4.152}$$

The Fanning friction factor was calculated using the Colebrook formula (Eq. 4.153) [113]. Although, biogas is actually a compressible fluid, it can be considered incompressible as the pressure differences are relatively low in biogas plants [112]. Finally, the values for frictional losses in pipeline elements, ζ, can be found in the literature [96]. Generally, 1.5 was used in simulations (i.e. 0.5 for the entrance and 1.0 for the exit).

$$\frac{1}{\sqrt{f}} = -4log \left(\frac{\epsilon}{3.7ID_{pipe}} + \frac{1.256}{Re\sqrt{f}} \right) \tag{4.153}$$

In secondary gas storages, the pressure can be controlled either by adjusting the air blower speed or the opening of the outlet valve [112]. Here, only the former was manipulated through the simulations. Changes in blower speed, N, were considered to translate its characteristic curve vertically (Figure 4.8). In Eq. 4.142, such effect corresponds to changes in the linear coefficient c. When N is changed, the new operating point can be found using the Fan Laws (Eqs. 4.154 and 4.155) [114]. Defining κ as the variation of the linear coefficient (Eq. 4.156), the new characteristic curve can be calculated by summing κ to the linear coefficient of the original equation (Eq. 4.157).

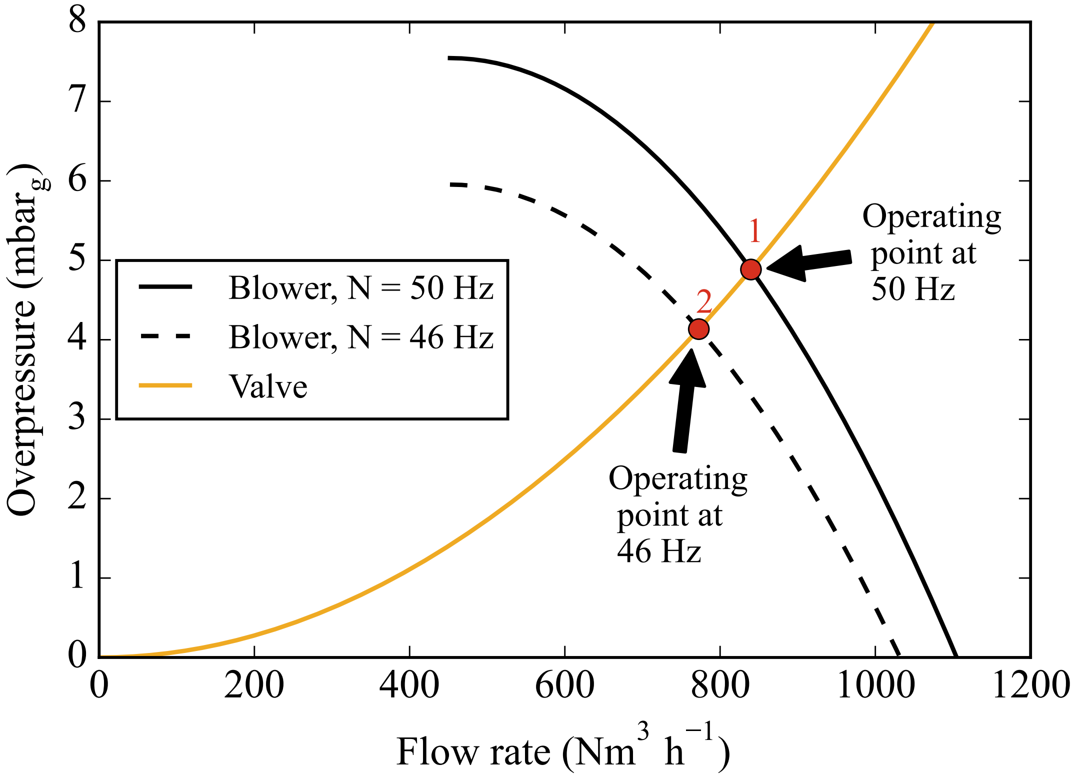

Figure 4.8: Characteristic curve of air blower at different rotation speeds. The operating points 1 and 2 for each blower curve are indicated with red dots.

$$\dot{V}_2 = \dot{V}_1 \frac{N_2}{N_1} \tag{4.154}$$

$$\Delta P_2 = \Delta P_1 \left(\frac{N_2}{N_1} \right)^2 \tag{4.155}$$

$$\Delta P\left(\dot{V}_2\right) - \Delta P_2 = a\dot{V}_2^2 + b\dot{V}_2^2 + c - \Delta P_1 \left(\frac{N_2}{N_1}\right)^2 = \kappa \tag{4.156}$$

$$\Delta P_{N_2} = a\dot{V}^2 + b\dot{V} + c + \kappa \tag{4.157}$$

The blower speed in the secondary gas storages were controlled using a P-controller on the gas level (Eq. 4.158). The control parameters used were calibrated manually for each simulation.

$$N = N_{bias} + k_{gain}\left(LVL^G_{main} - LVL^G_{sec}\right) \tag{4.158}$$

4.5 Outlet flow rate

The liquid and gas outlet flow rates were calculated using a P-controller. The first one was evaluated according to the liquid volume inside the digester (Eq. 4.159). On the other hand, the gas flow rate was calculated as a function of the gas level (Eq. 4.160), unless it entered another the headspace of another digesters. In this case, it was calculated from the pressure difference considering the flow inside a tube, as previously described in Section 4.4.1.

$$F^L_{out} = F^L_{bias} + k_{gain}\left(V^L_{set} - V^L\right) \tag{4.159}$$

$$F^G_{out} = F^G_{bias} + k_{gain}\left(LVL^G_{set} - LVL^G\right) \tag{4.160}$$

4.6 Model implementation

The digester model consists of 49 differential and 1 algebraic equations per digester, which are linked to the main variables that are solved by the solver (Table 4.5). Other variables (e.g. heat fluxes, outlet flow rates, etc.) were explicitly calculated as a function of these main variables. The model was implemented in Fortran, and the differential-algebraic system of equations was solved using DASPK [115]. The relative and absolute tolerances were both set at 10^{-6}. The Jacobian matrix is calculated by numerical perturbation by DASPK.

Table 4.5: Main variables and their respective equations of the digester model. These equations were solved using DASPK.

Variables	Equations	Number of equations
n_i^L	4.63	30
n_i^G	4.64	6
n^A	4.65	1
T^L	4.73	1
T^G	4.74	1
T^A	4.75	1
T^{TOP1}	4.76	1
T^{TOP2}	4.77	1
T^{MID1}	4.78	1
T^{MID2}	4.79	1
T^{BOT1}	4.80	1
T^{BOT2}	4.81	1
T^{HEX}	4.82	1
T_a	4.55	1
C_{H^+}	4.58	1
	Total	**49**

4.7 Model validation

The kinetics and the thermal part of the model were validated separately against experimental data from the literature. The prediction performance of simulations were quantified using the relative error (RE) (Eq. 4.161).

$$RE = \left| \frac{\left(Y^{exp} - Y^{sim}\right)}{Y^{exp}} \right| \tag{4.161}$$

4.7.1 Kinetic validation

The kinetic model was validated against experimental data of methane and biogas production in batch degradation of agricultural biomasses (maize (IM), rice straw (PR) and triticale (IT) silages) [116], and data of biogas production in a continuous large-scale agricultural biogas plant fed with maize silage and pig and cattle manure [77].

Lab-scale validation

The batch tests were carried out in 2.0 L flasks at 313.15 K during 60 days with manual agitation once a day at least. To convert the compositions from the work of Menardo *et al.* [116], the protein weight was calculated as 6.25 times the nitrogen mass [117] and the lipid content in each substrate was taken as the average value for each kind: 2% VS for IM [77, 118], 1.5% VS for PR [119, 120] and 2% VS for IT [118, 121]. Carbohydrates (CH) were considered to be composed by starch and fibers. The starch content was determined in order to match the mass balance on the volatile solids. Furthermore, lignin and part of cellulose and hemicellulose were considered to be non-degradable (CHI) [37, 77]. The degradability of cellulose and hemicellulose, d, was employed as an adjustment parameter and its value was evaluated manually for each feedstock in order to fit the simulation results with the experimental data. The values used for d were: 0.70 for IM, 0.72 for IT and 0.60 for PR. To simulate the batch tests, the results from a continuous simulation were used as inoculum composition, which was employed analogously to the experimental method (proportion of 2:1 in terms of VS related to the feedstock). The methane and biogas production from these simulations were subtracted by the results of a blank test with only the inoculum, isolating the part that corresponded to the feedstock degradation. (Figure 4.9 (a)-(d))

Using only one adjustment parameter, the batch simulations yielded results close to the experimental values for periods longer than 15 d (Figure 4.9). Indeed, RE on methane and biogas volume were lower than 5% for all feedstocks after such period. However, the model overestimated the initial production. Better results could have been obtained if the kinetic parameters were calibrated using the experimental data, but this was out of the scope of this work. This indicates that the model predicts higher reaction rates compared to the experimental degradation rate, but the stoichiometries adopted are coherent, as final methane and biogas volumes matched with the measured values. In part, the higher degradation rates can be justified by the use of default parameters of ADM1, which were originally obtained to simulate the degradation of sewage sludge in wastewater treatment context [33]. However, agricultural biomasses are more recalcitrant to AD, as they contain a higher content of fibers [77]. In addition, both in ADM1 and in ADM1-W, the intermediary products generated by the bioreactions are promptly available to other microorganisms, but such compounds

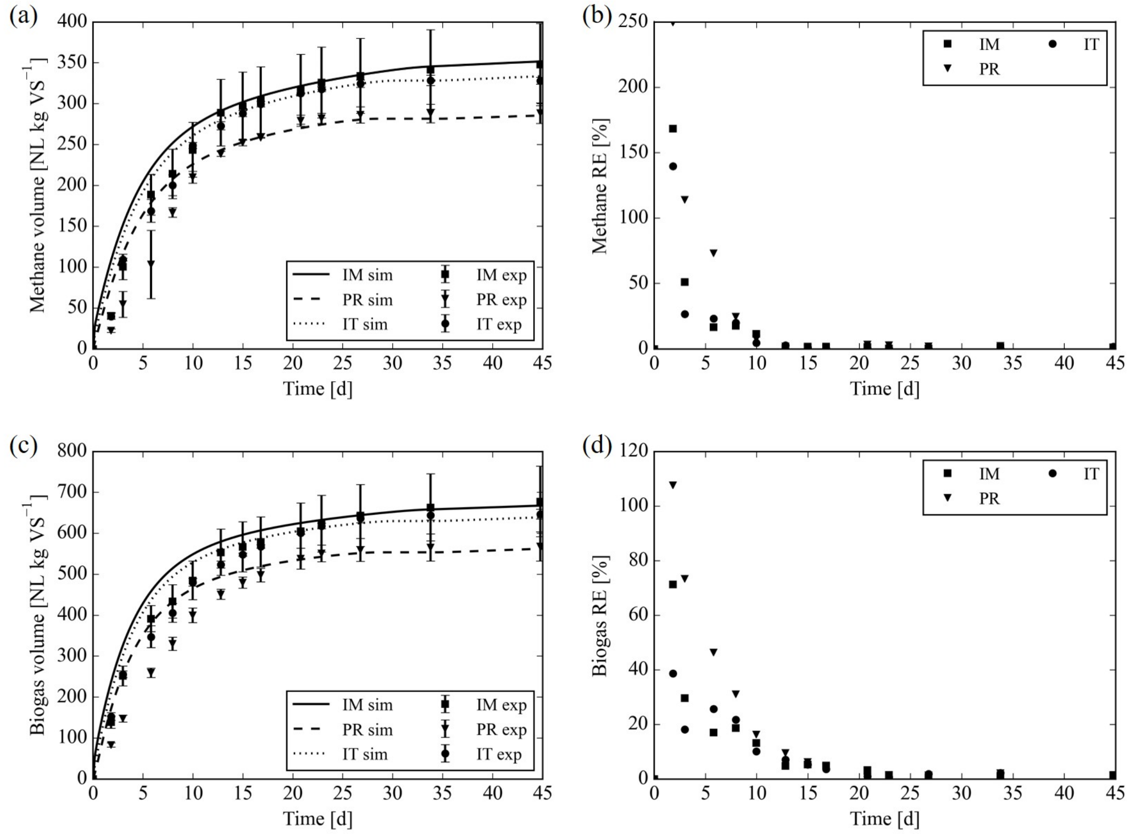

Figure 4.9: Experimental and simulation results of cumulative batch methane and biogas production from the degradation of maize silage (IM), rice silage (PR) and triticale silage (IT) [116].

need to diffuse inside the digestate so that they can be degraded [77].

Large scale validation

The second set of data corresponded to biogas production measurements from a biogas plant with 4 digesters and 2 post-digesters operating at a temperature of 39 °C [77]. Similarly to the assumption made for the batch tests, CH was calculated as starch plus fibers. PR and LI were obtained directly from the reported compositions. An average value of 0.7 was used for d. In this case, the initial conditions of the digester were obtained by simulating with the starting feedstock composition in a loop of 30 days so that the digestate composition stabilized.

In stable operation, the model managed to simulate the biogas production of the continous biogas plant (Figure 4.10 (a) and (b)). Overall, the average RE was 11.6%, but the highest discrepancies occurred between the day 215 and 250, due to a drastic reduction in the inlet feed flow rate [77]. Compared to the experimental values, the kinetic model reacts much faster to changes in the biomass input. The minimum biogas production occured at day 223 in simulation, while it happened 14 d later in reality. Nevertheless, the model managed to predict a similar drop in biogas production, simulating a minimal at around 4900 Nm^{3}d^{-1} compared to a reduction to around 4000 Nm^{3}d^{-1} in the measured values. These results are coherent with the ones from the batch simulations, indicating that ADM1-W can be used to simulate the AD in agricultural biogas digester at stable conditions, but it also has a limitation to simulate strong fluctuations in the feedstock, as the model has a tendency to react faster compared to real digesters.

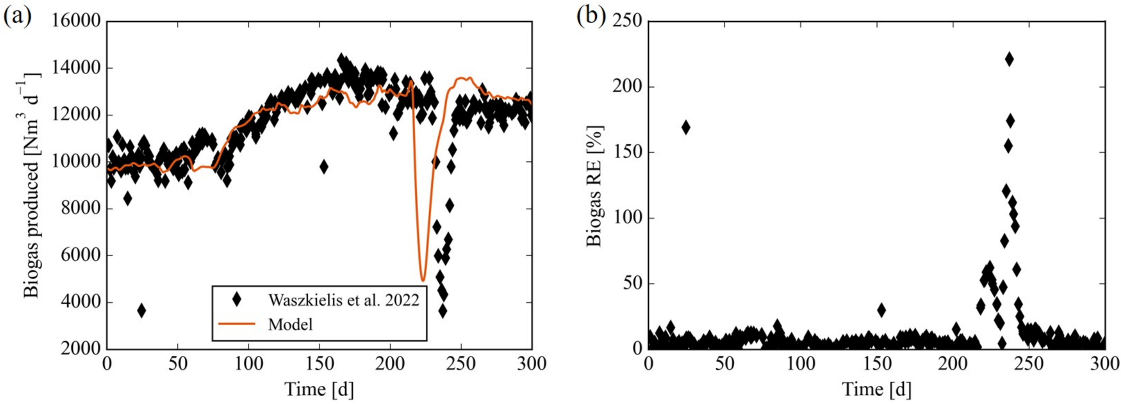

Figure 4.10: Experimental and simulation results of continuous digestion at an industrial scale agricultural biogas plant [77].

4.7.2 Thermal validation

In the work of Avila-Lopez *et al.* [47], they have developed a thermal model and validated it with experimental values from a large-scale plant (Biometharn, Aiguefonde, France). This industrial unit was composed by two digesters in series, both with a double-membrane gasholder. Although the majority of data they used was confidential, it was reported in their publication the monthly values of heat demand of the digesters' heat exchangers. Thus, to evaluate the performance of thermal part of the dynamic model developed here, these data were compared with the model predictions (Figure 4.11). The digesters' specifications and operational parameters were based on their work [47] (Table 4.6)and the meteorological data were collected for the year 2021 at the plant location using Solcast [122].

Table 4.6: Specifications of the digester and the post-digester.

Specification	Digester	Post-digester	Unit
Shaft work of stirrer	13.5	3.6	kW
Digester internal diameter	25.0	18.0	m
Total wall height	6.0	6.0	m
Underground wall height	2.5	2.5	m
Outer cover height	5.0	3.6	m
Max inner cover height	4.25	3.06	m
Min inner cover height	0.5	0.5	m
Wall layer 1 thickness (insulation)	0.14	0.14	m
Wall layer 2 thickness	0.2	0.2	m
Floor layer 1 thickness	0.1	0.1	m
Floor layer 2 thickness	0.1	0.1	m
Inner cover thickness	0.005	0.005	m
Outer cover thickness	0.005	0.005	m
Internal wall emissivity	0.94	0.94	
External wall emissivity	0.86	0.86	
External wall absorvity	0.74	0.74	
Internal cover emissivity	0.86	0.86	
External cover emissivity	0.86	0.86	
External cover absorvity	0.74	0.74	
Digestate emissivity	0.8	0.8	
Heat exchanger’s tube length	240.0	150.0	m
Heat exchanger’s tube internal diameter	0.05	0.05	m
Heat exchanger’s tube outer diameter	0.055	0.055	m
Heat exchanger’s tube density	7854	7854	kg m^{-3}

Overall, the model predictions were similar to experimental values, especially during the second semester. The RE ranged from 0.2% to 19.3%, with an average at 6.5%. Although the thermal model is similar to the work of Avila-Lopez *et al.* [47], in their work the heats of reactions were considered for the total degradation of the macronutrients into biogas following the approach employed by Lindorfer *et al.* [123]. Here, however, a dynamic kinetic model (ADM1-W) was coupled with the thermal model and the enthalpy changes for each bioreaction taking place in the digester were computed from the enthalpy difference between products and reagents.

Furthermore, the feed parameters were available only as an average for each season (winter, spring, summer and fall), while they have used daily values, which may have contributed to a better fit of their model. Besides that, their model also considered the impact of rain in heat losses, which was not accounted for here. Nevertheless, the predictions of the dynamic model (Figure 4.11)

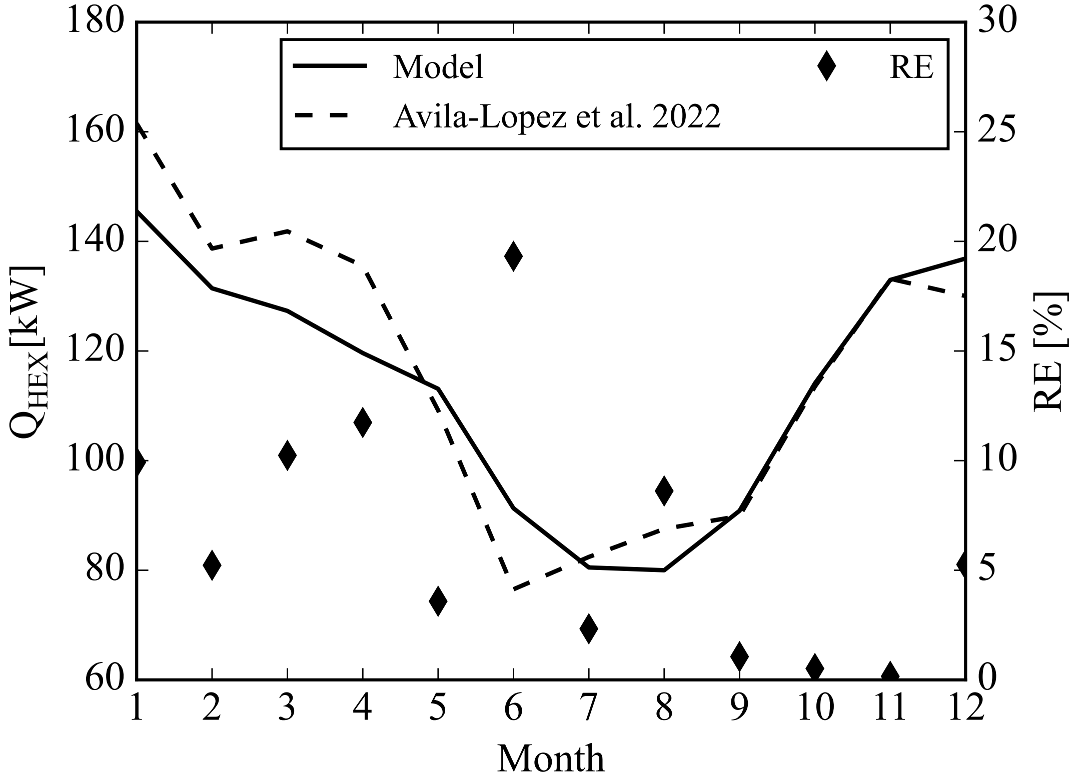

Figure 4.11: Model results and experimental data of the monthly heat input in the heat exchangers of the two digesters during the year of 2021 [47].

followed the same trend and had values close or in the same order of magnitude of the experimental data.

4.8 Conclusions

In this chapter, a dynamic model of an anaerobic digesters was developed and validated against experimental data from the literature. Overall, the model manages to predict with a good agreement both the biogas production and the thermal behavior of a digester, specially under stable conditions. However, the kinetic model used has some limitations in adequately representing the dynamic biogas production under strong variations of feedstock.

CHAPTER 5

BIOMETHANE AND POWER-TO-GAS MODELING

In a biomethane plant, the biogas produced in the digester is cleaned and then upgraded before injection into the gas grid. In the upgrading unit, a CO_2 rich stream is obtained, which can be used in a methanation reactor with H_2 to produce CH_4 as well. This second scenario will be referred as a power-to-gas case (P2G), given that H_2 would be produced by water electrolysis. To study these scenarios, additional units needed to be integrated to the digester. These models are described in this chapter.

5.1 Biomethane unit

To study the biomethane production from biogas, a reference plant structure for the industrial plant was used (Figure 5.1). The biogas production part was composed of a digester and a post-digester in series. The gas produced in these reactors would be cleaned (i.e. removal of H_2O, H_2, NH_3 and siloxanes) in a condenser then an activated carbon filter. Then, the biogas upgrading to biomethane would be carried out in a three-stage membrane separator.

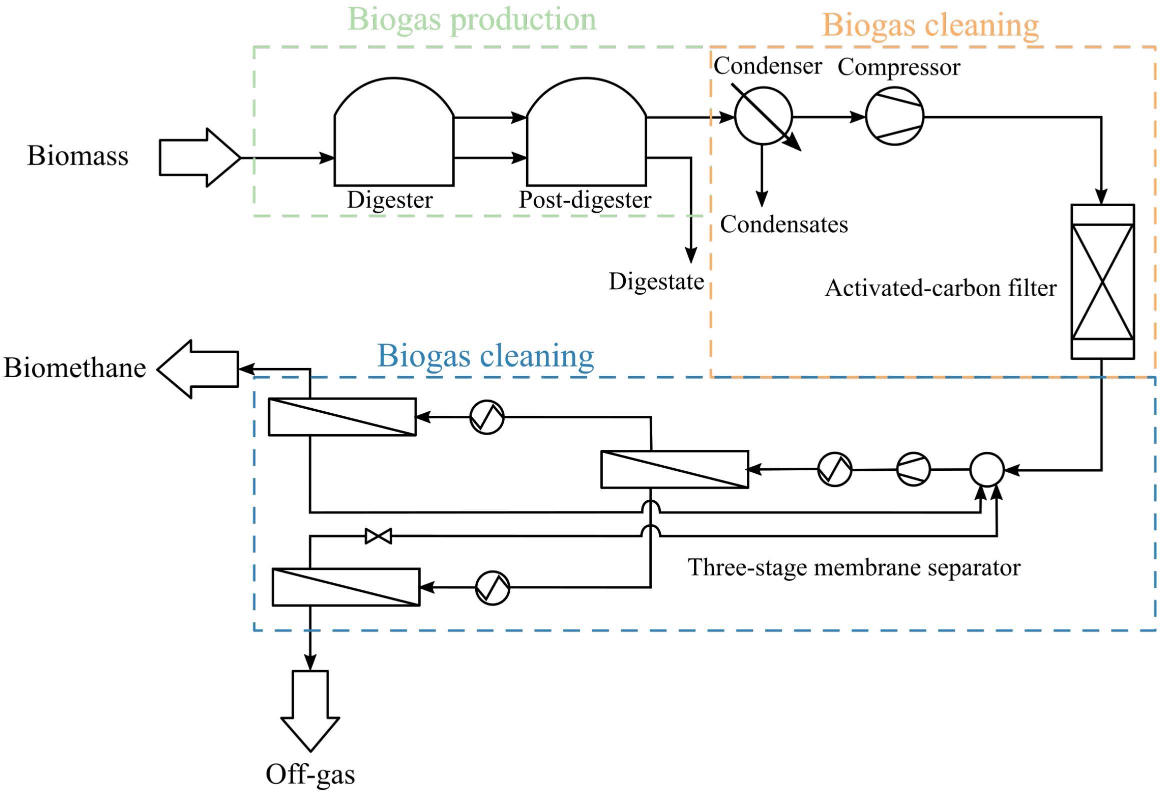

Figure 5.1: Scheme of the reference biomethane plant. The main sections of this unit are highlighted with dashed lines.

5.2 Power-to-gas unit

To consider a P2G scenario, a catalytic methanation reactor was integrated to the biomethane plant (Figure 5.2). The off-gas coming from the membrane unit would be mixed to hydrogen in stoichiometric proportions (i.e. $4\ H_2 : 1\ CO_2$), compressed, and heated before entering the first reactor. To shift the reaction equilibrium, the products of the first reactor would be sent to a chiller, where part of the water vapor formed would be condensated, before being heated and sent to a second catalytic reactor. Finally, the product gas would be sent to another chiller to condensate the H_2O again before being able to be injected into the gas grid.

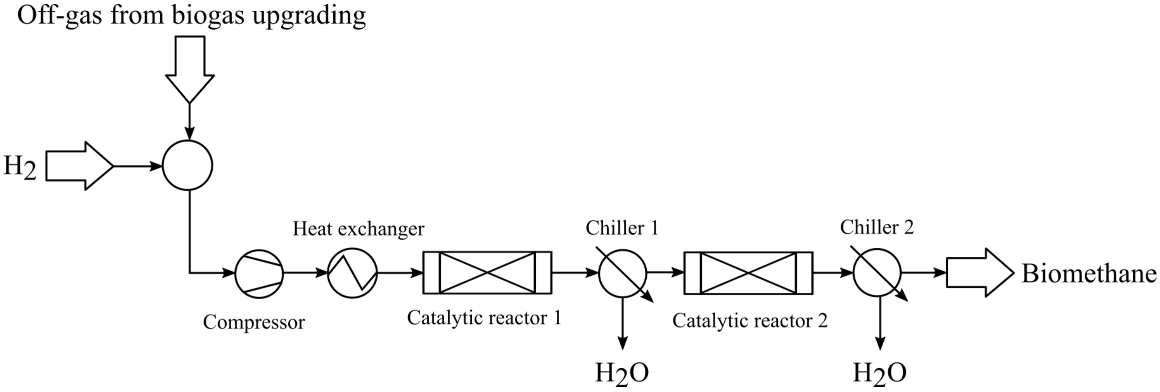

Figure 5.2: Scheme of the reference P2G plant.

5.3 Unit models

In all models, ideal gas behavior was adopted due to low operating pressure. Except for the methanation reactor, the all other units, as for instance, the membrane separator and the chiller, were assumed to work in a pseudo-stationary regime. Thus, for these blocks, no accumulation occurred inside them during any simulation time. For the methanation reactor, a 1-D dynamic model was used, as it will be further explained in Section 5.3.6. The notation used to refer to each model block when setting up a simulation scenario is presented in Table 5.1.

5.3.1 Biogas cleaner

The biogas cleaning unit (BGC) was modeled using a simple approach. The steps of water condensation and impurities removal in activated-carbon filters were merged in only one block, which was modeled as a perfect separator (Fig. 5.3).

In BGC, the raw biogas coming from the digesters, F_{in}^{G}, is cooled down to T_{out} and it was considered that all H_2O, NH_3 and H_2S contained in the inlet gas would leave in the condensate stream, F_{out}^{L}, also at T_{out}. In this case, the flow rate of the outlet streams can be obtained directly from the inlet (Eqs. 5.1 and 5.2).

$$F_{out}^{G} y_{out,i} = \begin{cases} F_{in}^{G} y_{in,i},\ i \in \{H_2, CH_4, CO_2, O_2, N_2\} \\ 0,\ \text{otherwise} \end{cases} \tag{5.1}$$

Table 5.1: Model element notation.

ID	Meaning	Symbol
GST	Gas stream	→
LST	Liquid stream	→
DIG	Digester	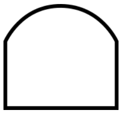
CHL	Chiller	
CMP	Compressor	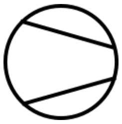
BGC	Biogas cleaner	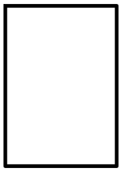
GHT	Gas heat exchanger	
3-MEM	Three-stage membrane	
CAT	Methanation reactor	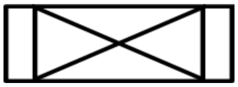

$$F_{out}^{L} x_{out,i} = \begin{cases} F_{in}^{G} y_{in,i}, \ i \in \{NH_3, H_2O, H_2S\} \\ 0, \text{otherwise} \end{cases} \tag{5.2}$$

The heat exchanged, Q_{cool}, was calculated with an energy balance (Eq. 5.3) and the electricity required to run this unit, Po_{el}, was estimated considering an energy performance ratio of 7 (Eq. 5.4) [53].

$$Q_{cool} = \sum_i -F_{in}^{L} y_{in,i} \tilde{H}_i^G \left(T_{in}\right) + F_{out}^{G} y_{out,i} \tilde{H}_i^G \left(T_{out}\right) + F_{out}^{L} x_{out,i} \tilde{H}_i^L \left(T_{in}\right) \tag{5.3}$$

$$Po_{el} = \frac{Q_{cool}}{7} \tag{5.4}$$

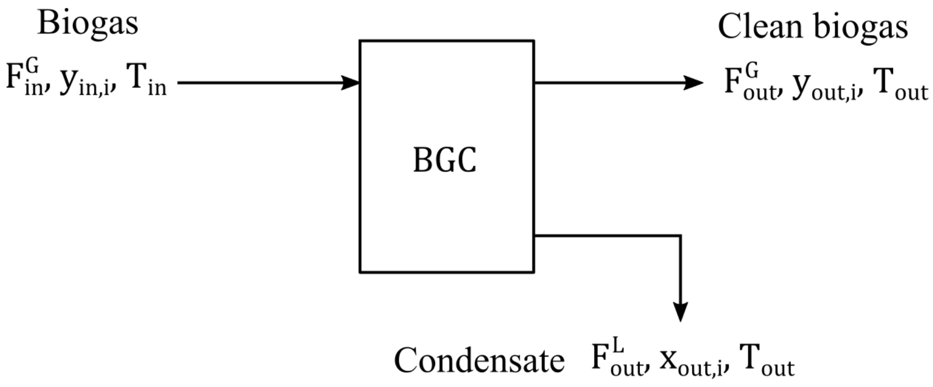

Figure 5.3: Scheme of a biogas cleaner.

5.3.2 Compressor

Compressors serve to increase the pressure of a gas stream (Fig. 5.4). This equipment was modeled using an isentropic model for the compression [124]. For a compressor with an isentropic efficiency of η_{ise}, the outlet temperature was calculated from the feed temperature and the pressure ratio (Eq. 5.5). The polytropic coefficient, κ, was calculated supposing ideal gas mixture (Eq. 5.6). As a simplification, the heat capacities were supposed constant in this unit and they were evaluated at the average temperature between the suction and the discharge values.

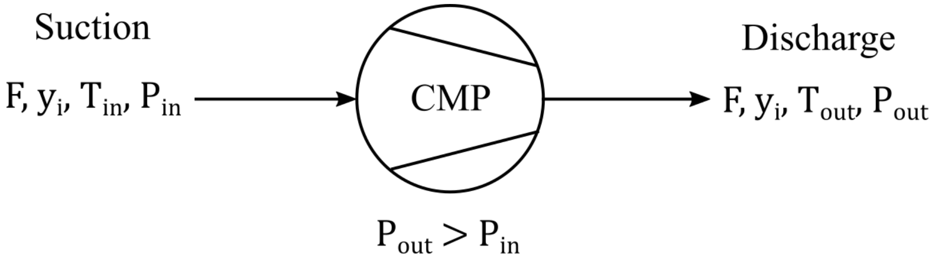

Figure 5.4: Scheme of a compressor.

$$T^G_{out} = \frac{T^G_{in}}{\eta_{ise}} \left[\left(\frac{P_{out}}{P_{in}} \right)^{\frac{\kappa-1}{\kappa}} - 1 \right] + T^G_{in} \tag{5.5}$$

$$\kappa = \frac{\sum_i y_i C_{Pi}}{\sum_i y_i C_{Pi} - R} \tag{5.6}$$

The electric power required, Po_{el}, was estimated from the enthalpy change, adopting an electric efficiency value η_{el} (Eq. 5.7).

$$Po_{el} = \frac{F_{in}}{\eta_{el}} \frac{C_P T_{in}^G}{\eta_{ise}} \left[\left(\frac{P_{out}^G}{P_{in}^G} \right)^{\frac{\kappa - 1}{\kappa}} - 1 \right] \tag{5.7}$$

5.3.3 Gas heat exchanger

This unit was used to change the temperature of a gas stream and to evaluate the heat duty of this equipment. The same approach was used for heating or cooling. It was supposed that no phase change occurs in this unit, thus the mass balance is easily carried out, as the inlet is equal to the outlet (Figure 5.5). The heat intake or removed was calculated with an energy balance (Eq. 5.8).

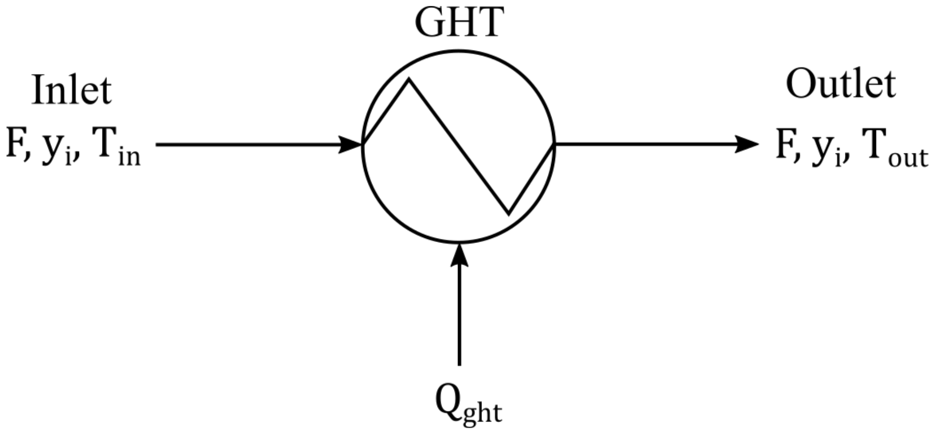

Figure 5.5: Scheme of a gas heat exchanger.

$$Q_{ght} = F_{out}^G \sum_i y_{out,i} \tilde{H}_i^G (T_{out}) - F_{in} \sum_i y_{in,i} \tilde{H}_i^L (T_{in}) \tag{5.8}$$

5.3.4 Chiller

This unit was also used to change the temperature of a gas stream. However, in this case, it was supposed that part of the water in the feed would condensate and leave as condensate (Figure 5.5). As hypothesis, it was assumed that the gas would leave the chiller saturated in water vapor at T_{out} (Eq. 5.9). The exiting flow rates were found applying a mass balance and the heat removed with an energy balance (Eqs. 5.10-5.12). Enthalpies were calculated as a function of temperature according to Perry and Green [96], with the standard state as reference (298.15 K). The electricity power required was obtained analogously to the BGC (Eq. 5.4).

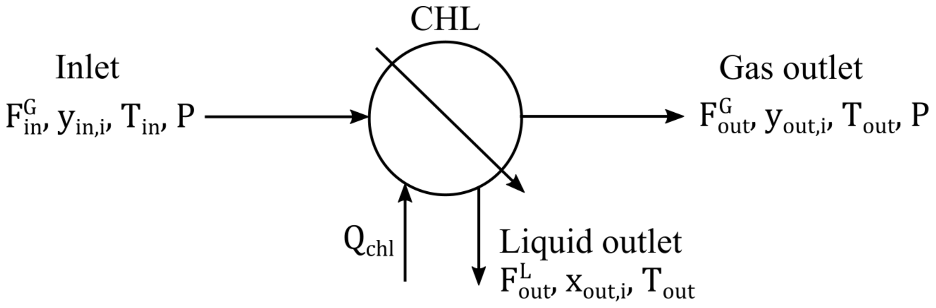

Figure 5.6: Scheme of a chiller.

$$y_{out,H_2O} = \frac{P_{sat,H_2O}\left(T_{out}\right)}{P} \tag{5.9}$$

$$F^G_{out} y_{out,i} = \begin{cases} F^G_{in} y_{in,i},\ i \neq H_2O \\ \frac{y_{out,H_2O}}{1-y_{out,H_2O}} \sum_{\iota \neq H_2O} F_{out} y_{out,\iota},\ i = H_2O \end{cases} \tag{5.10}$$

$$F^L_{out} = F^G_{in} y_{in,H_2O} - F^G_{out} y_{out,H_2O} \tag{5.11}$$

$$Q_{chl} = F^G_{out} \sum_i y_{out,i} \tilde{H}^G_i \left(T_{out}\right) + F^L_{out} \tilde{H}^L_{H_2O} - F_{in} \sum_i y_{in,i} \tilde{H}^G_i \left(T_{in}\right) \tag{5.12}$$

5.3.5 Membrane

The upgrading unit adopted in the biomethane plant was a three-stage membrane separator. The structure considered was based in the work of Kube [29], which consisted in, besides the three permeators, three heat exchanger at the feed of each separator and a compressor before the first one. The separation process was modeled using a simplified approach for a counter-current permeator as described below [125].

One-stage model

The separation process in one membrane stage was modeled using a simple approach for hollow fiber membranes proposed by Pettersen and Lien [125] (Figure 5.7), which is based in an analogy with heat exchange. In fact, this method was intended to initialize a more complex model. However, due to its numerical simplicity, it was employed here to describe the biogas upgrading unit.

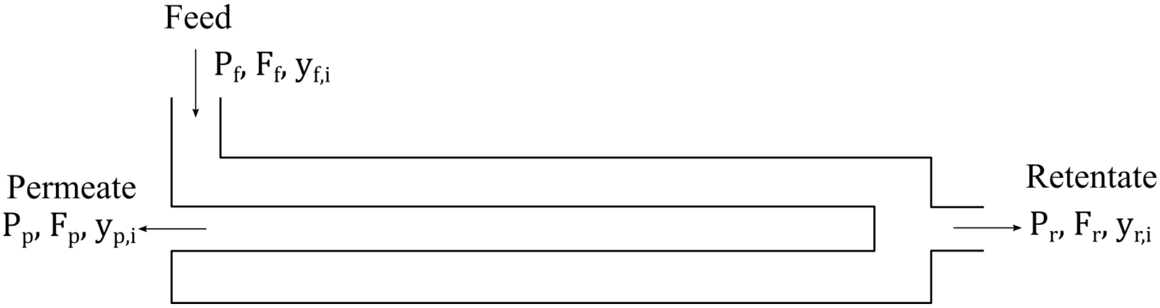

Figure 5.7: Scheme of a membrane permeator. Adapted from Pettersen and Lien [125].

In this unit, the cut-ratio, o, is defined as the ratio of the flow rate of the permeate and the feed (Eq. 5.13), and δ the trans-membrane pressure ratio (Eq. 5.14. It was supposed no heat effect or pressure drop in either side of the membrane. Besides, for each compound, the dimensionless permeation factor, r_i, was calculated as a function of the feed pressure and flow rate, and membrane's area and permeability (Eq. 5.15).

$$o = \frac{F_p}{F_f} \tag{5.13}$$

$$\delta = \frac{P_p}{P_f} = \frac{P_p}{P_r} \tag{5.14}$$

$$r_i = \frac{AP_f\Xi_i}{F_f} \tag{5.15}$$

From the analogy with heat transfer and an approximation of the logarithmic mean , the composition of the permeate stream can be calculated (Eqs. 5.16-5.19) [125]. In this approach, o is the only variable that needs to be found by the numerical solver. The equation that needs to be solved is the summation of the permeate's composition (Eq. 5.20). The pressures, membrane properties and feed properties are parameters that should be known beforehand.

$$y_{p,i} = \frac{-BB_i + \sqrt{BB_i^2 - 4AA_i CC_i}}{2AA_i} \tag{5.16}$$

$$AA_i = \frac{\delta}{3}\left(\frac{2o}{r_i} - \delta\right) + \frac{o}{3\,(1-o)}\left(\frac{o}{r_i} + \frac{o}{12\,(1-o)} - \delta\right) + \left(\frac{o}{r_i}\right)^2 \tag{5.17}$$

$$BB_i = \frac{y_{f,i}}{3}\left(1 + \frac{1}{1-o}\right)\left(\delta - \frac{o}{r_i}\right) + \frac{o y_{f,i}}{18\,(1-o)}\left(7 - \frac{1}{1-o}\right) \tag{5.18}$$

$$CC_i = \left(\frac{y_{f,i}}{6\,(1-o)}\right)^2 \left(o^2 + 12o - 12\right) \tag{5.19}$$

$$\sum_i y_{p,i}\,(o) = 1 \tag{5.20}$$

An alternative format for Eq. 5.16 was obtained by extracting the feed composition from BB_i and CC_i (Eq. 5.21), which will be employed in the three-stage model.

$$y_{p,i} = y_{f,i} \frac{\frac{-BB_i}{y_{f,i}} + \sqrt{\frac{BB_i^2}{y_{f,i}^2} - 4AA_i \frac{CC_i}{y_{f,i}^2}}}{2AA_i} = y_{f,i} HH_i \tag{5.21}$$

Three-stage model

In biogas plants, three-stage permeators are more commonly used and the structure adopted by Kube [29] was used (Figure 5.8). In each membrane m, the permeate composition can be written as a function of its feed's molar fraction and $HH_{m,i}$ (Eq. 5.22). $HH_{m,i}$ is calculated using Eq. 5.21.

$$y_{j,i} = y_{k,i} HH_{m,i},\ (j,k,m) \in \left\{(6,\ 2,\ 1),\ (5,\ 3,\ 2),\ (8,\ 6,\ 3)\right\} \tag{5.22}$$

We propose here a simple model based on the three-stage scheme proposed by Kube [29], but each stage being modeled as proposed by Pettersen and Lien [125]. Hence, the permeate and retentate flow rates were estimated from o_m by applying a mass balance in each stage (Eqs. 5.23

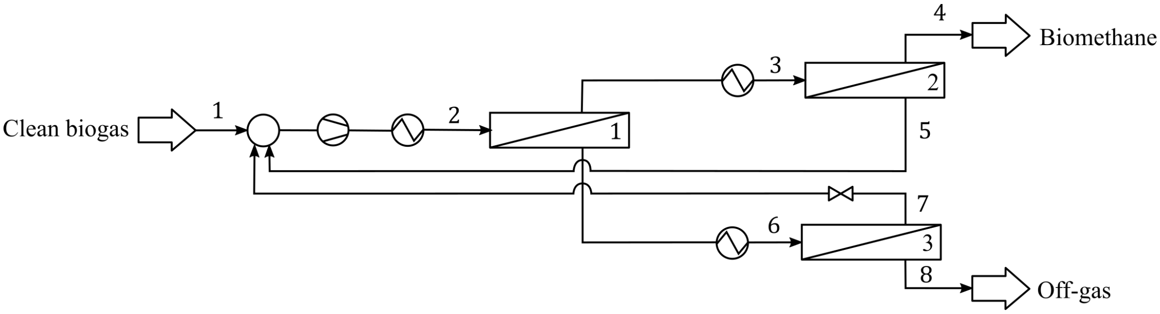

Figure 5.8: Scheme of a three-stage membrane permeator. The numbering refers to the stream and membrane stage identifications used in the separator model. Adapted from Kube [29].

and 5.24). Moreover, the retentate's composition was evaluated with a partial mass balance (Eq. 5.25).

$$F_j = F_k o_m,\ (j,k,m) \in \left\{(6,2,1),\ (5,\ 3,\ 2),\ (8,\ 6,\ 3)\right\} \tag{5.23}$$

$$F_j = F_k\left(1-o_m\right),\ (j,\ k,\ m) \in \left\{(3,\ 2,\ 1),\ (4,\ 3,\ 2),\ (7,\ 6,\ 3)\right\} \tag{5.24}$$

$$y_{j,i} = y_{k,i}\frac{1-o_m HH_{m,i}}{1-o_m},\ (j,k,m) \in \left\{(3,\ 2,\ 1),\ (4,\ 3,\ 2),\ (7,\ 6,\ 3)\right\} \tag{5.25}$$

In this system, the stream 1 correspond to the inlet of the upgrading unit. All properties of this stream are known and provided to the membrane model (F_1, $y_{1,i}$, P_1, T_1). The stream 2's flow rate and composition was estimated by substituting the total and partial mass balances in each membrane (Eqs 5.26 and 5.27), which allowed determining the other streams (Eqs. 5.23-5.25) . Therefore, the three-stage permeator model corresponds to three algebraic equations that need to be solved by the numerical solver (Eqs 5.28-5.30) as a function of the cut-ratio of each membrane (o_1, o_2 and o_3).

$$F_2 = \frac{F_1}{1-o_1\left(1-o_3\right)-o_2\left(1-o_1\right)} \tag{5.26}$$

$$y_{2,i} = \frac{F_1 y_{1,i}}{F_2 - F_5\left(\frac{1-o_1 HH_{1,i}}{1-o_1}\right) - F_6\left(\frac{1-o_3 HH_{3,i}}{1-o_3}\right)} \tag{5.27}$$

$$1 = \sum_i y_{6,i}(o_1,\ o_2,\ o_3) \tag{5.28}$$

$$1 = \sum_i y_{5,i}(o_1,\ o_2,\ o_3) \tag{5.29}$$

$$1 = \sum_i y_{8,i}(o_1,\ o_2,\ o_3) \tag{5.30}$$

In the work of Kube [29], the capacities (i.e. product of permeability and active membrane area, $A\Xi_i$ in Eq. 5.15) of CH_4 and CO_2 of one membrane module were provided. Each module consisted of a polyamide membrane of 0.11 m diameter and 1.2 m length [29]. The dependence of capacities were described using an Arrhenius equation (Eq. 5.31). The parameters used in this relationship were estimated from the selectivities provided in Kube's paper (CH_4 and CO_2) or estimated from his simulation results (O_2 and N_2) (Table 5.2). O_2 and N_2 were only used in the comparison between the simple model described here with the Kube's results. To account the number of modules in each stage (N_m), this parameter was added to the permeation factor estimation for each stage m (Eq. 5.32)

$$A\Xi_i = A_{0i}^{mem} exp\left(-\frac{E_{ai}}{RT}\right) \tag{5.31}$$

$$r_{m,i} = \frac{P_{fm} A\Xi_i(T_m) N_m}{F_{fm}} \tag{5.32}$$

Table 5.2: Membrane capacity estimation parameters

Compound	A_{Oi} [mol s^{-1} Pa^{-1}]	E_{ai} [J mol^{-1}]
CH_4	5.32 10^{-5}	19155
CO_2	1.23 10^{-5}	5842
N_2	3.25 10^{-8}	832
O_2	4.07 10^{-5}	14004

The compressor in this unit was modeled according to Section 5.3.2. Thus, according to the working pressure of the first membrane, the electricity consumption could be estimated. Moreover, the heat exchanger before each stage was considered as described in Section 5.3.3 and their electric power requirement was estimated accordingly.

In addition, Kube's results were also used to evaluate the simple membrane model described before. In fact, he developed a 1-D model for each stage, which is much more complex compared to the approach here. The membrane specifications used correspond to the standard experiment described in his paper [29] (Table 5.3). As notation, the Kube's model is labeled as "Kube", while the one based on the work of Pettersen and Lien [125] developed here is notated as "3-MEM".

Table 5.3: Membrane unit specifications used in model comparison [29]

Stage	N_m	P_f [bar]	P_p [bar]	T [K]
1	32.9	18.3	3.41	283.15
2	23.8	18.3	1.00	310.15
3	34.3	3.41	1.00	333.15

Comparing these two approaches, the results obtained with the 3-MEM were close to the ones from Kube (Table 5.4). Indeed, the relative difference in flow rate in the biomethane stream (i.e. stream 4) was at 3.6%, and of 3.2% in CH_4 composition. The lean gas stream (i.e. stream 8) the differences in flow rate and CO_2 were of 3.7% and 0.5% respectively. These two streams are the most important ones of this system, as they are those that cross the boundaries of the membrane model. Therefore, the 3-MEM model, despite of its simple approach, yields similar results to a much more complex model. However, to reach the equivalent biomethane composition as in Kube's work, some adjustments in the operational parameters would be required. Nevertheless, it still could be an useful tool in evaluating the effects of temperature, pressure ratios, or number of modules in each stage in such kind of permeator.

Table 5.4: Three-stage membrane simulation results for the comparison test

Stream	Source	F [mol s^{-1}]	Composition [%]			
			CH_4	CO_2	N_2	O_2
1	Kube	20.18	50.0	49.2	0.3	0.5
	3-MEM	20.18	50.0	49.2	0.3	0.5
2	Kube	25.03	47.3	51.6	0.3	0.8
	3-MEM	26.26	44.5	54.5	0.3	0.7
3	Kube	14.22	79.1	19.5	0.5	0.9
	3-MEM	14.92	74.8	23.9	0.4	0.9
4	Kube	10.25	97.4	1.5	0.6	0.5
	3-MEM	10.62	94.3	4.4	0.6	0.7
5	Kube	3.97	31.9	66.0	0.3	1.9
	3-MEM	4.29	26.5	72.0	0.1	1.4
6	Kube	10.81	5.5	93.8	0.1	0.7
	3-MEM	11.34	4.7	94.8	0.04	0.4
7	Kube	0.89	55.8	41.1	0.5	2.5
	3-MEM	1.79	25.9	72.5	0.2	1.4
8	Kube	9.92	1.0	98.5	0.0	0.5
	3-MEM	9.55	0.8	99.0	0.0	0.2

5.3.6 Methanation reactor

The technology employed in the methanation reactor was a multi-tubular fixed bed reactor (Figure 5.9). This equipment consists in several tubes packed with catalyst particles inside a larger shell. While the reactants flow through the tubes, a heat exchange fluid is used in the shell side to control the reactor temperature. In terms of modeling, a 1-D model developed in a previous PhD thesis carried out in LaTEP was used [126]. Although a full description of this model can be found in the manuscript of Fache [126] (Chapter 2), a brief description of the main aspects of this model is described here for practicality.

In the reactor, three equilibrium reactions were considered: CO and CO_2 methanation (Eqs. 5.33 and 5.34 respectively), and water-gas-shift reaction (Eq. 5.35) [127]. The kinetics employed were those of the work of Xu and Froment [127].

$$CO + 3H_2 \rightleftharpoons CH_4 + H_2O,\ \Delta\tilde{H}_R^{\circ} = -206\,kJ\,mol^{-1} \tag{5.33}$$

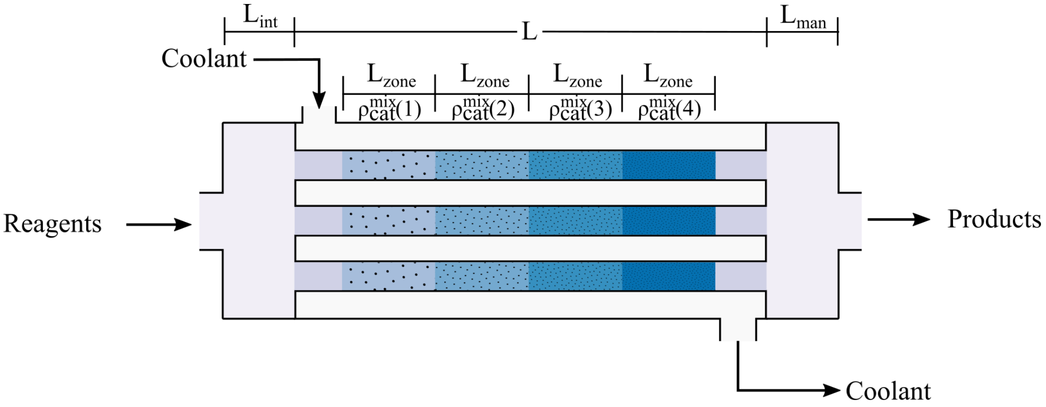

Figure 5.9: Multi-tubular fixed bed reactor with four catalyst dilution zones.

$$CO_2 + 4H_2 \rightleftharpoons CH_4 + 2H_2O,\ \Delta\tilde{H}_R^\circ = -165\ kJ\ mol^{-1} \tag{5.34}$$

$$CO + H_2O \rightleftharpoons CO_2 + H_2,\ \Delta\tilde{H}_R^\circ = -41\ kJ\ mol^{-1} \tag{5.35}$$

In the reactor tubes, a length L_{reac} is filled with a mixture of catalyst and inert pellets, while only glass particles are used in the suction and discharge zones. The catalyst filled zones can either have an uniform catalyst density or different values in each zone (e.g. $\rho_{cat}^{mix}\ (1)$, $\rho_{cat}^{mix}\ (2)$, etc). The heat-transfer fluid can flow co or counter-current. Plug-flow were supposed for both the gas and the heat-transfer fluid. In the gas phase, mass (Eq. 5.36), moment (Eq. 5.37) and energy (Eq. 5.38) conservation equations were applied. Energy balances were also applied to the tube (Eq. 5.39), and to the heat exchange fluid (Eq. 5.40). For simplicity the notation used by Fache [126] was conserved in these equations, therefore a table with the nomenclature used in this part is given (Table 5.5).

$$\epsilon_{tot}\frac{\partial \rho_i}{\partial t} = M_i \sum_j \nu_{i,j} r_j^v - \frac{1}{S_{reac}}\frac{\partial\left(\rho_i Q_v\right)}{\partial z} \tag{5.36}$$

$$-\frac{\partial P}{\partial z} = 150\frac{(1-\epsilon)^2}{\epsilon^3}\frac{\mu}{d_p^2}\frac{Q_v}{S_{reac}} + 1.75\frac{1-\epsilon}{\epsilon}\frac{\rho_{gas}}{d_p}\left(\frac{Q_v}{S_{reac}}\right)^2 \tag{5.37}$$

$$\frac{\partial\left(\rho_{por}C_{por}T+\epsilon_{tot}\sum_i\rho_i u_i\right)}{\partial t}=\frac{\partial}{\partial z}\left(\lambda_{ea}\frac{\partial T}{\partial z}\right)-\frac{1}{S_{reac}}\frac{\partial}{\partial z}\left(\sum_i Q_m(i)h_i\right)+2\frac{\phi_{t-gs}}{R_{reac}} \tag{5.38}$$

$$(\rho C)_{metal}\frac{\partial T_{tube}}{\partial t}=\frac{2\pi\left(R_{tube}\phi_{c-t}-R_{reac}\phi_{t-gs}\right)}{S_{metal}}+\lambda_{metal}\frac{\partial^2 T_{tube}}{\partial z^2} \tag{5.39}$$

$$\begin{aligned}(\rho C)_{cool}\frac{\partial T_{cool}}{\partial t}=&\lambda_{cool}\frac{\partial^2 T_{cool}}{\partial z^2}-(\rho C)_{cool}\frac{Q_{cool}}{S_{cool}}\frac{\partial T_{cool}}{\partial z}\\&-\frac{2\pi\left(R_{tube}n_t\phi_{c-t}+R_{ext}\phi_{loss-cool}\right)}{S_{cool}}\end{aligned} \tag{5.40}$$

Table 5.5: Methanation model notation

Variable	Meaning	Unit
C	Mass thermal capacity	$J\ K^{-1}\ kg^{-1}$
C_{por}	Mass thermal capacity of the porous medium	$J\ K^{-1}\ kg^{-1}$
d_p	Particle diameter	m
h_i	Partial enthalpy of compound i	$J\ kg^{-1}$
M_i	Molar mass of compound i	$kg\ mol^{-1}$
n_t	Number of tubes	
P	Total pressure	Pa
Q_{cool}	Volumetric flow rate of the coolant	$m^3\ s^{-1}$
Q_m	Mass flow rate	$kg\ s^{-1}$
Q_v	Volume flow	$m^3\ s^{-1}$
r_j^v	Rate of reaction j per apparent volume	$mol\ s^{-1}\ m_{total}^{-3}$
R_{ext}	Exterior radius of the reactor shell	m
R_{reac}	Tube internal radius	m
R_{tube}	External tube radius	m

Continued on next page

Table 5.5 – *Continued from previous page*

Variable	Meaning	Unit
S_{metal}	Surface of tube wall	m^2
S_{cool}	Surface of the flow area of the coolant	m^2
S_{reac}	Apparent section surface of the reaction medium	m^2
t	Time	s
T	Temperature	K
T_{cat}	Catalyst temperature	K
T_{cool}	Coolant temperature	K
T_{gas}	Temperature of the gas phase	K
T_{tube}	Tube wall temperature	K
u_i	Internal energy of compound i	$J\ kg^{-1}$
z	Axial position	m
Greek letters		
ϵ	Macroscopic void fraction	
ϵ_{mic}	Microscopic particle void fraction	
ϵ_{total}	Total particle void fraction, i.e. $\epsilon + (1 - \epsilon)\epsilon_{mic}$	
λ_{cool}	Thermal conductivity of the coolant	$W\ m^{-1}\ K^{-1}$
λ_{ea}	Thermal conductivity in the axial direction	$W\ m^{-1}\ K^{-1}$
λ_{metal}	Thermal conductivity of tubes and the reactor shell	$W\ m^{-1}\ K^{-1}$
μ	Dynamic viscosity	$Pa\ s$
ρ	Mass density	$kg\ m^{-3}$
ρ_i	Mass concentration of compound i	$kg\ m^{-3}$
ρ_{gas}	Gas mass concentration	$kg\ m^{-3}$
ρ_{por}	Apparent mass density of the porous solid	$kg\ m^{-3}$
$\nu_{i,j}$	Stoichiometric coefficient of compound i in reaction j	
ϕ_{c-t}	Heat flow from the coolant to the tube	$W\ m^{-2}$
$\phi_{loss-cool}$	Heat flow from the coolant to the external environment	$W\ m^{-2}$

Continued on next page

Table 5.5 – *Continued from previous page*

Variable	Meaning	Unit
ϕ_{t-gs}	Heat flow from the tube to the reaction medium (gas + solids)	$W\ m^{-2}$

CHAPTER 6

BIOMETHANE AND P2G SIMULATIONS

With the biogas digester, methanation reactor and auxiliary units modeled, some study cases were developed to illustrate different application possibilities of such work.

6.1 Biomethane system

The structure of the biomethane plant was adopted equal as the reference one of Section 5.1 (Figure 5.1). The model blocks developed in Chapter 5 were employed as shown in Figure 6.1 to best represent the material and energy flows inside the plant. Thus, a BGC was used to account both the water condensation and impurities removal, and CMP1 was added to account the energy consumption of the compressor before the activated carbon column.

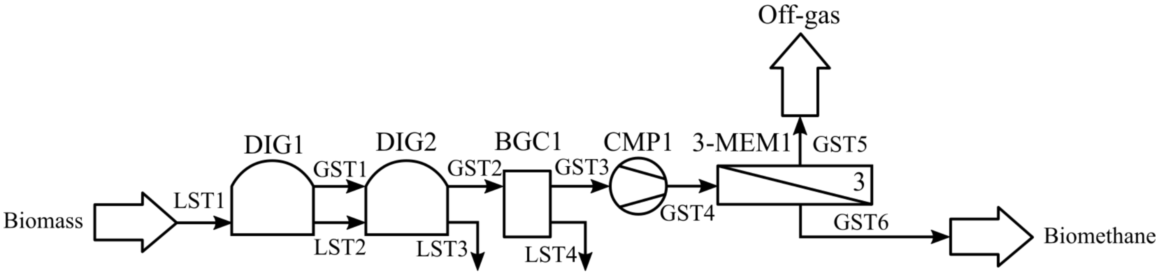

Figure 6.1: Model blocks to simulate a biomethane plant

The specifications used for the digester (DIG1) and post-digester (DIG2) were the same as the ones used in Section 4.7.2, which corresponds to the Biometharn Biogas plant (Aiguefonde, France), except for the dimensions of the double-membrane gasholders, which storage capacities were increased. The specifications of each unit are detailed in Table 6.1. Unless otherwise specified, the meteorological data used were obtained from Solcast at the location of the Biometharn biogas plant (+ 43.513, + 2.332) for the year of 2021 [122].

Table 6.1: Unit specifications in the biomethane plant

Block	Specification	Value	Unit
DIG1	Outer cover height (HT_{TOP1})	8.3	m
	Max inner cover height ($HT_{TOP2,max}$)	7.0	m
DIG2	Outer cover height (HT_{TOP1})	6.0	m
	Max inner cover height ($HT_{TOP2,max}$)	5.1	m
GST1	Pipe inner diameter (ID_{pipe})	0.15	m
	Pipe length (L_{pipe})	8.0	m
	Pipe roughness (ϵ_{pipe})	0.0	m
	Frictional losses ($\sum \zeta$)	1.5	
BGC1	Outlet temperature (T_{out})	277.15	K
CMP1	Discharge pressure (P_{out})	1.18	bar
	Isentropic efficiency (η_{ise})	0.8	
	Electric efficiency (η_{el})	0.9	
3-MEM1	Compressor		
	Isentropic efficiency (η_{ise})	0.8	
	Electric efficiency (η_{el})	0.9	
	Stage 1		
	Temperature (T_1)	278.15	K
	Feed pressure (P_{f1})	20	bar
	Permeate pressure (P_{p1})	3.41	bar
	Number of modules (N_1)	24	
	Stage 2		
	Temperature (T_2)	278.15	K
	Feed pressure (P_{f2})	20	bar
	Permeate pressure (P_{p2})	1	bar
	Number of modules (N_2)	26	
	Stage 3		
	Temperature (T_3)	278.15	K
	Feed pressure (P_{f3})	3.41	bar
3-MEM1	Permeate pressure (P_{p3})	1	bar
	Number of modules (N_3)	16	

6.1.1 Variable location

As the digester model can evaluate heat losses as a function of its structure and meteorological data, one possible application is to use it to analyze the effect of installing a biogas plant at different locations. In this study case, the feed was kept constant at an OLR of 1.72 kg VS m^{-3} d^{-1} with the following mass composition: 87.4% carbohydrates, 11.5% proteins, 0.1% lipids, and 1.0% VFA. Besides, in this study case, only the biogas production system (i.e. DIG1 and DIG2) was evaluated.

The weather data corresponded to two different geographical zones: South West France (+ 43.300, - 0.403; SWFR) and North West United Kingdom (+ 55.775, - 4.165; NWUK), and they were collected using PVGIS for a TMY in each place [128].

Overall, the climate in NWUK is colder and it has lower solar irradiance (Figures 6.2 and 6.3). As a consequence, the calculated heat delivered by the heat exchanger was in average 25% higher in NWUK compared to SWFR (Figure 6.4). Considering that the biogas was employed in a boiler with a thermal efficiency of 82% [58], it would have required 55740 Nm^3 year^{-1} of CH_4 in SWFR, which corresponds to an auto-consumption of 6.9%, while in NWUK, it would have required 68342 Nm^3 year^{-1}, 8.5% of the total CH_4 produced.

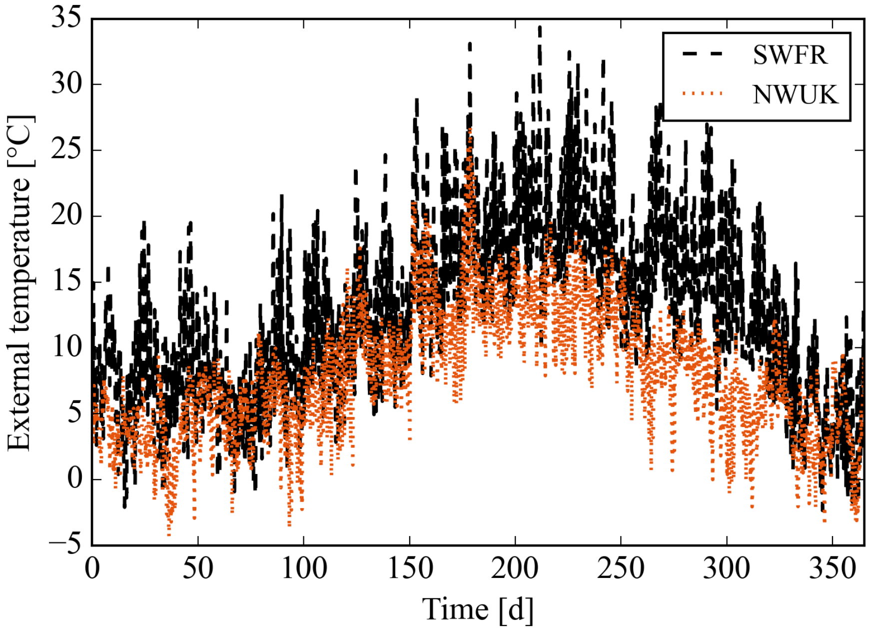

Figure 6.2: External temperature for a TMY in NWUK and in SWFR [128]

Therefore, mitigating the heat losses is of paramount importance to improve biogas plants energetic efficiency. To evaluate some strategies another simulation was carried out. In this scenario, named NWUK+, the digester structure was improved to mitigate heat losses to external environment. The wall insulant thickness was increased by 50%. Besides that, the properties of the internal biogas membrane cover were modified to account the use of an improved layer to reduce the heat losses through the roof. This technology (CUPOLA M3 HEAT SHIELD®) is composed by adding a

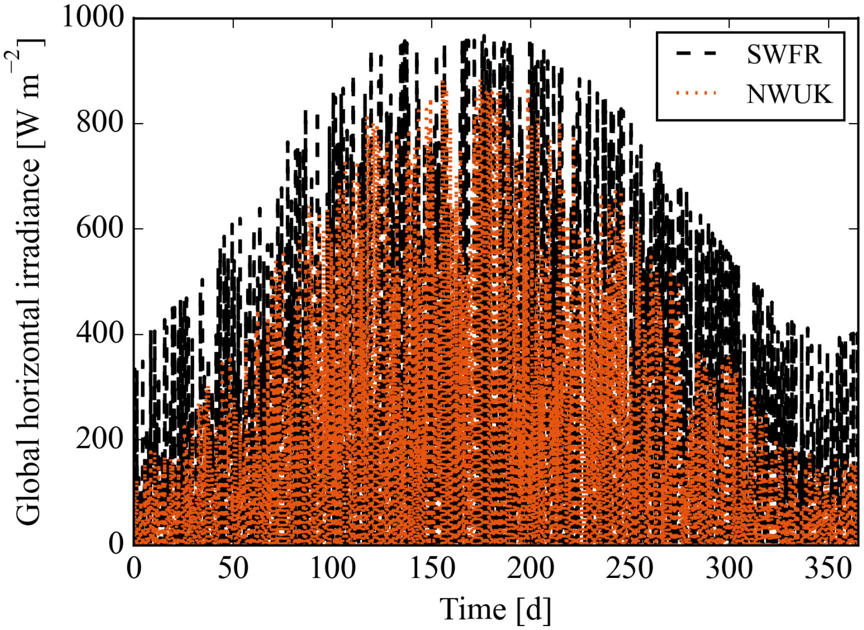

Figure 6.3: Global horizontal irradiance for a TMY in NWUK and in SWFR [128]

supplementary layer of a triple-layered ultra-shielded material with a reflexive layer on its top over the internal cover (TOP2) [129]. The thermal properties of the internal membrane were estimated using a weighted average considering that the additional layer had properties similar to a polymeric insulant [93]. Besides that, the emissivity of the upper part of this cover was set at 0.05 [93, 129].

Regarding the digester structure, the cover was the main heat sink, accounting for over 60% of heat losses (Figure 6.5). Due to the weather difference, the energy lost to the external environment in NWUK was 51% and 19% higher compared to SWFR during summer and winter time respectively. Improving the thermal insulation structure successfully managed to hinder the heat losses. In summer, there was a reduction of 37% in NWUK+ compared to NWUK, reaching values close to SWFR losses. Besides that, the improved structure results reached lower values compared to SWFR and the additional layer in the internal cover membrane lead to a decrease of around 45% of heat losses through the cover, which is close to the reported value of 50% for such kind of technology [129].

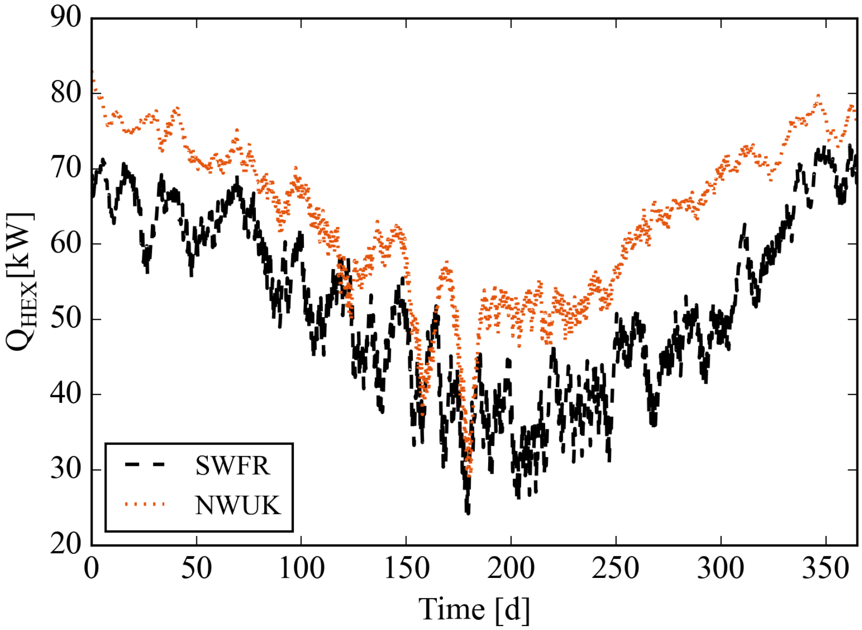

Figure 6.4: Heat delivered by the digester's heat exchanger.

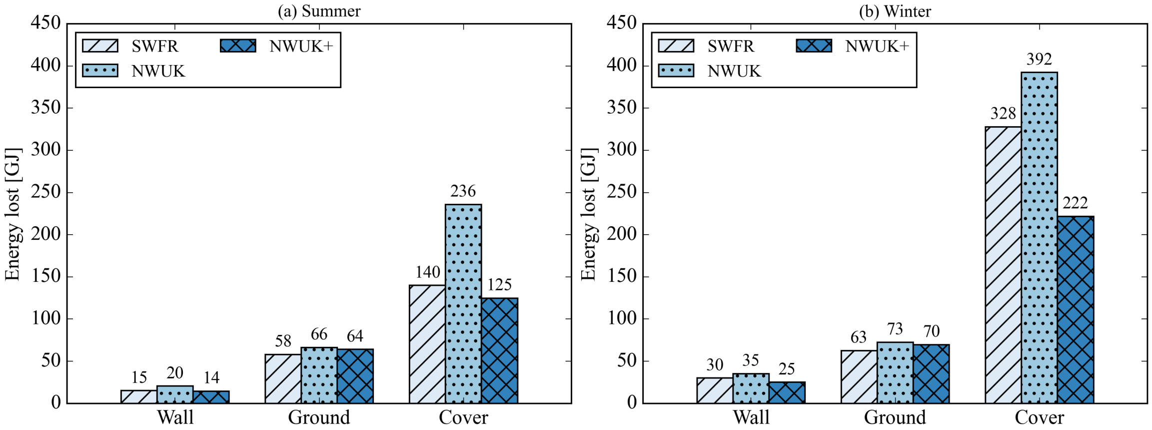

Figure 6.5: Total energy lost through the digester structure in summer(a) and in winter (b).

6.1.2 Gas storage management

In many agricultural biogas plants, digesters operate at a semi-batch regime, with biomass being injected periodically [130]. Compared to a continuous operation, this regime leads to intraday periodic variations of the biogas production. In terms of simulation, if the gas outlet flow rate is calculated using a P-control on the gas level (as described in Section 4.5), the variability in biogas production would be directly transferred to the outlet. However, in real systems, part of this effect would be buffered by the gas storage. Therefore, this study case analyzed the double-membrane gasholder model with different alternatives for calculating this flow rate.

To better represent the actual operation of an agricultural biogas plant, a periodic biomass feed was applied. The feed composition was based on the feedstock used in *Cooperativa Speranza* (Table 3.1) and the amount was scaled according to the digester's dimensions (Figure 6.6). The biomass feed policy corresponded to injecting the biomass twice a day at 8:00 and at 18:00 for a duration of 2 h and a ramp of 5 min (Figure 6.7).

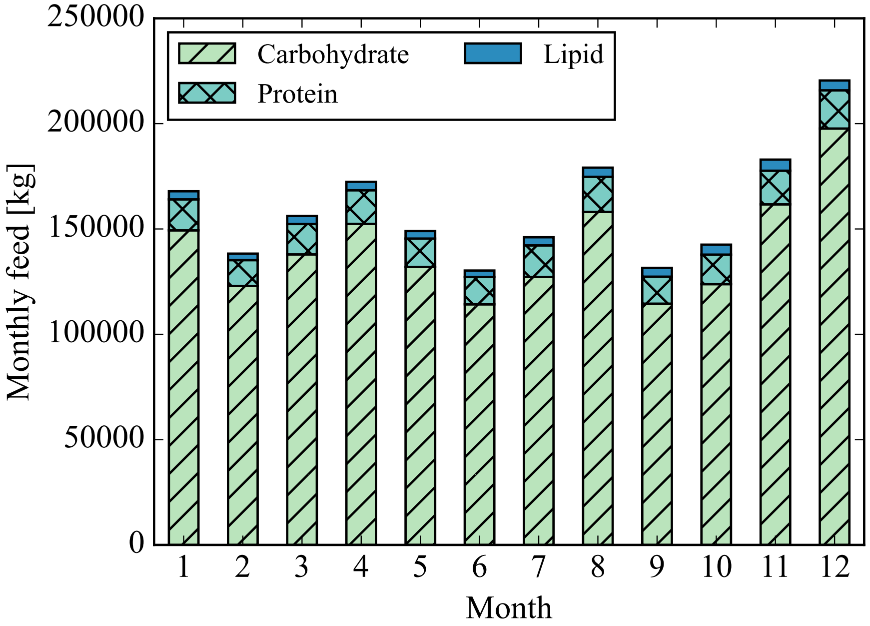

Figure 6.6: Monthly digester feed amount and composition used in simulations.

A stable gas outlet flow rate (GST2 in Figure 6.1) was found by solving an optimization problem. In this case, the biogas level was represented with a simplified approach (Eq. 6.1) and the

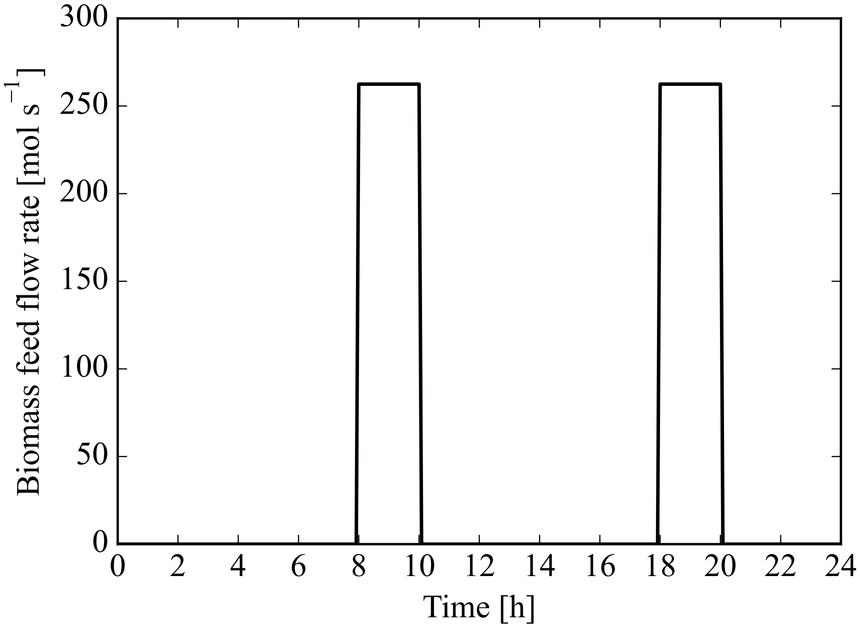

Figure 6.7: Daily digester periodic feed. The values used correspond to January.

time period was discretized in N equal intervals Δt. The temperature was supposed to vary, but the pressure was assumed constant. Indeed, although the real pressure in the gasholder is variable, it is still close to the atmospheric value. In Eq. 6.1, the inlet flow rate, $F_{in,k}$, corresponds to the biogas production. The objective function was to minimize the square difference between the outlet flow rate and the average value for the whole period (Eq 6.2). Therefore, this optimization problem consisted of N variables and $2N$ constraints.

$$LVL_k^G = LVL_{k-1}^G + \frac{RT_k^G}{V_{max}^G P} F_{in,k}^G \Delta t - \frac{RT_k^G}{V_{max}^G P} F_{out,k}^G \Delta t, \forall k \in [1,\ N] \tag{6.1}$$

$$\min_{F_{out,k}\ \forall k \in [1,N]} \sum_k \left(F_{out,k} - \overline{F_{out}} \right)^2 \tag{6.2}$$

$$s.t.\ LVL_k^G \geq LVL_{min}^G,\ \forall k \in [1,\ N-1]$$

$$LVL_k^G \geq LVL_{min,last}^G,\ k = N$$

$$LVL_k^G \leq LVL_{max}^G,\ \forall k \in [1,\ N]$$

The parameters used in Eqs. 6.1 and 6.2 were obtained from the simulation results of the digester model. Temperature values at each time t_k were taken as the average values of the two gasholders, and the biogas production, $F_{in,k}$, were considered equal as the flow rate of the stream GST2 calculated with a fixed set value on the gas level (Eq. 4.160). As the gas level in both gas storages are kept numerically close (Section 4.4.1, Eq. 4.158), V^G_{max}, was adopted as the sum of maximal capacities of the two gasholders, which in this case was 3026 m^2. Maximal and minimal gas filling levels were imposed at 85% and 30% respectively, except for the last time point, which minimum value was set at 50%. The time step of 1 h was used. After the optimization calculations, the digesters were simulated again with the optimization results attributed to GST2. A summary of this procedure is presented in Figure 6.8. As notation, the simulations where GST2's flow rate was calculated using a P-control were labeled as STD, while the ones that used the optimization results were labeled as STB.

The solution of Eq. 6.2 was obtained using the solver Algencan, which is a Fortran software for general nonlinear programming based on the augmented lagrangian method [131]. The problem explored in this work was a simple one, but the method employed could be replicated for another situations. For example, in case of dynamic electricity production, to schedule biogas production in order to maximize the plant revenues [132].

The simulations during the month of January showed that this methodology successfully reduced the variation amplitude of biogas production (Figure 6.9). The flow rate was kept stable at around 353 $Nm^{-3}h^{-1}$, while the gas storage level varied from 0.73 until 0.82.

In a second situation, the feed was interrupted for one day at day 14. This situation was employed to evaluate the use of the gas storage to compensate for a relevant drop in biogas production. Indeed, the gas storage managed to buffer this effect, as the GST2 flow rate dropped by 9.4% in STB, compared to a reduction of around 20% in STD (Figure 6.10). Although the reduction in production occurred already in day 14, the recovery of the reactor took place at a slower pace, reaching 99% of the initial average value after 15 days. However, it should also be noted that the kinetic model has a tendency to predict faster variations due to feed changes than the reality, as it was observed in the kinetic validation (Section 4.7.1).

Regarding the gas level in STB, there is a discharging period from day 15 to day 17 and a

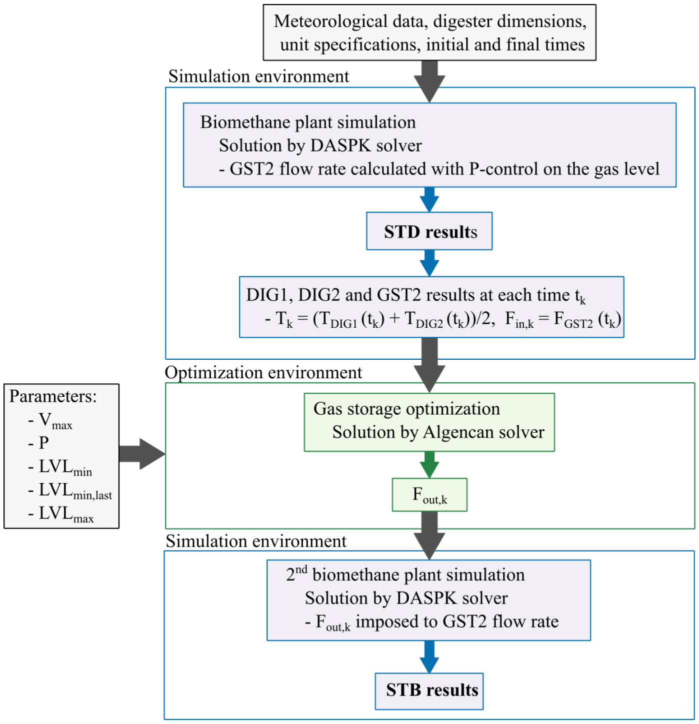

Figure 6.8: Scheme of the simulation procedure to obtain STD and STB results.

charging one from day 26 onward. In a double-membrane gasholder, a decrease in its level is accompanied by a pressure reduction [110, 112]. On the other hand, a pressure increase occurs when the level augment. This effect could also be observed in the headspace of the digesters (Figure 6.11). The average pressure in DIG1 when the gas level was stable at around 0.8 was 4.88 $mbar_g$. It decreased to 4.78 $mbar_g$ during the discharge phase, and then augmented to 4.92 $mbar_g$ during the charge phase. These changes were relatively small because of the slow variation of the stored gas volume, which occurred during a time span of several hours in each phase. The pressure in DIG2 was slightly inferior to the one in DIG1 because the flow rate between them was calculated using a tube model (Section 4.4.1, Eq. 4.152). The biogas level in each digester was kept close to each other by varying the rotation speed of the air blower in DIG2, which was considered to be the secondary storage.

Indeed, having a model that represents the different variables that interplay in the operation of a double-membrane gasholder could be useful to training the staff of biogas plants. As discussed by Reinelt and Liebetrau [133], the misunderstanding of the double-membrane gasholder functioning by biogas plant operators has already led to wrong regulation of the gas storage, notably because

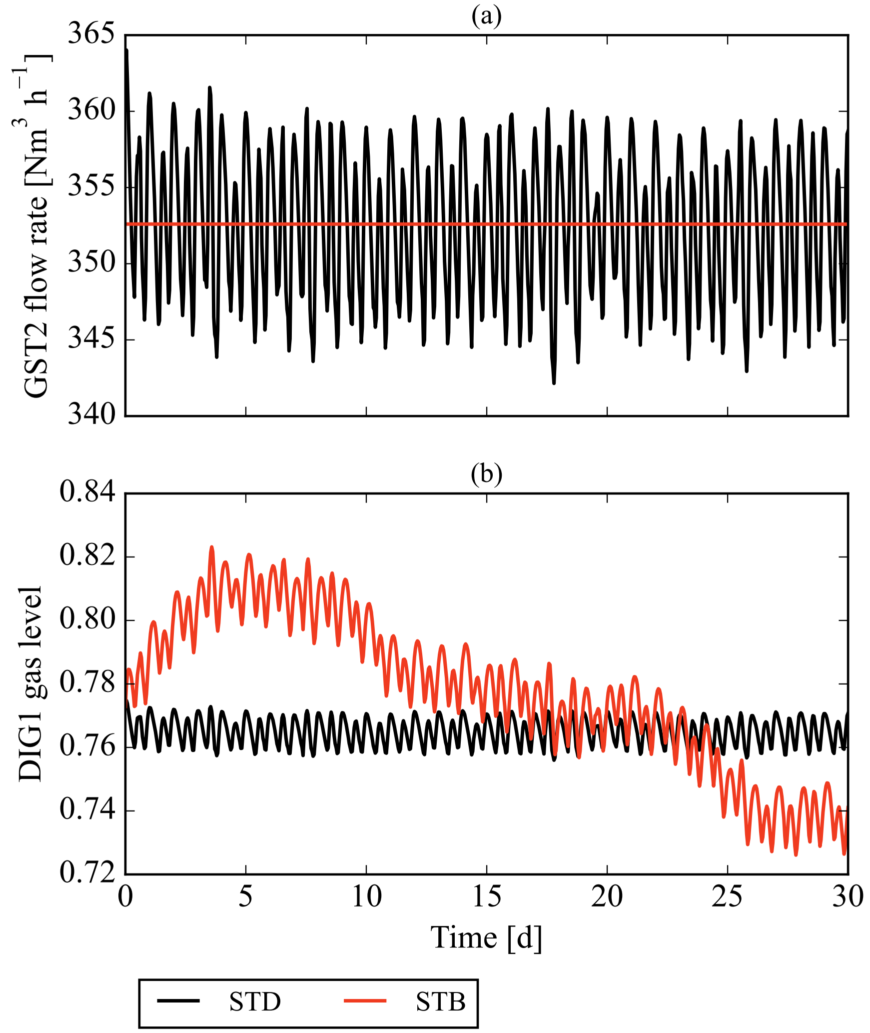

Figure 6.9: Results for different approach in GST2 flow rate calculation. (a) GST2 Flow rate, (b) DIG1 gas level.

the pressure is not directly correlated to the filling level in this kind of technology. Besides, this modeling approach can also be useful to evaluate the risk of overpressure event as a function of biogas temperature variations [110, 133, 134].

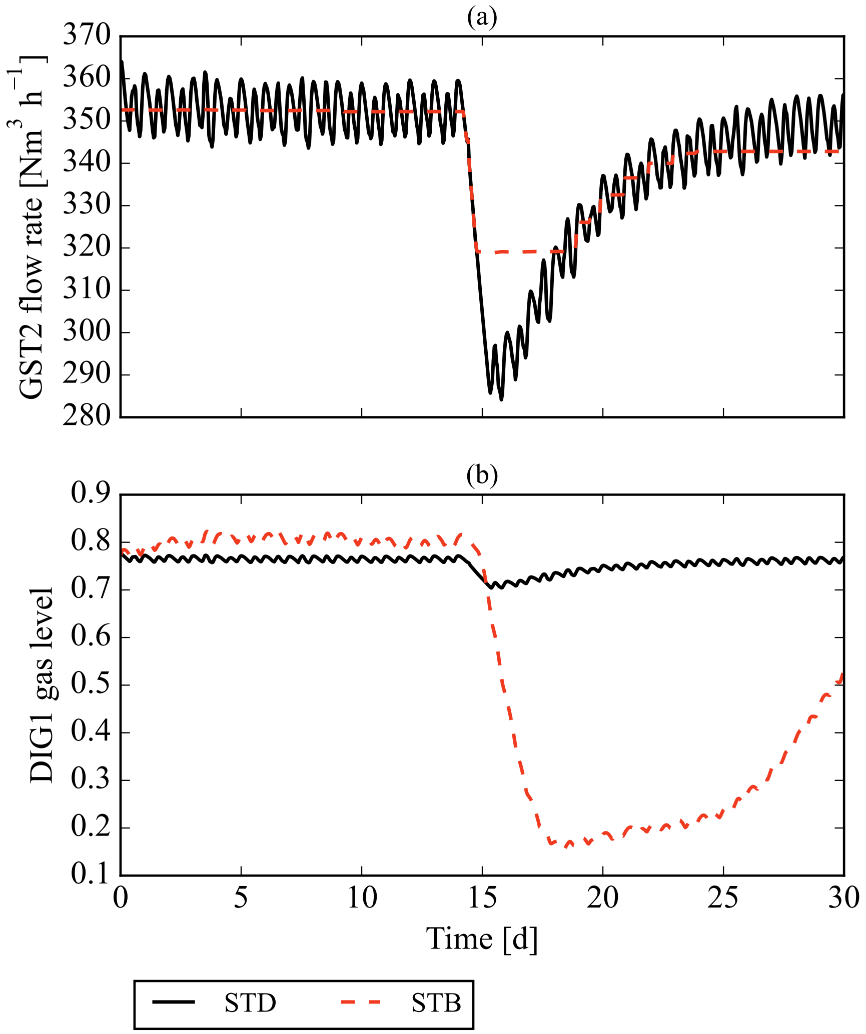

Figure 6.10: Results for different approach in GST2 flow rate calculation with a feed interruption at day 14: (a) GST2 Flow rate, (b) DIG1 gas level.

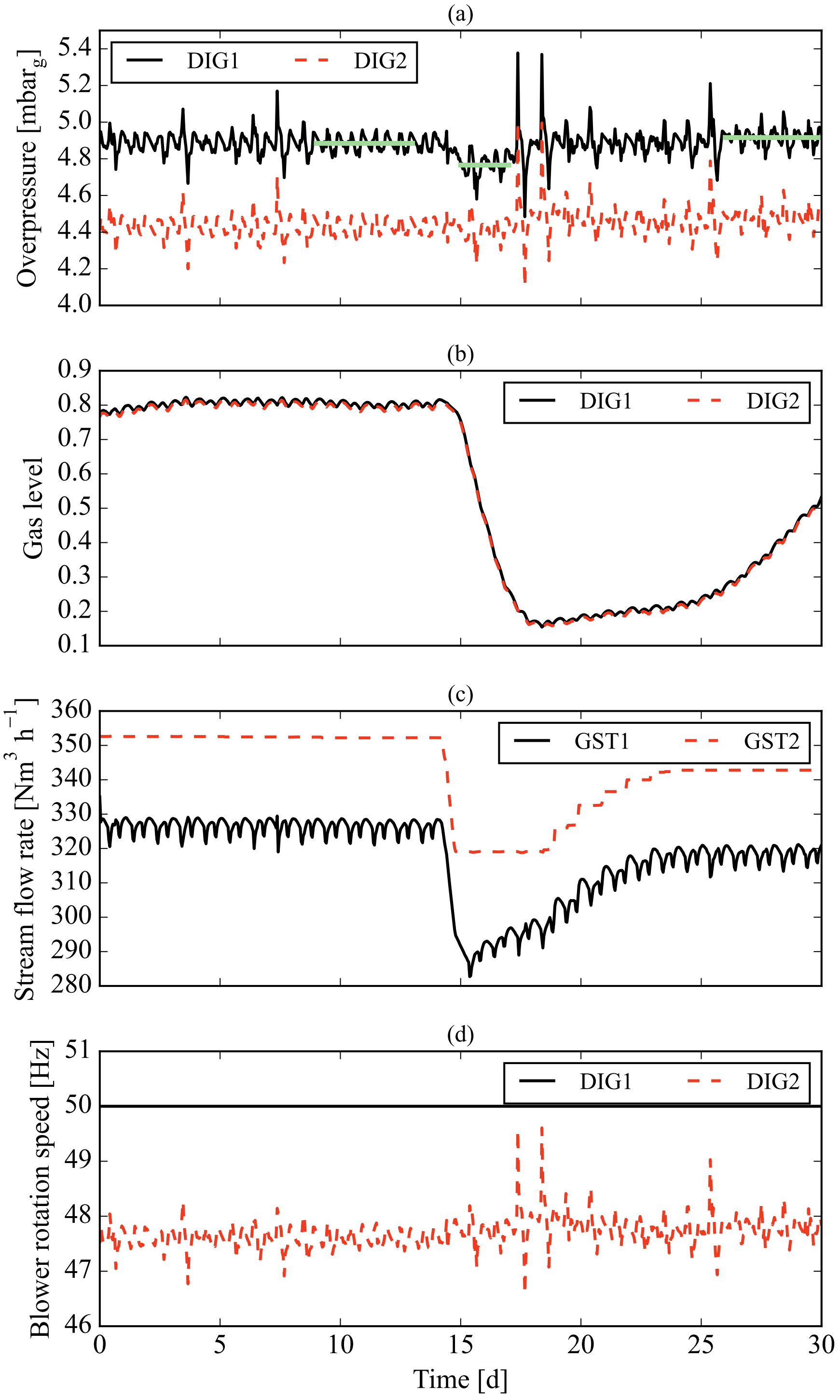

Figure 6.11: Gasholder variables in STB simulation: (a) overpressure in gasholder, (b) gas storage level, (c) stream flow rate, (d) air blower roation speed. In (a), the green lines indicate the average pressure of the period covered by them.

6.1.3 Biomethane production

The biomethane production was calculated considering the STB results of Section 6.1.2 and the system structure described in Section 6.1 (Figure 6.1). Here, two cases are described: January with feed interruption, and a simulation from 15 July to 14 August. The biomethane stream (GST6) should be composed of at least 97.5% of CH_4 [15], and the off-gas should ideally have less than 1.0% of CH_4 to avoid the need of additional treatment before releasing it to the atmosphere [29]. However, if GST5 is completely used in the P2G plant, this last restriction is not required.

In January, the biomethane managed to reach the required specifications (Figure 6.12), with a concentration of about 97.8% during the whole simulation period. The lower biogas flow rate from day 15 to 18 was accompanied by a slightly higher methane concentration, which increased from 53.4% to 55.9%. This, however, had little effect on the final product composition. Regarding the off-gas stream (GST5), CH_4 fraction exceeded the limit of 1.0% (Figure 6.13), with values around 1.2%. The biomass feed interruption, despite not impacting in a great deal the biomethane composition, led to a higher CH_4 concentration in the off-gas stream, which almost reached 1.6% at the end of day 15. Possibly, changing the membrane parameters (e.g. operating temperature, pressure ratios, number of modules, etc.) could reduce this concentration. It is also possible that these fluctuations are within the model's accuracy, but this analysis would require comparing experimental data with model predictions.

In the July-August simulation, there was an increase in biogas production due to a feedstock change (Figures 6.6 and 6.14). The composition of the clean biogas stream (GST4) remained around 54% of CH_4 during the whole period. In August, the biomethane flow rate increase by around 13% compared to July. Despite of that, this stream's CH_4 fraction remained stable at 97.7%, which is suitable for injection into the gas grid. Similar to the January simulation, the GST5's CH_4 fraction was superior to 1%, with a slight decrease in August (Figure 6.15).

Regarding the three-stage membrane separator (3-MEM), its electricity consumption was calculated at around 0.25 kWh Nm^{-3} in all simulations. This values is within the expected range for this kind of technology, which is between 0.18 and 0.35 kWh Nm^{-3} [9]. Therefore, the approach used in the upgrading unit can also fairly represent its power requirement despite its simplicity.

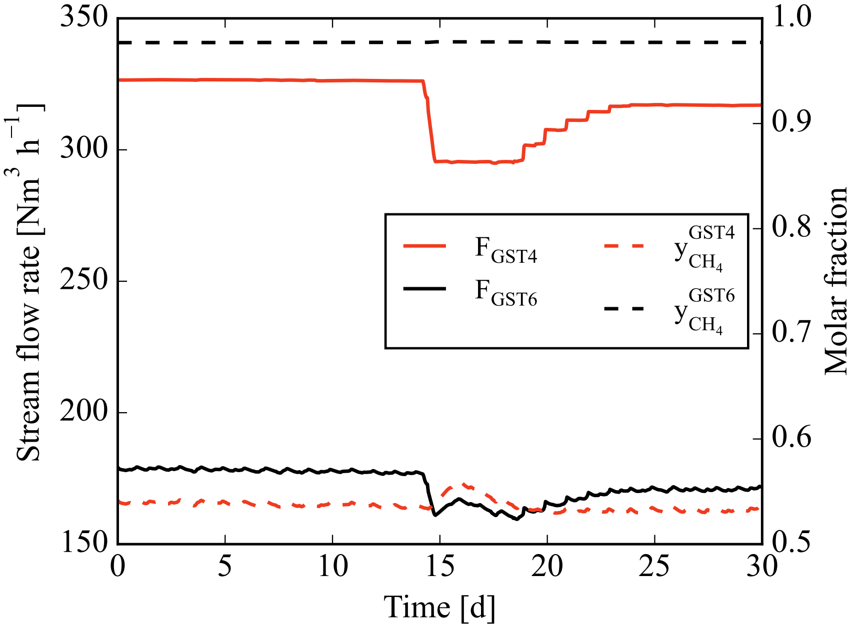

Figure 6.12: Upgrading unit inlet (GST4) and biomethane (GST6) streams flow rate and composition in January with a feed interruption in day 14.

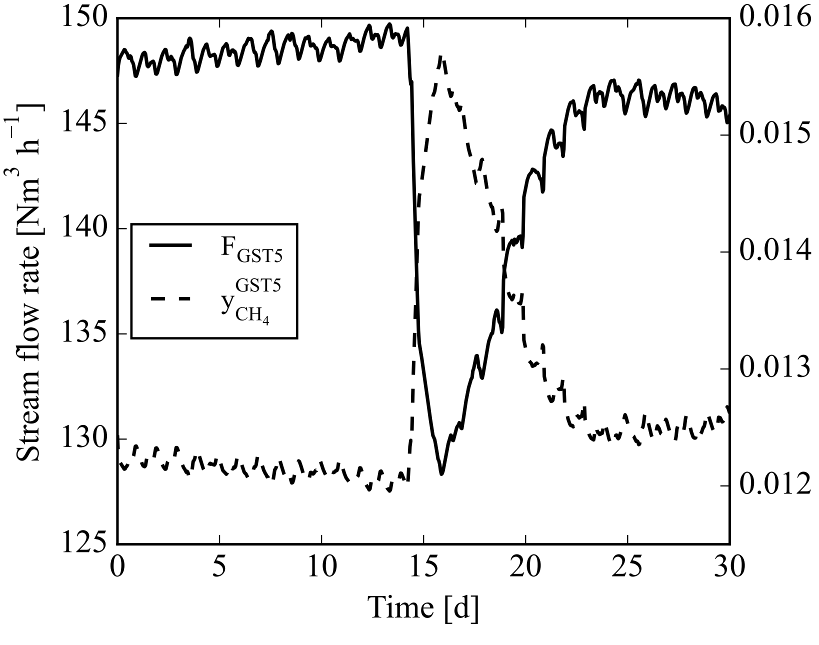

Figure 6.13: Upgrading unit off-gas (GST5) flow rate and composition in January with a feed interruption in day 14.

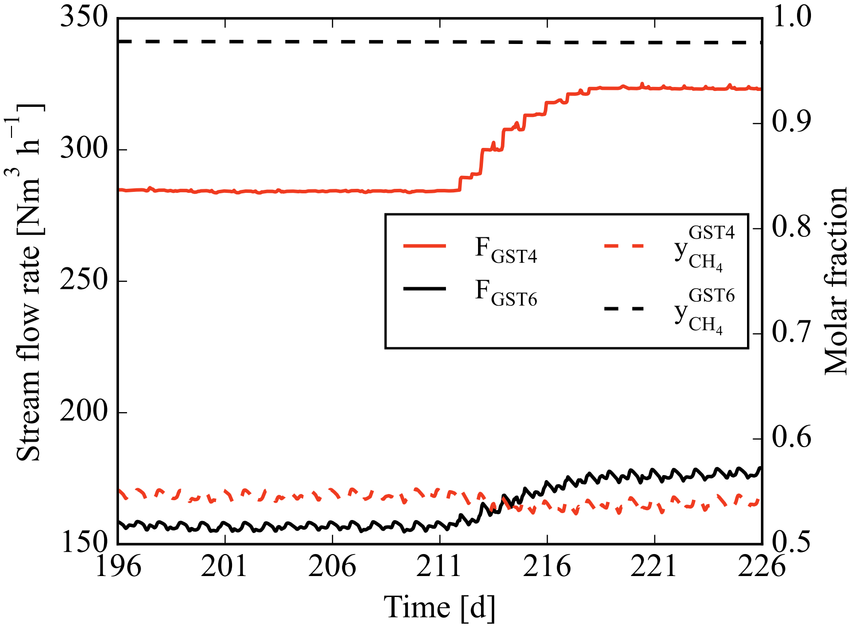

Figure 6.14: Upgrading unit feed (GST4) and biomethane (GST6) streams flow rate and composition from 15 July to 14 August.

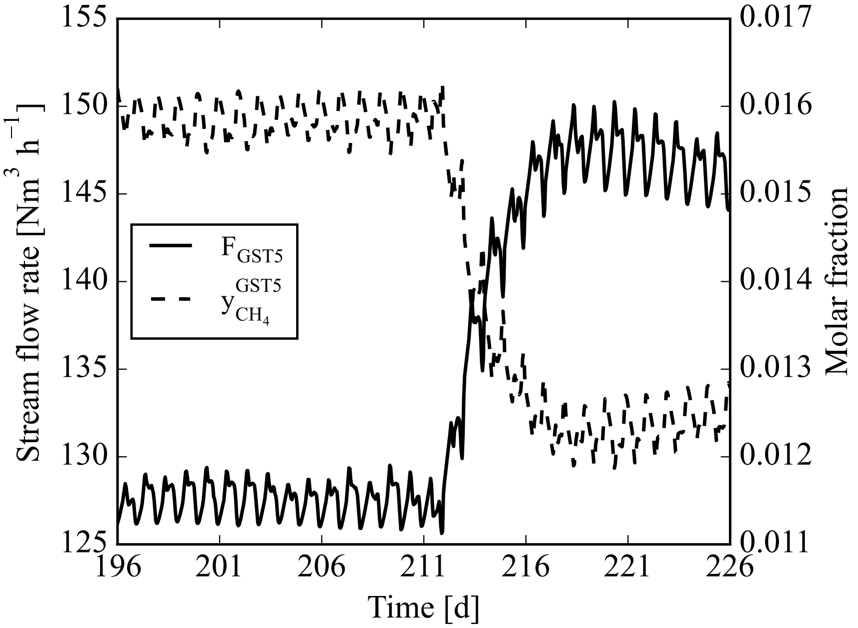

Figure 6.15: Upgrading unit off-gas stream (GST5) flow rate and composition from 15 July to 14 August.

6.2 Integration with P2G

To simulate the P2G plant of Figure 5.2, the model blocks were arranged as shown in Figure 6.16. The off-gas of the biomethane plant's upgrading unit is first mixed with H_2 in stoichiometric proportions (4 H_2:1 CO_2). Then, the resulting stream is compressed to 10 bars and heated to 400 K before entering the first methanation reactor. The outlet stream of CAT1 goes to a chiller, where part of the water vapor is condensed. After this unit, the gas is heated again to 473 K and sent to the second reactor. The CAT2's product stream after condensing and drying corresponds to the biomethane of the P2G plant. The specifications used for each unit are given in Tables 6.2 and 6.3.

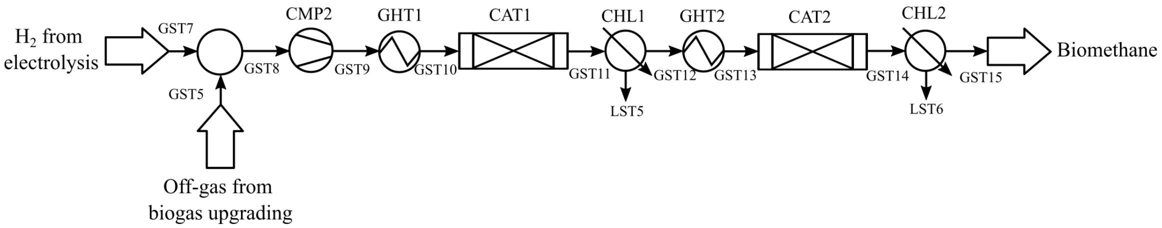

Figure 6.16: Model blocks to simulate a P2G plant

Table 6.2: Methanation reactors specifications

Specification	Reactor		Unit
	CAT1	CAT2	
Number of tubes (n_t)	800	800	
Tube internal radius (R_{reac})	1.0 10^{-2}	1.0 10^{-2}	m
Tube external radius (R_{tube})	1.1 10^{-2}	1.1 10^{-2}	m
Intake/outlet manifold lengths ($L_{int},\ L_{man}$)	0.1	0.1	m
Total length of the tube (L)	4.1	3.1	m
Coolant flow rate (Q_{cool})	1.0 10^{-2}	1.0 10^{-2}	$m^3\ s^{-1}$
Length of each catalyst zone (L_{zone})	1.0	3.0	m
Number of catalyst zones	4	1	
Catalyst concentration in zone 1 ($\rho_{cat}^{mix}(1)$)	45	980	kg m^{-3}
Catalyst concentration in zone 2 ($\rho_{cat}^{mix}(2)$)	80		kg m^{-3}
Catalyst concentration in zone 3 ($\rho_{cat}^{mix}(3)$)	250		kg m^{-3}
Catalyst concentration in zone 4 ($\rho_{cat}^{mix}(4)$)	350		kg m^{-3}
Particle diameter (d_p)	2.0 10^{-3}	2.0 10^{-3}	m
Macroscopic void fraction (ϵ)	0.4	0.4	
Pure catalyst apparent density (ρ_{cat})	890	890	kg m^{-3}

Table 6.3: Specifications of auxiliary units in the P2G plant

Block	Specification	Value	Unit
CMP2	Discharge pressure (P_{out})	10.0	bar
	Isentropic efficiency (η_{ise})	0.8	
	Electric efficiency (η_{el})	0.9	
GHT1	Outlet temperature (T_{out})	400.15	K
CHL1	Outlet temperature (T_{out})	313.15	K
GHT2	Outlet temperature (T_{out})	473.15	K
CHL2	Outlet temperature (T_{out})	283.15	K

The simulations of the methanation reactors were carried out by using the program developed by Fache [126]. His program was coded in Fortran and used DASSL [135] to solve the differential-algebraic system of equations generated by the methanation model (Section 5.3.6) [126]. The input required by the first reactor were calculated and written from the simulation results of the biomethane plant, considering the H_2 addition, the compression and the heat exchanger. On the other hand, the input for the second one was estimated from the output of the first reactor using a Python routine, which also performed the calculations of the chiller (CHL1) and the gas heater (GHT2).

In the simulations, the procedure used to start the methanation reactors were the same one described in the work of Fache [126]. This operation consisted of first heating the inerted reactor until the operating temperature for 600 s. Then, maintaining the heating for another 600 s to stabilize the temperature throughout the entire reactor. After this, a first injection of a mixture of CO_2 and CH_4 in stoichiometric proportions was carried out for 30 s.

In continuous simulations, the flow rate and composition from the biomethane plant were used only after the first injection. Thus, a few disturbances appeared in the first points of these simulations. However, in these cases, only the stable values were analyzed, as it was considered that the methanation reactors would already be in operation before the simulation period. The dynamic behavior of starting-up the reactor and putting it in stand-by was studied in the intermittent operation simulations.

6.2.1 Continuous operation

To evaluate a continuous operation of the P2G plant, the results of the biomethane plant simulation from 15 July to 14 August were used, as it comprehends two different levels of gas flow rate into the P2G plant (Figure 6.15). Besides, another simulation from 15 November to 15 December were carried out to also capture the year highest biomass feed (Figure 6.6). In Table 6.4, the calculation time for each of these study cases is presented.

Table 6.4: Simulation time for each methanation reactor.

Case	Simulation time [s]	
	CAT1	CAT2
15 July - 14 August	1956	16910
15 November - 15 December	2116	14535

From the outlet flow rate of the first catalytic reactor, the CO_2 conversion could be estimated at 96.4% in July and of 94,5% in August (Figure 6.17 (a)). In terms of composition, the variations through the simulation were barely noticeable, with CH_4 fraction at around 30.7% in the whole period (Figure 6.17 (b)). Despite of the high conversions, a second reaction stage would still be required, as the dry gas composition of CAT1's outlet would be composed by 77.7% of CH_4, which is not suitable for grid injection. Indeed, from a CO_2-CH_4 mixture in stoichiometric proportions, a CO_2 conversion of 99% would be required to reach 95% of CH_4 in the dry gas.

The maximal temperature in the gas phase varied according to the feed flow rate, with values close to 662 K in July and to 670 K in August (Figure 6.18). This marginal increase took place because of the augmentation in the reactor feed, which led to higher energy released by the reactions. The gas temperature profile in the reactor at the end of the simulation shows that the reagent conversions are concentrated in the beginning of each catalyst zone, as indicated by the temperature spikes (Figure 6.18). Although most of the conversion occurred in the first three regions of the reactor, the forth one was included to obtain the highest possible conversion before the following reaction stage.

In the second reactor, CAT2, the overall CO_2 conversion reached 99.4% in July and 98.6% in August (Figure 6.19). Similarly to the effluent of the first methanation reactor, the gas composition did not have a relevant variation, despite the increase in the feed flow rate. This indicates that the residence time is not limiting extent of the reactions, thus a smaller reactor could be considered.

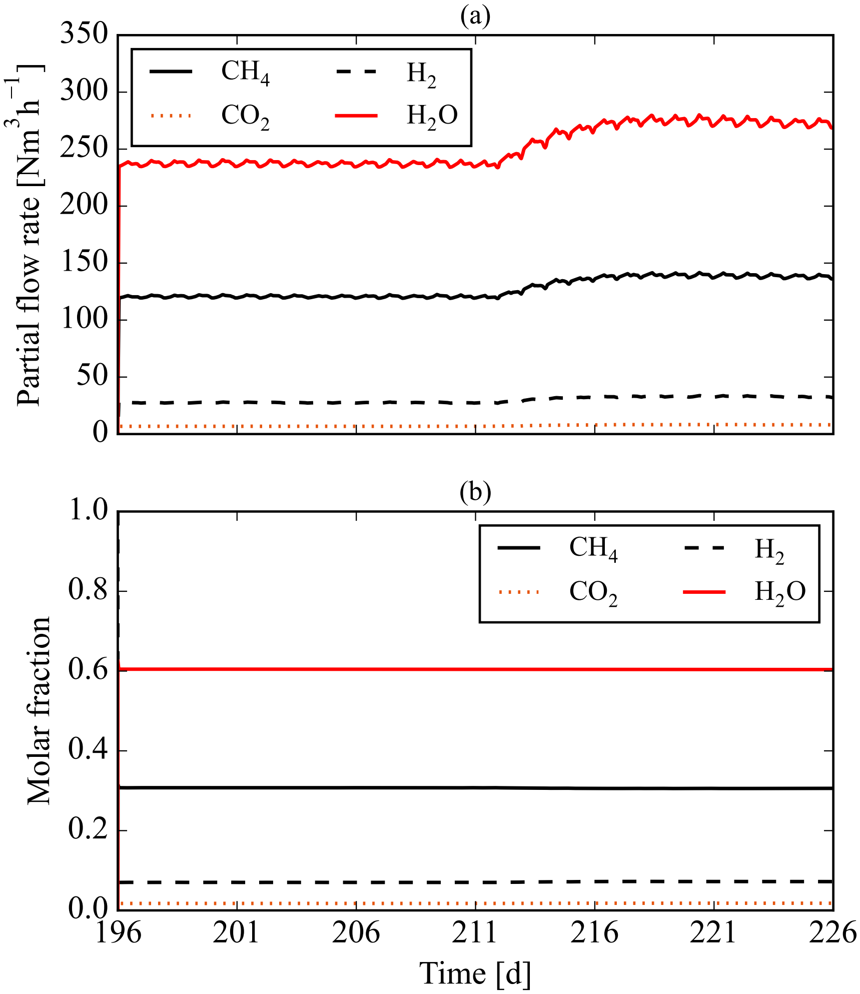

Figure 6.17: CAT1's outlet flow rate and composition.

However, at the same time, the dry composition of CAT2's outlet does not have a large margin compared to the specifications to grid injection, as a slight reduction in CO_2 conversion would increase H_2 above the limit of 6% (Figure 6.20) [15].

In December, the flow rate of GST5 was 12.3% higher compared to November and 23.0% to August (Figure 6.21). Considering that this stream was totally sent to the methanation reactors, a temperature runaway occurred in CAT1, where maximal gas temperature exceeded 800 K as a hot-spot was formed at the beginning of the second catalyst zone (Figure 6.22). This result indicates that a special attention should be paid in designing the catalytic reactors and their gas treatment capacity, as feedstock variations in the biogas plant could lead to thermal runaway in the reactors

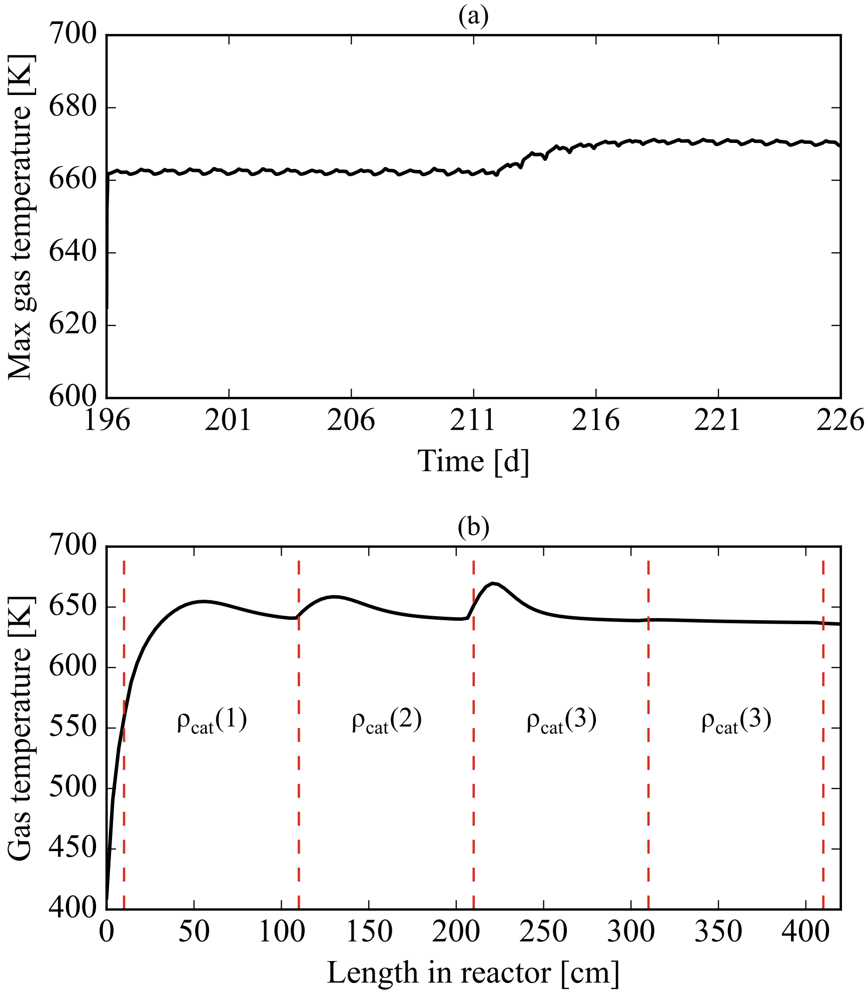

Figure 6.18: CAT1’s maximal temperature from 15 July to 14 August (a) and temperature profile at the end of the simulation (b). In (b), the dotted lines delimit each different catalyst region.

by reagent overflow.

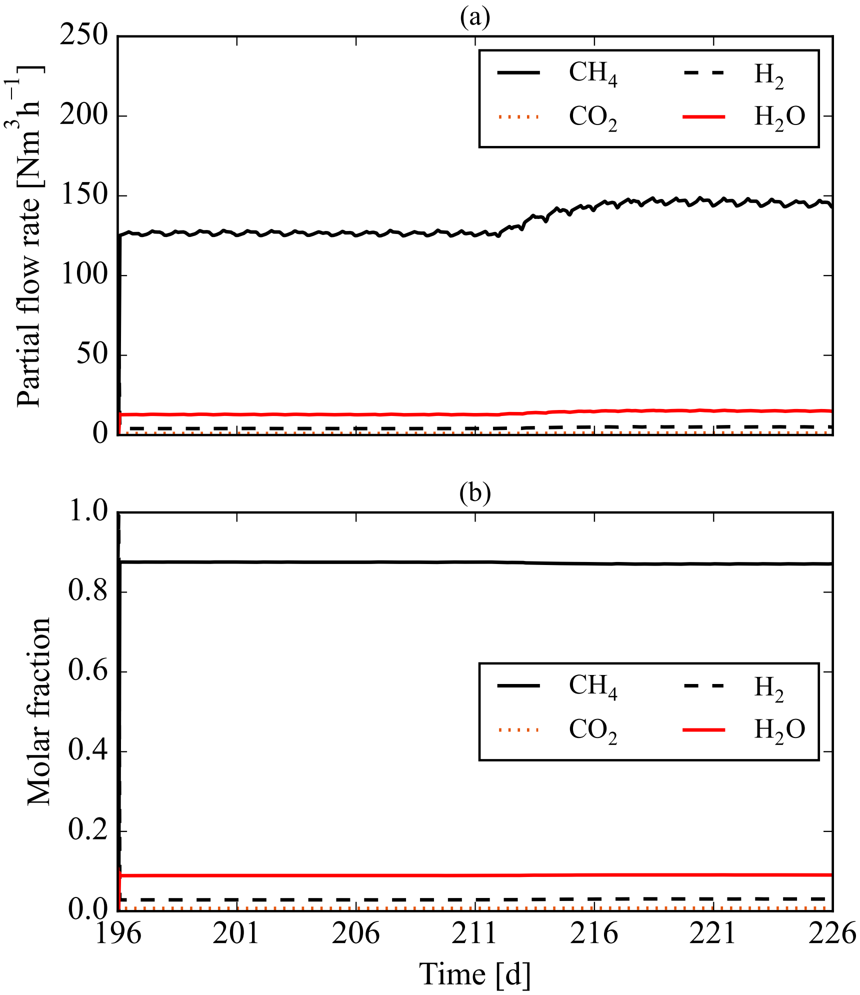

Figure 6.19: CAT2's outlet flow rate and composition.

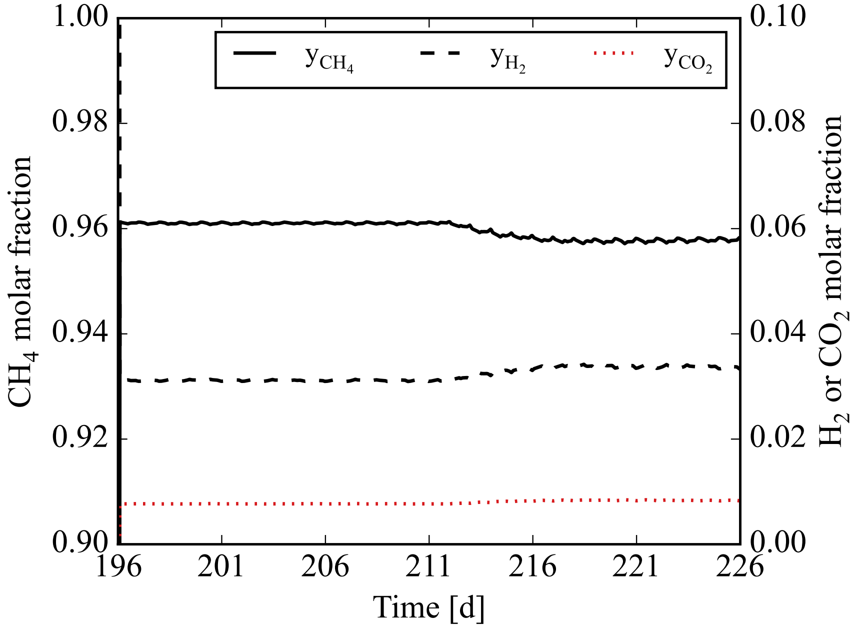

Figure 6.20: CAT2's outlet dry gas composition.

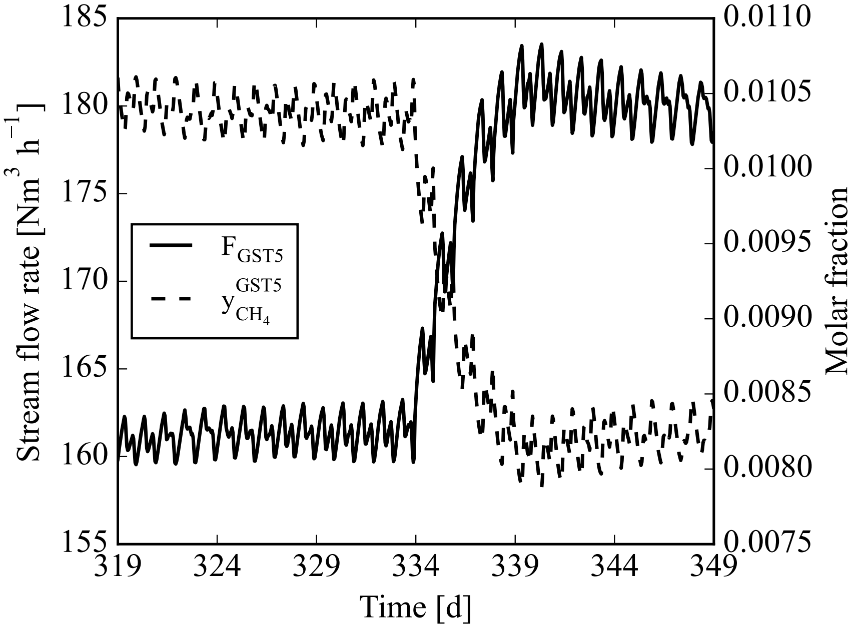

Figure 6.21: Upgrading unit off-gas stream (GST5) flow rate and composition from 15 November to 15 December.

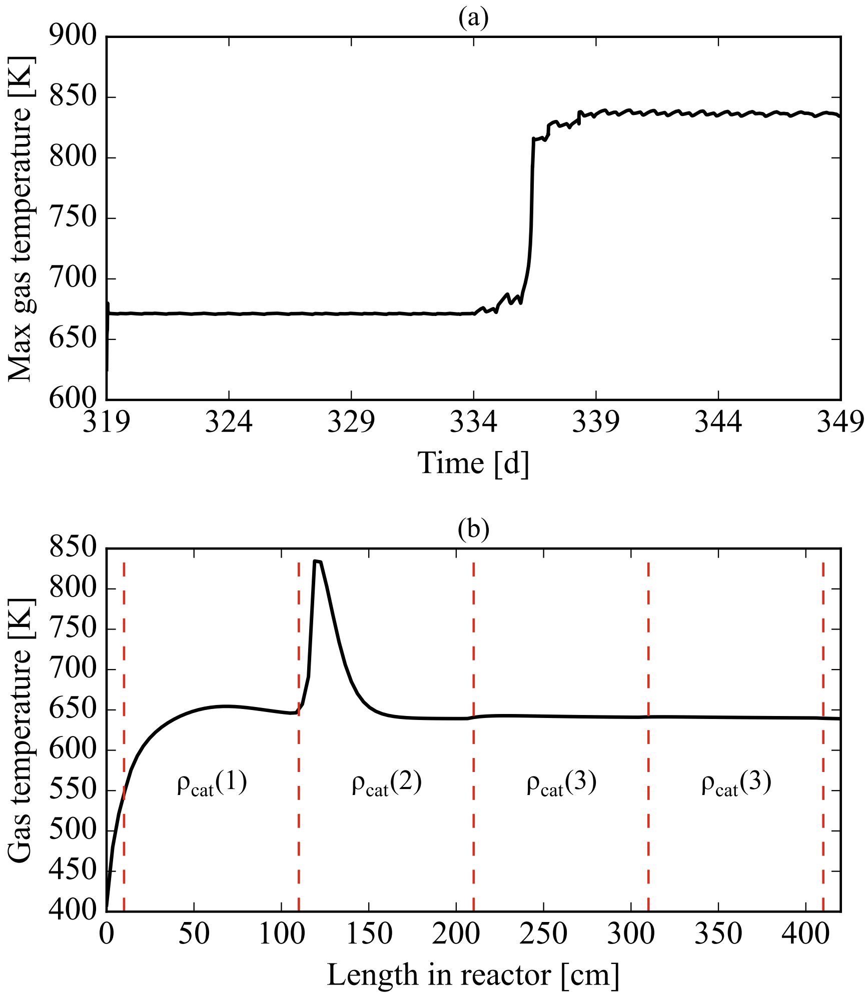

Figure 6.22: CAT1's maximal temperature from 15 November and 15 December (a) and temperature profile at the end of the simulation (b). In (b), the dashed lines delimit each different catalyst region.

6.2.2 Intermittent operation

One of the main objectives of the P2G concept is to store excess electricity of the energy grid [13]. In this case, the operation of the methanation reactors would be dynamic according to the availability of surplus energy [136]. To account this kind of scenario, a criteria should be used to decide the operation schedule of the P2G plant.

The French electricity transmission system operator (*Réseau de Transport d'Èlectricité* - RTE) publishes several data on power generation and consumption in France [137]. The data on pumped-storage power was used as indicator of surplus energy availability in the grid. Indeed, pumped hydropower storage is currently the most established technology employed to absorb and store energy from the grid [138]. This technology consists of pumping water from a lower reservoir to a higher one when the electricity demand is low and use it to generate electricity when the demand is high [138, 139].

The total energy stored by hydropower plants was calculated for each hour of the day based on the data of power generation in France in 2022 [137] (Figure 6.23). Although this kind of power plant can work at any time of the day, most of the energy stored occurred during the night and in the afternoon. The former period consists of the moment of the day with the lowest electricity demand, while the latter, besides having a relative low demand, is also influenced by renewable energy generation, especially solar power [140]. Thus, two working periods per day were assumed for the P2G plant: a fixed one from 1:00 until 6:00; and a variable one from 12:00 until 18:00 according to the solar irradiance. In the second period, the methanation reactors would be operated only during the times when the GHI is higher than 600 kW m^{-2} and if these periods last at least 2 h.

Simulation setup

Two three-day periods were simulated to evaluate the winter and the summer seasons: 15-17 February and 20-22 July. Here, the meteorological data for a TMY were obtained from PVGIS using the coordinates of Pau, France (+ 43.300, - 0.403) [141]. The initialization of both reactors was initially carried out as described previously in Section 6.2. However, after the first injection, the feed was kept constant for 600 s, then the reactors were put in stand-by for 1200 s. The stand-by

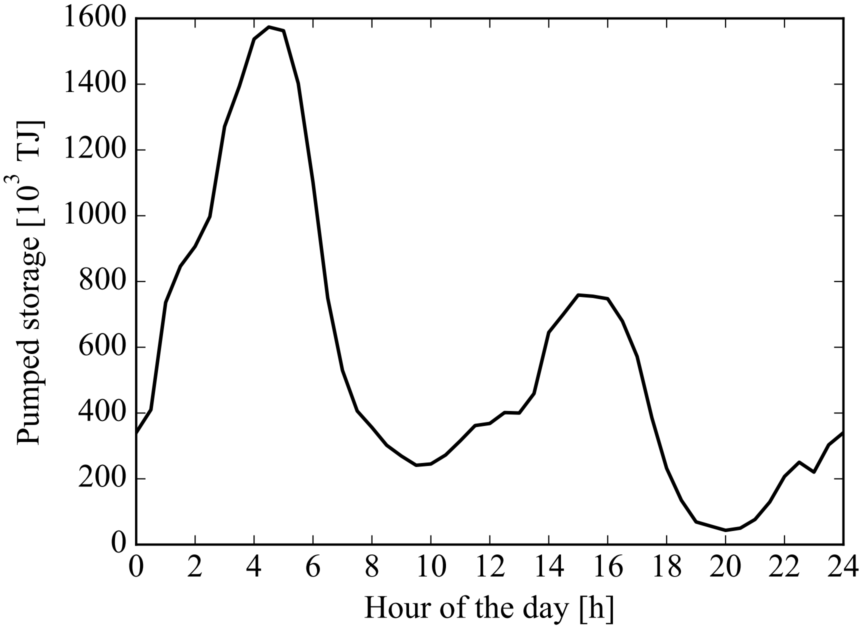

Figure 6.23: Pumped hydroelectric energy stored in France in 2022 per hour of the day.

mode of the reactors consists in no reagent input and a direct recirculation of the coolant, which enters at the same temperature it leaves the reactor, thus avoiding a fast temperature decrease of the reactor [126]. After these procedures, the next injections were carried out with the off-gas stream of the biomethane plant. The transition to stand-by mode was done by first cutting off the GST5 (i.e. the CO_2 supply) with a ramp of 30 s, and then cutting the H_2 feed with a ramp of 30 s as well, as recommended in the work of Fache [126]. To restart the reactor, GST5 and H_2 were injected at stoichiometric proportions with a ramp of 30 s until their full value, and the coolant was reheated to its set value. The calculation times for each evaluated scenario are exhibited in Table 6.5.

Table 6.5: Simulation time for each study case of intermittent operation

Case	Simulation time [s]		
	Biomethane plant	CAT1	CAT2
15-17 February	370	1227	26304
20-21 July	356	1717	29140

Winter season

In February, there was not enough solar irradiance during the considered interval (Figure 6.24). Therefore, the catalytic reactors were operated only during the night, totaling 18 hours in this period. The off-gas stream coming from the upgrading unit (GST5) consisted of 98.6% of CO_2 with a flow rate of approximately 138 Nm^3 h^{-1}. In CAT1, this stream was converted into around 129.5 Nm^3 h^{-1} of CH_4, thus corresponding to a carbon dioxide conversion of 95.2% (Figure 6.25 (a)), which is in line with the results obtained for a continuous operation (Section 6.2.1).

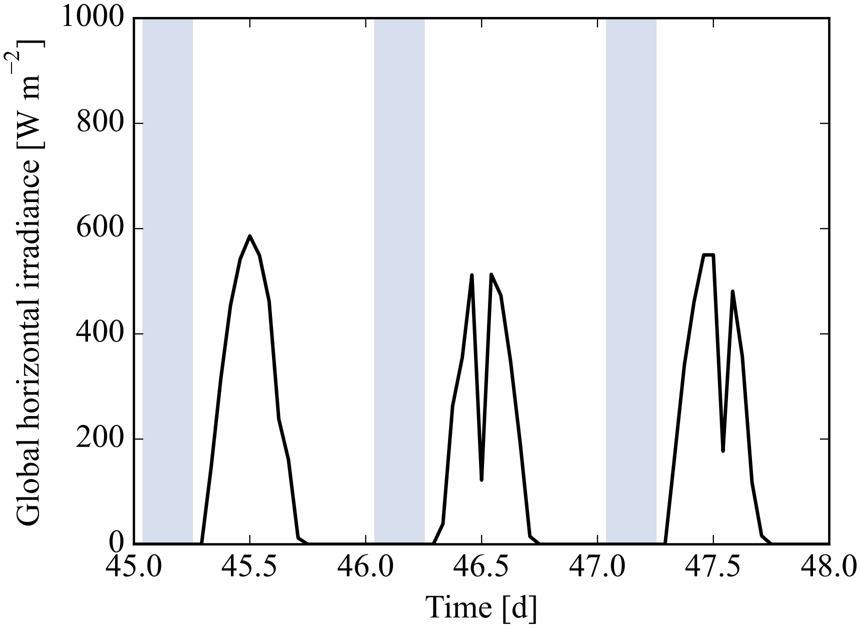

Figure 6.24: Global horizontal irradiance from from 15 (day 45) until 17 (day 47) February in Pau for a TMY. The highlighted zones correspond to the working hours of the P2G plant.

After each injection, there was a spike of H_2 in the effluent. This effect occurred because the reactor was overflown with hydrogen when it was put in stand-by mode. Besides, a momentaneous temperature peak reaching up to 678 K could also be observed at the start of each operation, which is linked to higher reactions rates when the reagents were first introduced (Figure 6.25 (b)). Briefly after, the hot-spot temperature stabilized around 667 K. In stand-by mode, the coolant was only recirculated in the reactor, which led to a linear decrease of the gas temperature of about - 1.7 K h^{-1}, reaching a minimum value of 602 K just before the next reactor start-up.

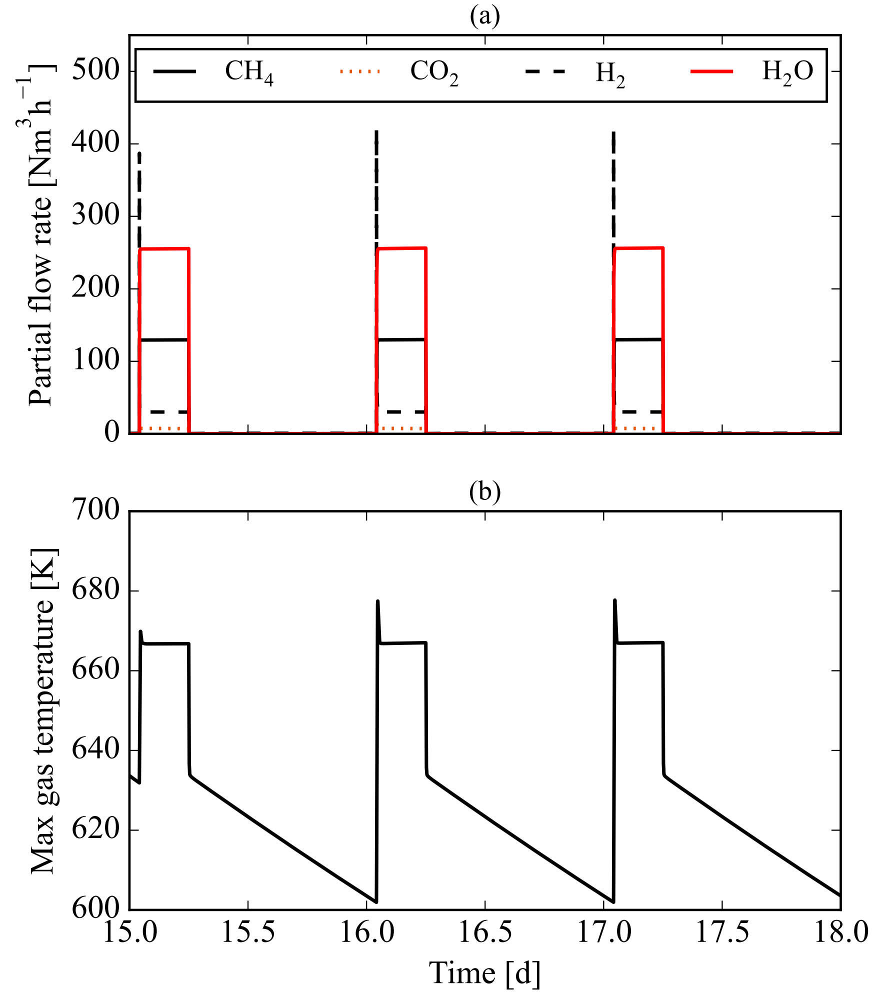

Figure 6.25: CAT1 outlet flow rate (a) and maximal gas temperature (b) in the reactor from 15 to 17 February with intermittent operation.

Using the day 16 as reference, it took 6.5 minutes to methane flow rate reach 99% of its steady value (Figure 6.26). This demonstrates that the adopted reactor structure and the start-up procedure enable a relatively quick start-up. This feature is particularly important for intermittent operations, as it reduces the duration of off-spec gas production. On the other hand, the transition to stand-by mode went considerably faster, with methane flow rate reducing to zero in 45 seconds.

Still on day 16, the gas temperature rose as soon as the injection started (Figure 6.27). Such effect occurred because, at first, the coolant was reheated until its set temperature instead of being directly recirculated, and the reactions started to generate heat. This initial temperature peak was stabilized in about 12 minutes, and, at the end of the production period, the feed cut-off led to a

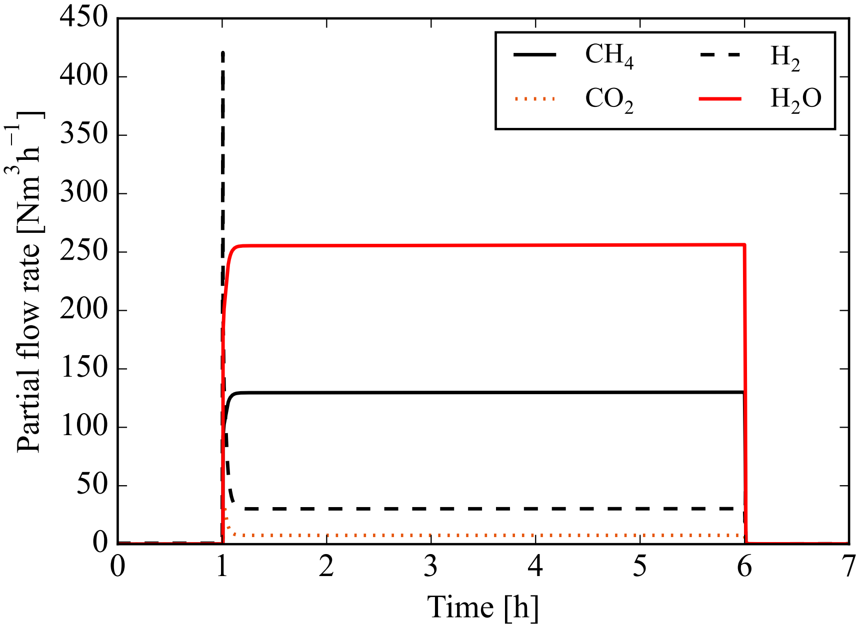

Figure 6.26: CAT1 outlet partial flow rates on 16 February.

quick reduction from 667 K to 634 K in 6 minutes.

In the second reactor, the trend was similar to the first one (Figure 6.28). However, the temperature values were lower, around 626 K during the operation time, due to much lower reaction rates in this unit. The overall CO_2 conversion reached 99.8% and the dry gas composition met the injection specifications (Table 6.6). In Table 6.6, the day 16 February was used again as reference because there was not a significant difference compared to the other days.

Table 6.6: Flow rate and compositions at steady operation on 16 February

Stream	Flow rate [Nm^3 h^{-1}]	Composition [%]				
		CH_4	H_2	CO_2	H_2O	CO
CAT1 inlet (GST10)	680.8	0.3	79.8	19.9	0.0	0.0
CAT1 outlet (GST11)	422.1	30.6	7.2	1.8	60.4	<0.1
CAT2 inlet (GST13)	169.2	76.8	18.0	4.5	0.7	<0.1
CAT2 outlet (GST14)	155.1	87.3	2.9	0.7	9.0	<0.1
P2G Biomethane (GST15)	141.1	95.9	3.2	0.8	0.0	<0.1

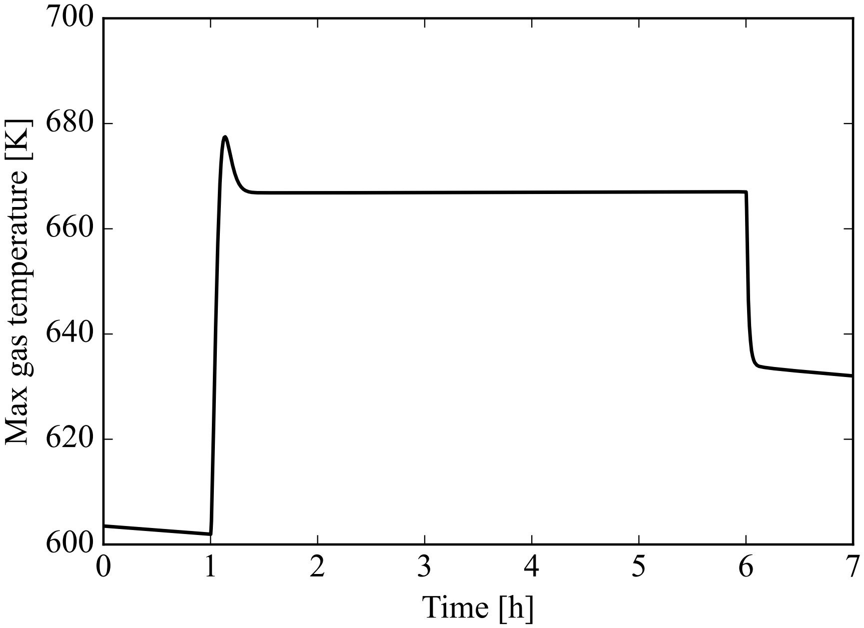

Figure 6.27: CAT1 maximal gas temperature on 16 February.

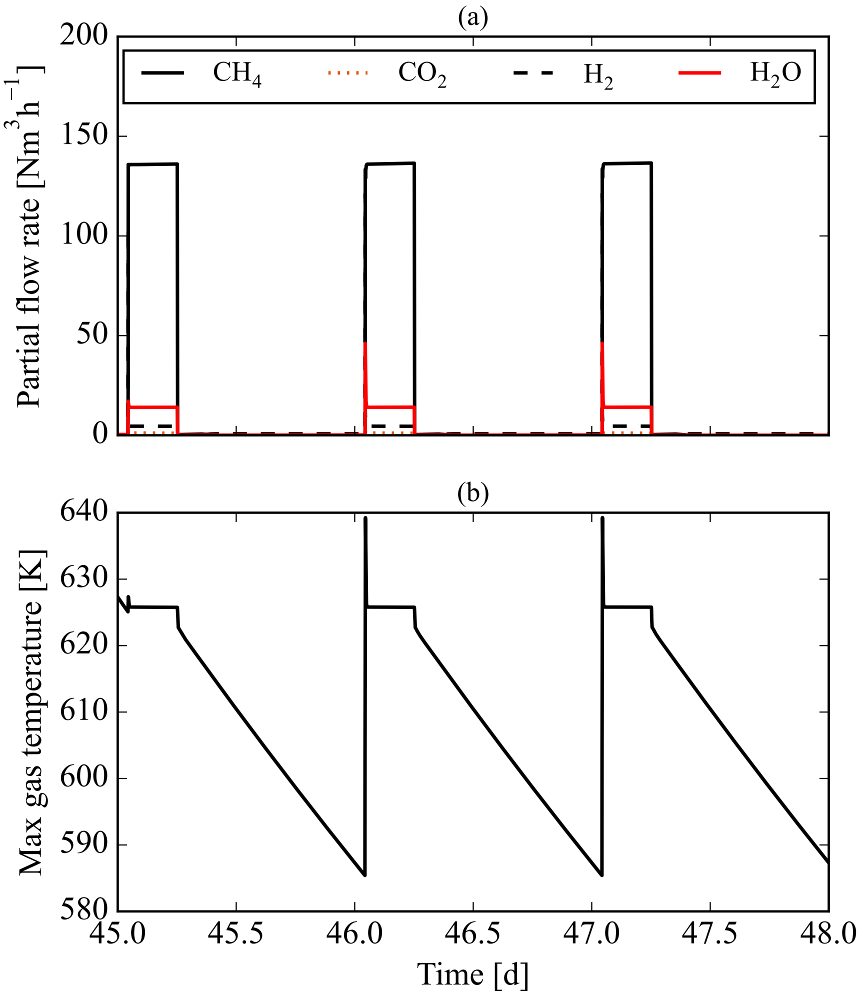

Figure 6.28: CAT2 outlet flow rate (a) and maximal gas temperature (b) in the reactor from 15 to 17 February with intermittent operation.

Summer season

In July, the catalytic reactors were operated both in the night and the day periods, as GHI reached values above 600 W m^{-2} in all the afternoons (Figure 6.29). The total working hours were 18 hours during the night and 11 hours in the afternoons. The off-gas coming from the biomethane plant consisted of 126.1 Nm^3 h^{-1} with 98.4% of CO_2 in average.

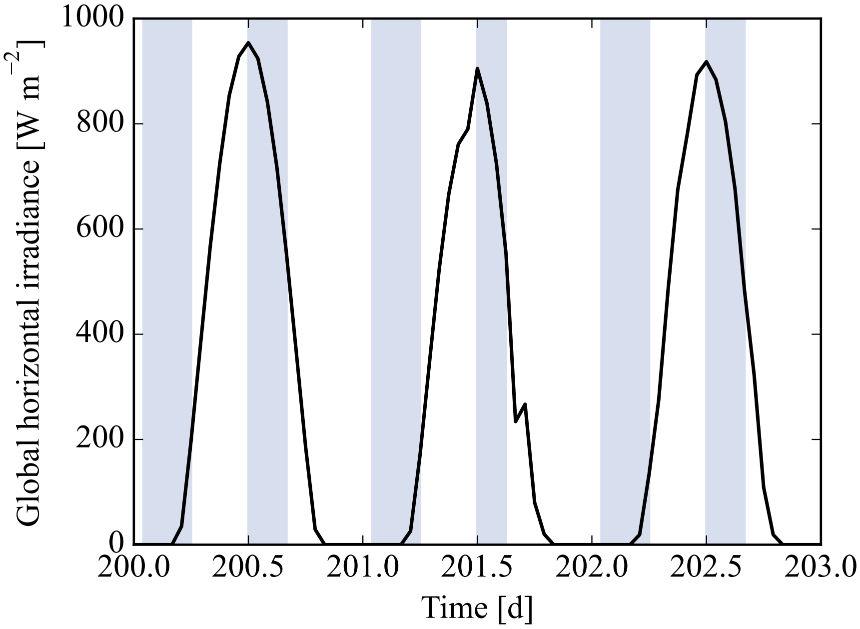

Figure 6.29: Global horizontal irradiance from from 20 (day 200) until 22 (day 202) July in Pau for a TMY. The highlighted zones correspond to the working hours of the P2G plant.

In CAT1, the CH_4 production reached approximately 119.3 Nm^{-3} h^{-1}, and, in the second one, it augmented to 125.1 Nm^{-3} h^{-1} (Figure 6.30). In terms of CO_2 conversion, these values corresponded to a 94.6% conversion in the first reactor and 99.2% in the second one.

Besides increasing the biomethane production, the higher number of operating periods also reduced the temperature drop of the reactor, which minimum was about 3% higher compared to the winter period (Figure 6.31). In stand-by mode, the temperature drop was also approximately linear at a rate of - 1.8 K h^{-1} in CAT1 and - 2.1 K h^{-1} in CAT2. The difference between the two studied periods occurred especially due to the shorter gaps in the July in relation to February.

Using again the middle day as reference (i.e. 21 July), from the beginning of feed injection,

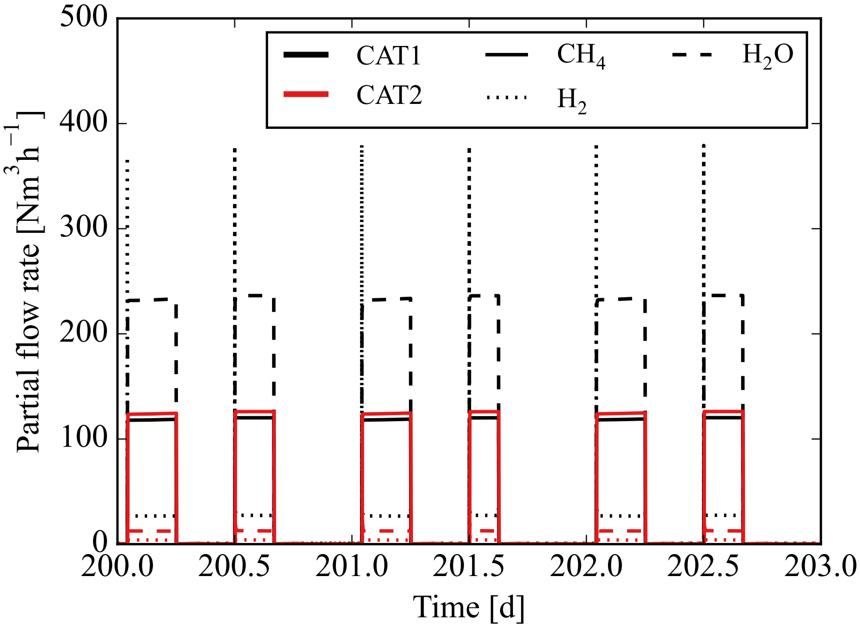

Figure 6.30: Catalytic reactors outlet partial flow rate on 20, 21 and 22 July for an intermittent operation.

99% of the steady CH_4 was reached within 6 min in CAT1 and 8.4 min in CAT2 (Figure 6.32). Regarding these dynamics, there were not remarkable differences between the night and the afternoon operations.

An intermittent operation of the P2G plant according the surplus electricity availability led to a seasonal variation between Summer and Winter season (Table 6.7). Due to a higher solar irradiance in July, the P2G operated during more hours in this month compared to February, when the reactors were active only during the night. This difference impacted directly the methane production, which was 1.58 fold higher in July, with an overall conversion of total available CO_2 at 35.3%, while it was at 20.3% in the Winter period. The biomethane in both periods had a composition of around 96% of CH_4, 3% of H_2, and 1% of CO_2, which is within grid injection specifications.

In these study cases, the hydrogen production was supposed to be non-limiting. However, as the surplus electricity would be used to power the electrolyzer in an actual situation, including this other reactor would allow to truly study the capacity of the P2G plant to produce under real conditions. Besides, it was supposed that the catalytic reactors would either treat the full stream coming from biomethane plant or it would be put in stand-by mode. Other intermediary cases could be possible

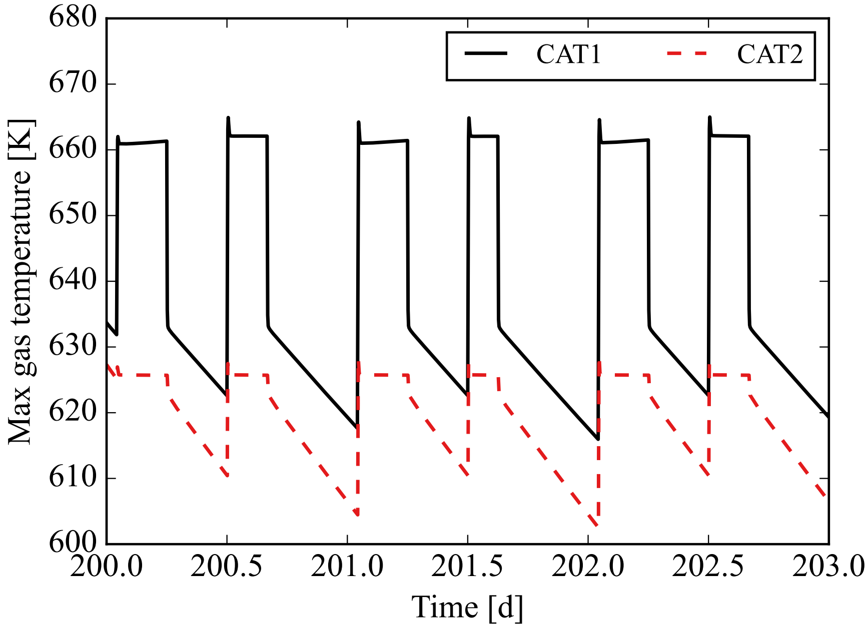

Figure 6.31: Maximal gas temperatures in CAT1 and CAT2 on 20, 21 and 22 July for an intermittent operation.

according to surplus energy availability. For instance, working at intermediate capacity levels, in which only a portion of the available off-gas would be treated. Nevertheless, the tools developed in this work allowed to estimate the additional production of CH_4 from the valorization of an off-gas of the biomethane plant.

Table 6.7: Summary of P2G plant production for summer (20-22 July) and winter (15-17 February) operations. Only the on-spec biomethane production in the P2G plant was considered.

Metric	15-17 February	20-22 July
Total CO_2 in off-gas [Nm^3]	9784.2	8934.1
P2G plant working time [h]	18	29
Total CH_4 produced [Nm^3]	1990.3	3151.3
Total H_2 in biomethane [Nm^3]	67.2	101.5
Total CO_2 in biomethane [Nm^3]	16.6	25.1

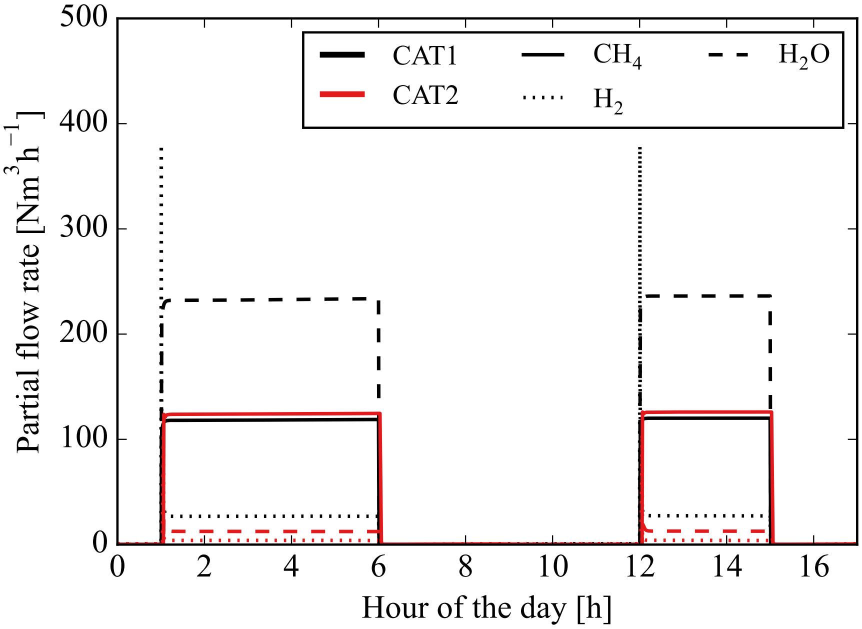

Figure 6.32: Catalytic reactors outlet partial flow rate on 21 July.

6.2.3 Process safety remarks

It was shown in Section 6.2.1 that a feed overflow into the catalytic reactors can lead to a thermal runaway (Figure 6.22). In addition to this situation, an eventual reduction in reagent conversion and its effects in the thermal stability of the reactor was analyzed here. When using the off-stream from a biomethane plant, a catalyst poisoning with H_2S would be of particular interest given that this contaminant is present in raw biogas. Although this compound is removed in the biogas cleaning step, if, due to a dysfunction in this stage, H_2S reaches the methanation reactor, it would poison the catalyst and thus reduce its efficacy. Other situations could also lead to a similar effect in reaction rates. For example, if the temperature of the coolant would drop following an operation error or equipment malfunction.

In the current model, catalyst poisoning cannot be simulated. For this reason, to reduce the reaction rates, the temperature of the heat exchange fluid was reduced instead. This simulation was carried out by considering a cold start-up of the reactor as previously explained in Section 6.2. A constant feed of 640 Nm^3 h^{-1} of H_2 and CO_2 mixture in stoichiometric proportions was used. After the first injection with a ramp of 30 s, the model parameters were kept constants for 600 s to stabilize the reactor. Then, the coolant entry temperature was reduced by 10 K with a ramp of 30 s. After each temperature change, the reactor was simulated for 600 s. This procedure was repeated from an initial temperature of 623.15 K until 593.15 K (Figure 6.33). The same structure as CAT1 (Table 6.2) was used.

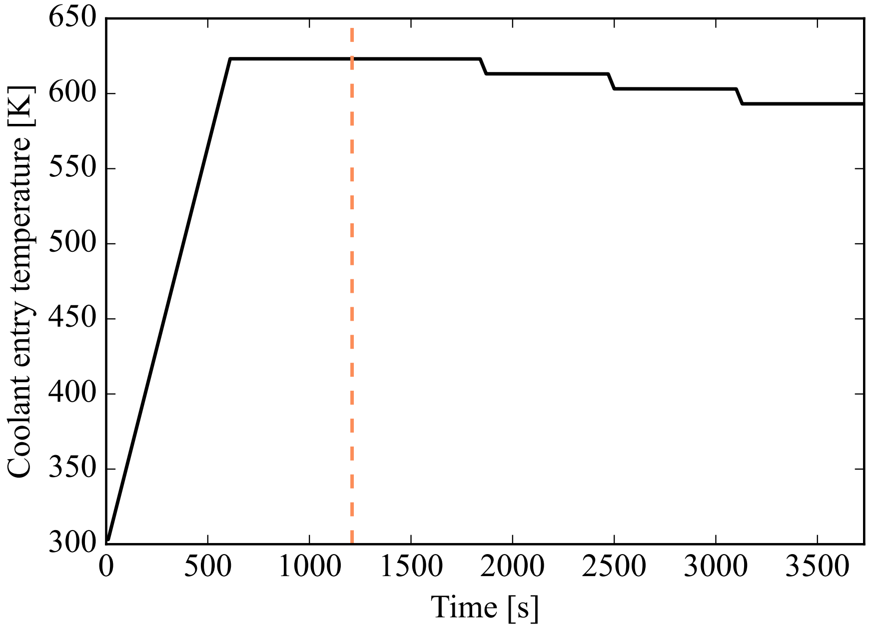

Figure 6.33: Coolant entry temperature into the reactor. The vertical dashed line indicates the time when the feed injection started.

The maximal gas temperature increased as the coolant temperature decreased (Figure 6.34). The gas temperature surpassed 773 K at 2833 s, when the coolant temperature was at 603.15 K. Therefore, reducing the heat exchanger fluid temperature led to a thermal runaway of the catalytic reactor, even though one could expect that using a colder coolant would instead help to prevent it.

When the coolant was at 623.15 K, the gas temperature within the reactor presented a slight increase at the initial section of each catalyst zone (Figure 6.35, t = 1840 s). As the heat exchange fluid was cooled down, the overall gas temperature also reduced. However, at the same time, it led to a formation of a hot-spot at the start of the third catalyst zone, thus indicating that the reactions concentrated in this region. In fact, the temperature reduction impaired the conversions in the first two zones. At t = 1840 s, the CO_2 molar fraction went from 20% at the reactor inlet to less than 8% at the end of the second zone (Figure 6.36). With a coolant temperature at 593.15 K at t = 3730

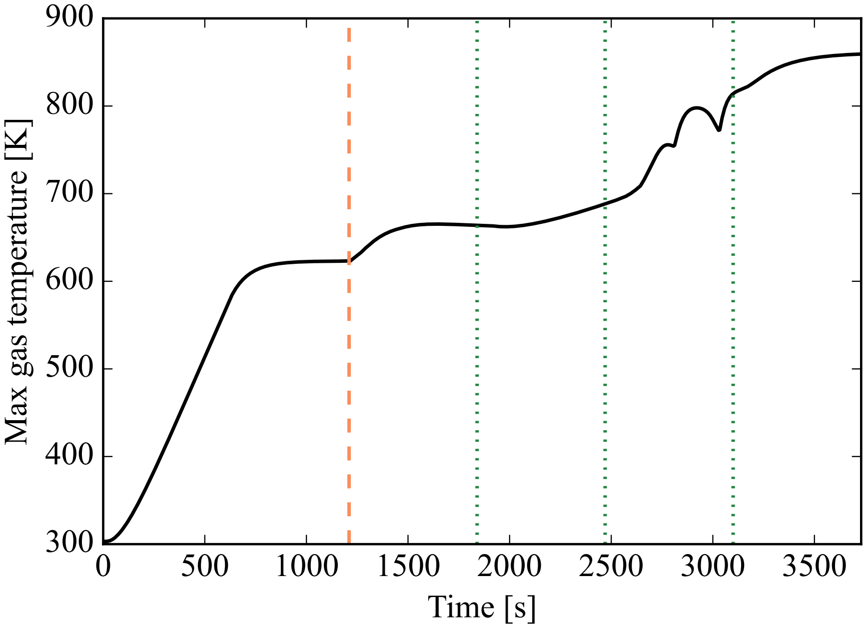

Figure 6.34: Maximal gas temperature in the reactor. The vertical dashed line indicates the start of the feeding and the dotted lines the changes of the coolant temperature.

s, this value was at almost 16% in this same position. As the third zone has a much higher catalyst concentration compared to the first two regions, the higher reagent concentrations compensated the temperature reduction, leading to the formation of the hot-spot.

Therefore, when employing multiple catalyst zones with increasing concentration, a special attention should be paid to any factor that could impair the conversion in the reactors. An analogous reasoning could be applied to the second reaction stage. A reduction in the reaction extent in the first reactor would lead to more reagents arriving to the second one, which operates with a much more elevated catalyst concentration, and thus possibly leading to a thermal runaway as well.

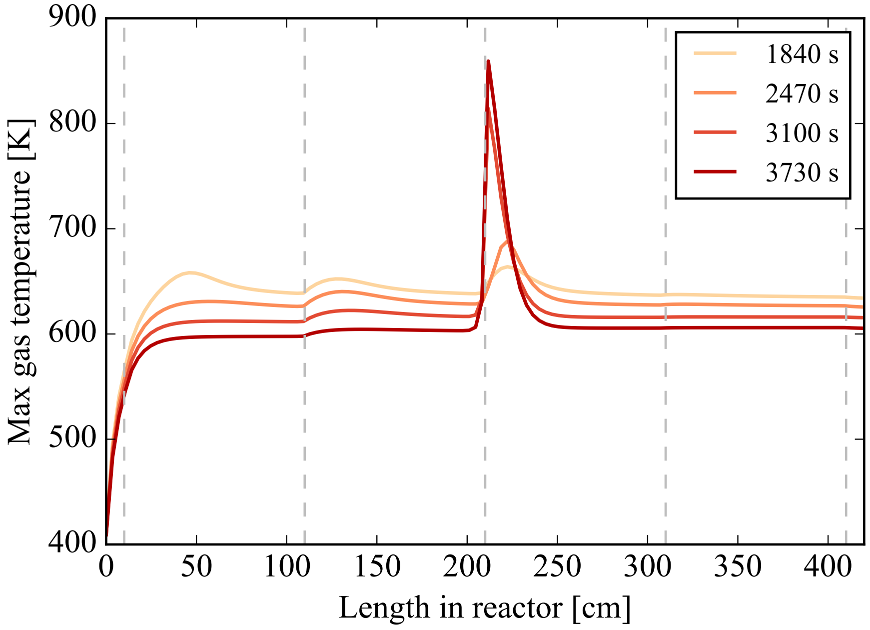

Figure 6.35: Time profile of the gas temperature in the catalytic reactor. The vertical dashed lines delimit each catalyst zone. Each curve correspond to the profile to the moment before each coolant temperature change.

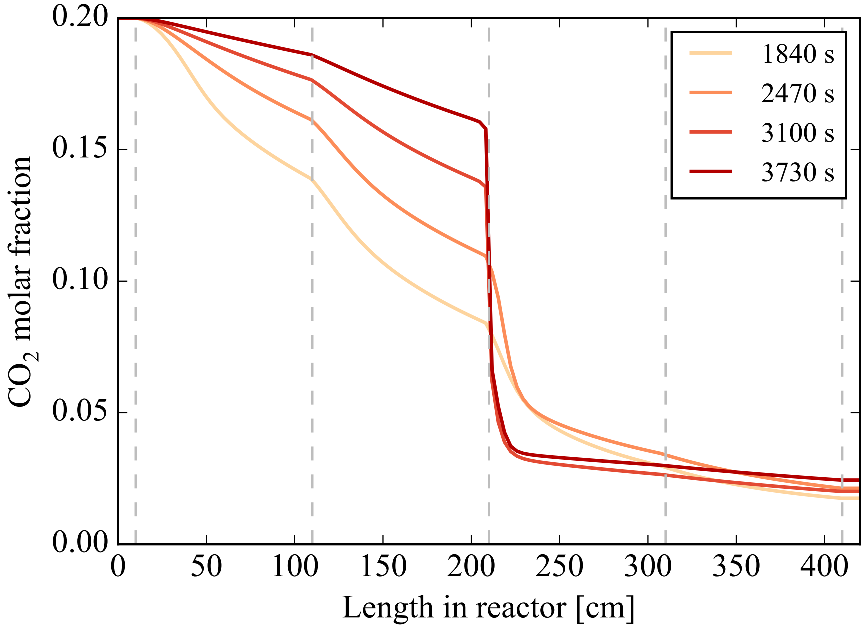

Figure 6.36: Time profile of the CO_2 molar fraction in the catalytic reactor. The vertical dashed lines delimit each catalyst zone.

6.2.4 Heat recovery strategies

In biogas plants, the digesters are the main heat sinks, as they require thermal energy to compensate the heat losses to the environment. Often, a fraction of the biogas produced is used to generate the necessary heat, with this auto-consumption potentially reaching up to 15% of the total production [46]. In Chapter 3, it was shown that lowering such self-consumption can positively impact the plant's carbon footprint and energy efficiency.

Given that the methanation reaction is exotermic (Eq. 5.34), the P2G plant possibly presents some opportunities to significantly reduce biogas self-consumption. In addition, several other units require heating or cooling utilities, which can also aid in the plant's thermal integration. Therefore, this section aims to utilize the developed models to asses thermal energy sources and sinks, and identify potential synergies between the biomethane plant and the catalytic methanation reactors. The results from the intermittent operation of the P2G plant were used in this evaluation (Section 6.2.2).

In February, the heat demand in the whole installation varied between 47 and 92 kW (Figure 6.37). Using the same assumptions employed in Section 6.1.1, the self-consumption in the biogas plant would be at 4.4% to heat the digester and the post-digester. In the membrane separator, it was supposed that only half of the heat removed from the gas stream could be used for heating. Indeed, after the compression to 20 bar in this unit, the gas temperature reached 616.4 K, and then it was cooled down to 278.15 K prior to injection in the first separation stage. Thus, only part of this stream energy would be possible to recover as a hot utility, while the remaining portion would require the use of a cold one. If the thermal energy available from the 3MEM was recovered, it would be able to attend more than 50% of the heat needs of DIG1 and DIG2.

The operation hours of the P2G plant were marked by a net positive heat production in the entire system. Most of this thermal energy production took place in the first catalytic reactor, which released 220.7 kW while in operation. CAT2 was in fact a heat sink, with its demand at 1.13 kW, as the energy released by the reactions did not compensate the heat losses to the external environment. This occurred because the reactions extent in this second reactor was much lower in relation to the first one. GHT1 worked in fact as a chiller and it can be considered a potential heat source because the compressed gas entered this unit at 522.4 K and left at 400.15 K. On the other hand, GHT2 heated the chilled gas from 300.15 K until 473.15 K, thus requiring a thermal energy input.

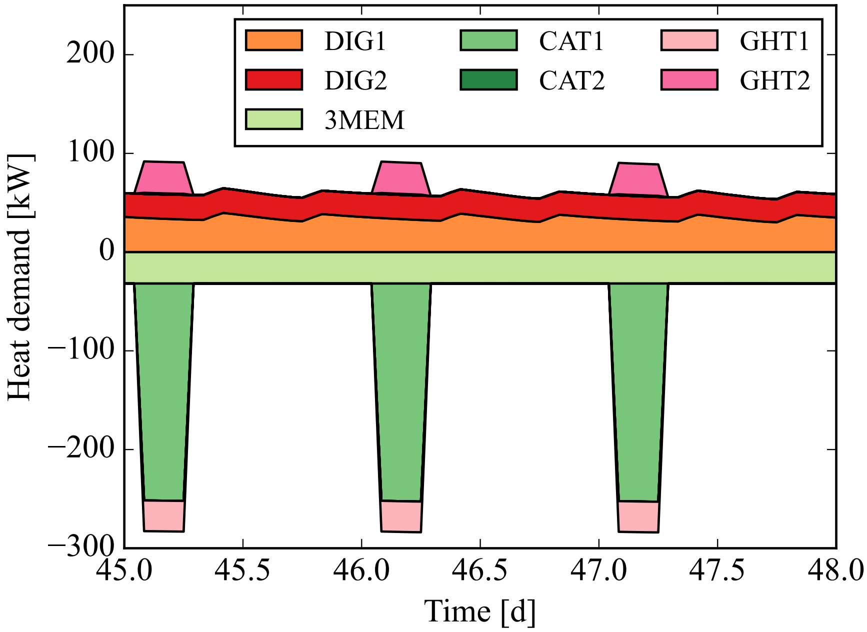

Figure 6.37: Heating utility demand on 15, 16 and 17 February in the whole plant (biomethane and P2G) with intermittent operation of the P2G plant. Positive values indicate a heat consumption, and negative values heat production. 3MEM values correspond to half of the calculated power of the upgrading unit's heat exchanger.

The heat demand trend in the July simulations was similar to the one obtained in February (Figure (6.38). However, the time gaps between the working periods of the P2G were shorter as there was enough solar irradiance to start the catalytic reactors in the afternoons. In the biogas digester, the heat demand decreased from around 59.6 kW in February to about 42.4 kW in July. Thus, the heat production in the P2G was higher in the Season with lower heat demand.

In both studied periods, there was an overall net positive thermal energy generation (Table 6.8). However, the heat generation was concentrated in the P2G plant's operating hours. This means that a thermal energy storage system would be required if this energy was employed to heat the digesters, which require heat during the whole period. In this case, a zero biogas self-consumption would be possible. Besides, the surplus heat generated could be used in other process, as, for instance, feedstock hygienisation, digestate drying or be sold to a neighbor industry or heat district.

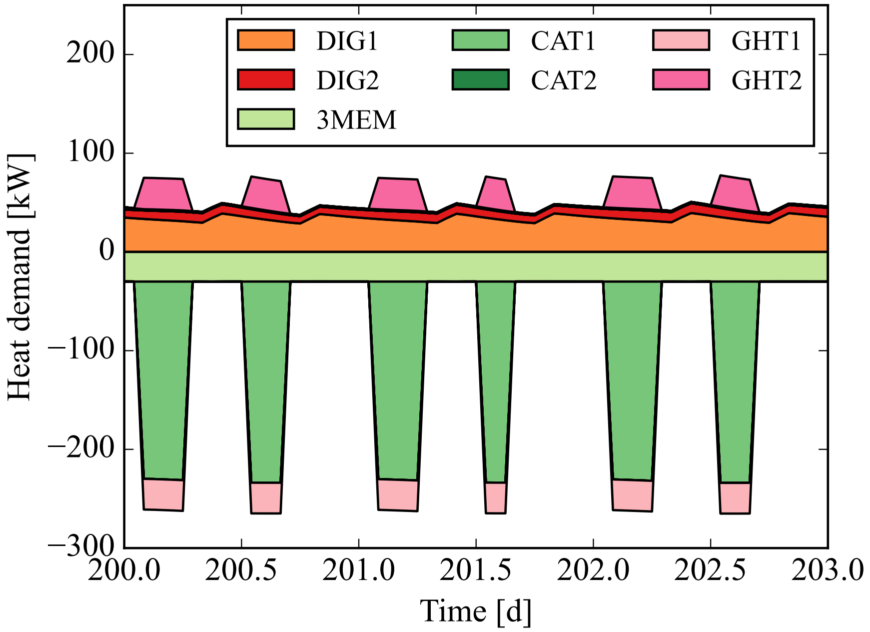

Figure 6.38: Heating utility demand on 20, 21 and 22 July in the whole plant (biomethane and P2G) with intermittent operation of the P2G plant. Positive values indicate a heat consumption, and negative values heat production. 3MEM values correspond to half of the calculated power of the upgrading unit's heat exchanger.

It should also be noted that these considerations are based in an intermittent operation that only reflects the solar energy generation. The availability of excess electricity depends on other factors as, for instance, power consumption and generation from other sources. With an increasing fraction of renewable sources in the energy mix, wind speed might also influence on this energy balance as well. Possibly, the P2G would actually be able to operate for more hours a day, thus reducing the stand-by intervals. In this case, the heat generation would be better distributed, and less thermal storage would be required. Therefore, as a continuation of this work, it would be interesting to use a more complex approach to define P2G plant's operation schedule.

Table 6.8: Total energy demand or production during the three-days period in February and in July for an intermittent operation of the P2G plant. Positive values refer to a heat demand and negative ones to heat production.

Unit	Heat demand [MJ]	
	15-17 February	20-22 July
DIG1	+ 8946.3	+ 8794.3
DIG2	+ 6244.7	+ 2279.4
3MEM	- 8248.2	- 7785.2
CAT1	- 11109.5	- 18434.2
CAT2	+ 57.2	+ 344.3
GHT1	- 1567.0	- 2835.6
GHT2	+ 1603.2	+ 2901.0
Net demand	**- 4073.3**	**- 14733.0**

6.3 Conclusions

In this chapter, a number of different study cases could be evaluated using the models developed during this thesis. Besides, they were integrated with a catalytic methanation model produced in a previous PhD thesis carried out in LaTEP. The digester model could be applied to evaluate the structural thermal losses in different climates, which can be useful in designing new biogas plants at different locations. In addition, it could be also useful in training the staff of these installations, as it is possible to study different parameters that affect the process. Integrating the biomethane plant to a P2G installation allowed evaluating the additional methane that would be produced from this multi-energy platform and assessing possible synergies between these processes.

CHAPTER 7

CONCLUSIONS AND PERSPECTIVES

The objective of this work was to develop computational models to dynamically simulate biomethane production in a biogas plant combined with a catalytic methanation reactor within a Power-to-Gas (P2G) approach. The produced gas was designed to meet the grid injection specifications, specifically those of the French natural gas grid.

The analysis on the technology allowed defining the typical biomethane plant as: an agricultural biogas plant, equipped with CSTR digesters and membrane separator. Therefore, this digester and this upgrading unit were modeled in this thesis.

The literature review indicated that ADM1 is the mainstream approach for describing the bioreactions in AD systems. Thus, a modified version of ADM1, more suitable for agricultural systems, and a comprehensive thermal model were combined into the digester mathematical description. This model was validated against experimental data, showing good agreement in predicting biogas production and thermal behavior. However, the kinetic model had limitations in representing dynamic biogas production under strong feedstock variations. This means that further advancements in AD kinetic modeling is still required to fully capture the complexity of anaerobic digestion systems.

The biogas cleaning and upgrading stages were modeled using simpler approaches. As upgrading unit, a three-stage membrane separator was used. Although a quite basic model was adopted in this permeator, it managed to fairly reproduce the results obtained by a much more complex approach from the literature.

Then, several simulations including these biomethane plant units and a catalytic methanation reactor model, which was previously developed in LaTEP, were carried out. These studies showed that this multi-energy platform would be able to store excess energy from the grid, as the start-up uf the methanation reactors could be done within a few minuts. Besides, they revealed this system could be subject of seasonal variations due to variabilities in renewable energy production.

However, many other possibilities were left unexplored. For instance, it would be interesting to evaluate the viability of H_2 storage to reduce the intermittency of the methanation reactors. Integrating an electrolyzer into the simulation environment would possibly give more insights in the capabilities of such system to operate under dynamic conditions. Also, the design of the plant units (e.g. dimensions, operating conditions) and their operation (e.g. feeding schedule, gas storage level) could be optimized to minimize the installation's environmental footprint or to maximize its economic performance. The answers to these questions will hopefully be found in the following years.

Appendices

APPENDIX A

GEOMETRY RELATIONSHIPS

A.1 Spherical cap

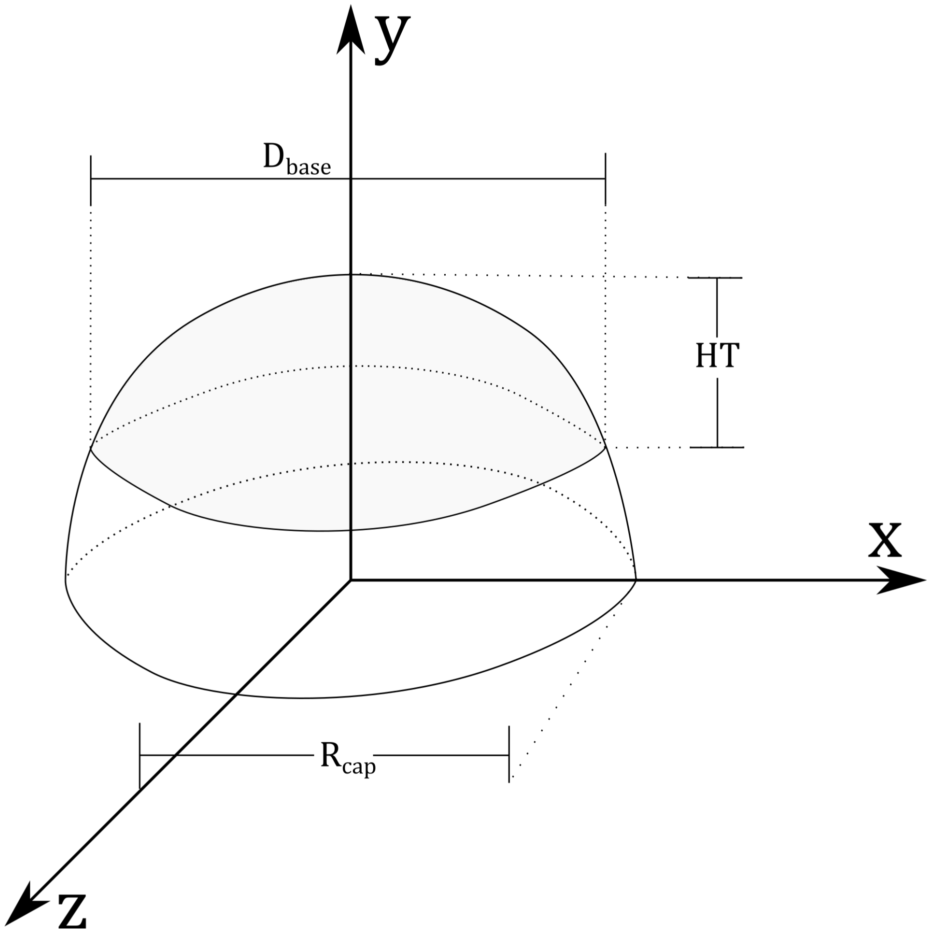

Figure A.1: Geometrical representation of a spherical cap.

A.1.1 Radius

$$R_{cap} = \frac{HT^2 + \left(\frac{D}{2}\right)}{2HT} \tag{A.1}$$

A.1.2 Volume

$$V_{cap} = \frac{\pi HT}{6}\left(3\left(\frac{D_{base}}{2}\right)^2 + HT^2\right) \tag{A.2}$$

A.2 Cylinder

A.2.1 Lateral surface

$$A_{lat,cyl} = \pi DHT \tag{A.3}$$

A.3 Disk

A.3.1 Perimeter

$$Per_{disk} = \pi D \tag{A.4}$$

A.3.2 Surface

$$A_{disk} = \pi\frac{D^2}{4} \tag{A.5}$$

APPENDIX B

HEAT TRANSFER CORRELATIONS

The heat transfer flow rates by convection, either natural or forced, were estimated through the use of empirical correlations on Nu, which was used to estimate the heat transfer coefficient, h (Eq. B.1).

$$Nu = \frac{h\,L}{\lambda} \tag{B.1}$$

These correlations are calculated using other dimensionless numbers: Re (Eq. B.2), Pr (Eq. B.3), Gr (Eq. B.4), Gr_m (Eq. B.5, Ra (Eq. B.6), Sh (Eq. B.7), Sc (Eq. B.8).

$$Re = \frac{\rho\,u\,L}{\mu} \tag{B.2}$$

$$Pr = \frac{\mu\,C_P}{\lambda} \tag{B.3}$$

$$Gr = \frac{\beta L^3 |\Delta T|}{\nu^2} \tag{B.4}$$

$$Gr_m = \frac{g\,(\rho_s - \rho_{bulk})\,L^3}{\rho \nu^2} \tag{B.5}$$

$$Ra = Gr\;Pr \tag{B.6}$$

$$Sh = \frac{kL}{D_{AB}} \tag{B.7}$$

$$Sc = \frac{\nu}{D_{AB}} \tag{B.8}$$

B.1 Natural convection

B.1.1 Horizontal plate

For natural convection over a hot plate or under a cold one, Eq. B.9 was used. Alternatively, to describe the heat transfer over a cold plate or under a hot one, Eq. B.10 was employed [142].

$$Nu = \begin{cases} 0.54Ra^{1/4}, & 10^4 \leq Ra < 10^7 \\ 0.15Ra^{1/3}, & 10^7 \leq Ra < 10^{11} \end{cases} \tag{B.9}$$

$$Nu = 0.27Ra^{1/4},\ 10^5 \leq Ra \leq 10^{10} \tag{B.10}$$

B.1.2 Vertical plate

For natural convection in contact with a vertical plate, the equation of Churchill and Chu [143] was used (Eq. B.11).

$$Nu = \left[0.825 + \frac{0.387Ra^{1/6}}{\left[1 + \left(\frac{0.492}{Pr}\right)^{9/16}\right]^{8/27}}\right]^2 \tag{B.11}$$

B.1.3 Horizontal tube

Natural convection over a horizontal tube was described using the correlation of Churchill and Chu [144] (Eq. B.12).

$$Nu = \left(0.6 + \frac{0.387Ra^{1/6}}{\left(1 + \left(0.559/Pr\right)^{9/16}\right)^{8/27}}\right)^2 \tag{B.12}$$

B.2 Forced convection

B.2.1 Cylinder in cross flow

The forced convection with a cylinder in cross flow was calculated using the equation of Churchill and Bernstein [145] (Eq. B.13).

$$Nu = 0.3 + \frac{0.62 Re^{1/2} Pr^{1/3}}{\left[1 + \left(\frac{0.4}{Pr}\right)^{2/3}\right]^{1/4}} \left[1 + \left(\frac{Re}{282\,000}\right)^{5/8}\right]^{4/5} \tag{B.13}$$

B.2.2 Flat plate in parallel flow

Nu was calculated using Eq. B.14 [146].

$$Nu = \begin{cases} 0.664 Re^{1/2} Pr^{1/3}, & Re < 5\ 10^5 \\ \left(0.0037 Re^{4/5} - 871\right) Pr^{1/3}, & Re \geq 5\ 10^5 \end{cases} \tag{B.14}$$

B.2.3 Internal flow in circular tubes

Nu was calculated according to the flow regime: laminar regime ($Re < 2300$, Eq. B.15) [147] and turbulent regime ($Re \geq 2300$, Eq. B.16) [148].

$$Nu = 3.66 \tag{B.15}$$

$$Nu = 0.0023 Re^{0.8} Pr^{1/3} \tag{B.16}$$

B.2.4 Turbulent flow in circular tubes

Another correlation to evaluate Nu in internal flow in tubes is the Gnielinski's equation (Eq. B.17), which is valid over a large range of Re [149]. The friction factor, f, can be estimated for smooth tubes using Petukhov's equation (Eq. B.18) [150].

$$Nu = \frac{\left(f/8\right)\left(Re - 1000\right)Pr}{1 + 12.7\left(f/8\right)^{1/2}\left(Pr^{2/3} - 1\right)} \tag{B.17}$$

$$f = \left(0.79ln(Re) - 1.64\right)^{-2} \tag{B.18}$$

REFERENCES

[1] Eurostat, *Shedding light on energy in the eu - 2022 interactive edition*, [Online; accessed 2022-08-31], May 5, 2022.

[2] European Commission. Directorate General for Communication., *European green deal: delivering on our targets.* LU: Publications Office, 2021.

[3] European Environment Agency (EEA), *Share of energy consumption from renewable sources in Europe*, Mar. 2024.

[4] Eurostat, *Statistics | Eurostat*, Apr. 2024.

[5] A. Santecchia, R. Castro-Amoedo, T.-V. Nguyen, I. Kantor, P. Stadler, and F. Maréchal, "The critical role of electricity storage for a clean and renewable European economy," *Energy & Environmental Science*, vol. 16, no. 11, pp. 5350–5370, 2023.

[6] M. Calero, V. Godoy, C. G. Heras, E. Lozano, S. Arjandas, and M. A. Martín-Lara, "Current state of biogas and biomethane production and its implications for spain," *Sustainable Energy & Fuels*, vol. 7, no. 15, pp. 3584–3602, 2023.

[7] ADEME, "Chiffres clés du parc d'unités de méthanisation en France au 1er janvier 2022," ADEME, Synthèse d'expertise, May 2022.

[8] GRTgaz, S. des énergies renouvelabels (SER), GRDF, SPEGNN, and Teréga, *Panorama des gaz renouvelables en 2023*, 2024.

[9] M. Beil and W. Beyrich, "Biogas upgrading to biomethane," in *The Biogas Handbook*, Elsevier, 2013, pp. 342–377, ISBN: 978-0-85709-498-8.

[10] B. Wu, X. Zhang, D. Shang, D. Bao, S. Zhang, and T. Zheng, "Energetic-environmental-economic assessment of the biogas system with three utilization pathways: Combined heat and power, biomethane and fuel cell," *Bioresource Technology*, vol. 214, pp. 722–728, Aug. 2016.

[11] N. Malet, S. Pellerin, R. Girault, and T. Nesme, "Does anaerobic digestion really help to reduce greenhouse gas emissions? A nuanced case study based on 30 cogeneration plants in France," *Journal of Cleaner Production*, vol. 384, p. 135 578, Jan. 2023.

[12] M. L. Parisi, S. Maranghi, R. Basosi, and A. Sinicropi, "Life Cycle Inventories datasets for future European electricity mix scenarios," *Data in Brief*, vol. 30, p. 105 499, Jun. 2020.

[13] M. Sterner and M. Specht, "Power-to-Gas and Power-to-X—The History and Results of Developing a New Storage Concept," *Energies*, vol. 14, no. 20, p. 6594, Oct. 2021.

[14] S. Group, *Pau-Lescar Biofactory: The first wastewater treatment plant to recover CO2 from sludge methanation - SUEZ Group*, 2021.

[15] GRTgaz, *Contrat relatif au raccordement d'une installation de production de biométhane et d'injection de biométhane dans le réseau de transport de gaz naturel*, 2019.

[16] D. Deublein and A. Steinhauser, Eds., *Biogas from Waste and Renewable Resources: An Introduction*, 1st ed. Wiley, Feb. 2008, ISBN: 978-3-527-62170-5.

[17] M. H. Gerardi, *The Microbiology of Anaerobic Digesters*, 1st ed. Wiley, Aug. 2003, ISBN: 978-0-471-20693-4 978-0-471-46896-7.

[18] S. Weinrich and M. Nelles, *Basics of Anaerobic Digestion - Biochemical Conversion and Process Modelling (DBFZ-Report, 40)*. Leipzig: DBFZ, Mar. 2021, ISBN: 978-3-946629-72-6.

[19] A. Kunz, R. L. R. Steinmetz, and A. C. d. Amaral, *Fundamentals of anaerobic digestion, biogas purification, use and treatment of digestate* (Embrapa Suinos e Aves), 2nd ed. Concordia: Sbera: Embrapa Suinos e Aves, Mar. 2022, ISBN: 978-65-88-155-03-5.

[20] D. P. Van, T. Fujiwara, B. Leu Tho, P. P. Song Toan, and G. Hoang Minh, "A review of anaerobic digestion systems for biodegradable waste: Configurations, operating parameters, and current trends," *Environmental Engineering Research*, vol. 25, no. 1, pp. 1–17, Mar. 2019.

[21] C. A. d. Lemos Chernicharo, *Anaerobic reactors* (Biological wastewater treatment series 4). London: IWA Publ. [u.a.], 2007, ISBN: 978-1-84339-164-7.

[22] A. Etienne, *Panorama des unités de méthanisation agricoles en région Hauts-de-France (au 31 octobre 2020)*, Nov. 2020.

[23] A. Wellinger, J. D. Murphy, and D. Baxter, Eds., *The biogas handbook: science, production and applications* (Woodhead publishing series in energy 52). Oxford: Woodhead Publ, 2013, ISBN: 978-0-85709-498-8.

[24] X. Y. Chen, H. Vinh-Thang, A. A. Ramirez, D. Rodrigue, and S. Kaliaguine, "Membrane gas separation technologies for biogas upgrading," *RSC Advances*, vol. 5, no. 31, pp. 24 399–24 448, 2015.

[25] A. Petersson, “Biogas cleaning,” in *The Biogas Handbook*, Elsevier, 2013, pp. 329–341, ISBN: 978-0-85709-498-8.

[26] M. R. Atelge *et al.*, “A Critical Overview of the State-of-the-Art Methods for Biogas Purification and Utilization Processes,” *Sustainability*, vol. 13, no. 20, p. 11 515, Oct. 2021.

[27] L. Deng, Y. Liu, and W. Wang, *Biogas Technology*. Singapore: Springer Singapore, 2020, ISBN: 9789811549397 9789811549403.

[28] F. M. Baena-Moreno, L. M. Gallego, F. Vega, and B. Navarrete, “Cryogenic techniques: An innovative approach for biogas upgrading,” in *Emerging Technologies and Biological Systems for Biogas Upgrading*, Elsevier, 2021, pp. 159–186, ISBN: 978-0-12-822808-1.

[29] J. Kube, “Energetic Optimization of the Three-Stage Gas Permeation Process for the Upgrading of Biogas,” *Chemical Engineering & Technology*, vol. 43, no. 1, pp. 29–38, Jan. 2020.

[30] F. M. Baena-Moreno, E. Le Saché, L. Pastor-Pérez, and T. R. Reina, “Membrane-based technologies for biogas upgrading: A review,” *Environmental Chemistry Letters*, vol. 18, no. 5, pp. 1649–1658, Sep. 2020.

[31] GRDF, R-GDS, REGAZ Bordeaux, GRTgaz, and Terega, *Retour d’expérience inter-opérateurs sur l’injection de biométhane Année 2021*, 2022.

[32] S. Emebu, J. Pecha, and D. Janáčová, “Review on anaerobic digestion models: Model classification & elaboration of process phenomena,” *Renewable and Sustainable Energy Reviews*, vol. 160, p. 112 288, May 2022.

[33] D. Batstone *et al.*, “The iwa anaerobic digestion model no 1 (adm1),” *Water Science and Technology*, vol. 45, no. 10, pp. 65–73, May 1, 2002.

[34] R. Mo, W. Guo, D. Batstone, J. Makinia, and Y. Li, “Modifications to the anaerobic digestion model no. 1 (adm1) for enhanced understanding and application of the anaerobic treatment processes – a comprehensive review,” *Water Research*, vol. 244, p. 120 504, Oct. 2023.

[35] H. Ozgun, “Anaerobic digestion model no. 1 (adm1) for mathematical modeling of full-scale sludge digester performance in a municipal wastewater treatment plant,” *Biodegradation*, vol. 30, no. 1, pp. 27–36, Feb. 2019.

[36] F. Calise, F. L. Cappiello, M. Dentice d’Accadia, A. Infante, and M. Vicidomini, “Modeling of the anaerobic digestion of organic wastes: Integration of heat transfer and biochemical aspects,” *Energies*, vol. 13, no. 11, p. 2702, May 28, 2020.

[37] K. Koch, M. Lübken, T. Gehring, M. Wichern, and H. Horn, “Biogas from grass silage – measurements and modeling with adm1,” *Bioresource Technology*, vol. 101, no. 21, pp. 8158–8165, Nov. 2010.

[38] S. Weinrich, E. Mauky, T. Schmidt, C. Krebs, J. Liebetrau, and M. Nelles, “Systematic simplification of the anaerobic digestion model no. 1 (adm1) – laboratory experiments and model application,” *Bioresource Technology*, vol. 333, p. 125 104, Aug. 2021.

[39] S. Weinrich and M. Nelles, “Systematic simplification of the anaerobic digestion model no. 1 (adm1) – model development and stoichiometric analysis,” *Bioresource Technology*, vol. 333, p. 125 124, Aug. 2021.

[40] I. Angelidaki, L. Ellegaard, and B. K. Ahring, “A mathematical model for dynamic simulation of anaerobic digestion of complex substrates: Focusing on ammonia inhibition,” *Biotechnology and Bioengineering*, vol. 42, no. 2, pp. 159–166, Jun. 20, 1993.

[41] I. Angelidaki, L. Ellegaard, and B. K. Ahring, “A comprehensive model of anaerobic bioconversion of complex substrates to biogas,” *Biotechnology and Bioengineering*, vol. 63, no. 3, pp. 363–372, May 5, 1999.

[42] A. Kovalovszki, M. Alvarado-Morales, I. A. Fotidis, and I. Angelidaki, “A systematic methodology to extend the applicability of a bioconversion model for the simulation of various co-digestion scenarios,” *Bioresource Technology*, vol. 235, pp. 157–166, Jul. 2017.

[43] G. Lovato *et al.*, “In-situ biogas upgrading process: Modeling and simulations aspects,” *Bioresource Technology*, vol. 245, pp. 332–341, Dec. 2017.

[44] T. Kegl and A. Kovač Kralj, “An enhanced anaerobic digestion BioModel calibrated by parameters optimization based on measured biogas plant data,” *Fuel*, vol. 312, p. 122 984, Mar. 2022.

[45] D. J. Batstone and I. W. Association, Eds., *Anaerobic digestion model no. 1: (ADM1)* (Scientific and technical report / IWA 13), 1. publ. London: IWA Publ, 2002, ISBN: 978-1-900222-78-5.

[46] ADEME, *Chaleur issue de la méthanisation : De réelles opportunités : Guide pratique*, [Online; accessed 2023-09-19], May 2016.

[47] M. Avila-Lopez, C. Robles-Rodriguez, L. Tiruta-Barna, and A. Ahmadi, “Toward thermal autarky for large-scale biogas plants: Dynamic energy modeling for energy efficiency in anaerobic digesters with enhanced multimembrane gasholders,” *Fuel*, p. 126 978, Dec. 2022.

[48] T. Teleszewski and M. Żukowski, “Analysis of heat loss of a biogas anaerobic digester in weather conditions in poland,” *Journal of Ecological Engineering*, vol. 19, no. 4, pp. 242–250, Jul. 1, 2018.

[49] S. Vilms Pedersen, J. Martí-Herrero, A. Singh, S. Sommer, and S. Hafner, “Management and design of biogas digesters: A non-calibrated heat transfer model,” *Bioresource Technology*, vol. 296, p. 122 264, Jan. 2020.

[50] R. Hreiz, N. Adouani, Y. Jannot, and M.-N. Pons, “Modeling and simulation of heat transfer phenomena in a semi-buried anaerobic digester,” *Chemical Engineering Research and Design*, vol. 119, pp. 101–116, Mar. 2017.

[51] F. Calise, F. L. Cappiello, L. Cimmino, M. Dentice d’Accadia, and M. Vicidomini, “Dynamic analysis and investigation of the thermal transient effects in a cstr reactor producing biogas,” *Energy*, vol. 263, p. 126 010, Jan. 2023.

[52] A. Ahmadi, M. Avila, and L. Barna, “Pathways for the thermally optimal design and practice of anaerobic digestion in large-scale biogas plants: Heat transfer modeling and energy analysis,” *Chemical Engineering Research and Design*, vol. 197, pp. 884–907, Sep. 2023.

[53] F. Goffart De Roeck, A. Buchmayr, J. Gripekoven, J. Mertens, and J. Dewulf, “Comparative life cycle assessment of power-to-methane pathways: Process simulation of biological and catalytic biogas methanation,” *Journal of Cleaner Production*, vol. 380, p. 135 033, Dec. 2022.

[54] L. Janke, F. Ruoss, A. Hahn, S. Weinrich, and A. Nordberg, “Modelling synthetic methane production for decarbonising public transport buses: A techno-economic assessment of an integrated power-to-gas concept for urban biogas plants,” *Energy Conversion and Management*, vol. 259, p. 115 574, May 2022.

[55] F. Calise, F. L. Cappiello, L. Cimmino, M. Dentice d’Accadia, and M. Vicidomini, “Dynamic simulation and thermoeconomic analysis of a power to gas system,” *Renewable and Sustainable Energy Reviews*, vol. 187, p. 113 759, Nov. 2023.

[56] F. Calise, F. L. Cappiello, L. Cimmino, M. Dentice d’Accadia, and M. Vicidomini, “Dynamic analysis and thermoeconomic optimization of a Power-to-Gas system driven by renewables,” *Energy Conversion and Management*, vol. 313, p. 118 647, Aug. 2024.

[57] E. Giglio, R. Pirone, and S. Bensaid, “Dynamic modelling of methanation reactors during start-up and regulation in intermittent power-to-gas applications,” *Renewable Energy*, vol. 170, pp. 1040–1051, Jun. 2021.

[58] R. Hakawati, B. M. Smyth, G. McCullough, F. De Rosa, and D. Rooney, “What is the most energy efficient route for biogas utilization: Heat, electricity or transport?” *Applied Energy*, vol. 206, pp. 1076–1087, Nov. 2017.

[59] L. Lombardi and G. Francini, “Techno-economic and environmental assessment of the main biogas upgrading technologies,” *Renewable Energy*, vol. 156, pp. 440–458, Aug. 2020.

[60] I. Dimitriou, P. García-Gutiérrez, R. H. Elder, R. M. Cuéllar-Franca, A. Azapagic, and R. W. K. Allen, “Carbon dioxide utilisation for production of transport fuels: Process and economic analysis,” *Energy & Environmental Science*, vol. 8, no. 6, pp. 1775–1789, 2015.

[61] M. Erol, H. Haykiri-Acma, and S. Küçükbayrak, “Calorific value estimation of biomass from their proximate analyses data,” *Renewable Energy*, vol. 35, no. 1, pp. 170–173, Jan. 2010.

[62] TNO Biobased and Circular Technologies, “Phyllis 2: The Open Access Database for Biomass Properties,” TNO Biobased and Circular Technologies, Tech. Rep.

[63] Ecoinvent, *System Models*.

[64] H. W. Brendeløkken, “Upgrading technologies for biogas production plants. Overview and life cycle cost analysis of available technologies,” Master’s Theses in Technology and Safety in the High North, UiT The Arctic University of Norway, Jun. 2016.

[65] D. Dressler, A. Loewen, and M. Nelles, “Life cycle assessment of the supply and use of bioenergy: Impact of regional factors on biogas production,” *The International Journal of Life Cycle Assessment*, vol. 17, no. 9, pp. 1104–1115, Nov. 2012.

[66] J. Bacenetti and M. Fiala, “Carbon footprint of electricity from anaerobic digestion plants in Italy,” *Environmental Engineering and Management Journal*, vol. 14, no. 7, pp. 1495–1502, 2015.

[67] G. Wernet, C. Bauer, B. Steubing, J. Reinhard, E. Moreno-Ruiz, and B. Weidema, “The ecoinvent database version 3 (part I): Overview and methodology,” *The International Journal of Life Cycle Assessment*, vol. 21, no. 9, pp. 1218–1230, Sep. 2016.

[68] ISPRA, “Indicatori di efficienza e decarbonizzazione del sistema energetico nazionale e del settore elettrico,” Istituto Superiore per la Protezione e la Ricerca Ambientale (ISPRA), Tech. Rep. 363/2022, 2022.

[69] ISPRA, "Italian Greenhouse Gas Inventory 1990-2020. National Inventory Report 2022," Italian Institute for Environmental Protection and Research (ISPRA), Tech. Rep. 360/2022, 2022.

[70] Intergovernmental Panel On Climate Change, *Climate Change 2021 – The Physical Science Basis: Working Group I Contribution to the Sixth Assessment Report of the Intergovernmental Panel on Climate Change*, 1st ed. Cambridge University Press, Jul. 2023, ISBN: 978-1-00-915789-6.

[71] K. Shanmugam, M. Tysklind, and V. K. Upadhyayula, "Use of Liquefied Biomethane (LBM) as a Vehicle Fuel for Road Freight Transportation: A Case Study Evaluating Environmental Performance of Using LBM for Operation of Tractor Trailers," *Procedia CIRP*, vol. 69, pp. 517–522, 2018.

[72] M. E. Stettler *et al.*, "Review of Well-to-Wheel lifecycle emissions of liquefied natural gas heavy goods vehicles," *Applied Energy*, vol. 333, p. 120 511, Mar. 2023.

[73] G. Blengini, E. Brizio, M. Cibrario, and G. Genon, "LCA of bioenergy chains in Piedmont (Italy): A case study to support public decision makers towards sustainability," *Resources, Conservation and Recycling*, vol. 57, pp. 36–47, Dec. 2011.

[74] European Environment Agency, *Greenhouse gas emission intensity of electricity generation*, Data Visualization, Jun. 2024.

[75] S. Weinrich and M. Nelles, "Systematic simplification of the Anaerobic Digestion Model No. 1 (ADM1) – Model development and stoichiometric analysis," *Bioresource Technology*, vol. 333, p. 125 124, Aug. 2021.

[76] L. Pokorna-Krayzelova, K. E. Mampaey, T. P. Vannecke, J. Bartacek, P. Jenicek, and E. I. Volcke, "Model-based optimization of microaeration for biogas desulfurization in uasb reactors," *Biochemical Engineering Journal*, vol. 125, pp. 171–179, Sep. 2017.

[77] K. Waszkielis, I. Białobrzewski, and K. Bułkowska, "Application of anaerobic digestion model no. 1 for simulating fermentation of maize silage, pig manure, cattle manure and digestate in the full-scale biogas plant," *Fuel*, vol. 317, p. 123 491, Jun. 2022.

[78] A. Kovalovszki, L. Treu, L. Ellegaard, G. Luo, and I. Angelidaki, "Modeling temperature response in bioenergy production: Novel solution to a common challenge of anaerobic digestion," *Applied Energy*, vol. 263, p. 114 646, Apr. 2020.

[79] L. Pokorna-Krayzelova, K. E. Mampaey, T. P. Vannecke, J. Bartacek, P. Jenicek, and E. I. Volcke, "Model-based optimization of microaeration for biogas desulfu-

rization in UASB reactors," *Biochemical Engineering Journal*, vol. 125, pp. 171–179, Sep. 2017.

[80] H. P. Vu *et al.*, "Hydrogen sulphide management in anaerobic digestion: A critical review on input control, process regulation, and post-treatment," *Bioresource Technology*, vol. 346, p. 126 634, Feb. 2022.

[81] V. Fedorovich, P. Lens, and S. Kalyuzhnyi, "Extension of Anaerobic Digestion Model No. 1 with Processes of Sulfate Reduction," *Applied Biochemistry and Biotechnology*, vol. 109, no. 1-3, pp. 33–46, 2003.

[82] J. Kim and C. Lee, "Response of a continuous anaerobic digester to temperature transitions: A critical range for restructuring the microbial community structure and function," *Water Research*, vol. 89, pp. 241–251, Feb. 2016.

[83] E. Nie, P. He, H. Zhang, L. Hao, L. Shao, and F. Lü, "How does temperature regulate anaerobic digestion?" *Renewable and Sustainable Energy Reviews*, vol. 150, p. 111 453, Oct. 2021.

[84] A. Veeken and B. Hamelers, "Effect of temperature on hydrolysis rates of selected biowaste components," *Bioresource Technology*, vol. 69, no. 3, pp. 249–254, Sep. 1999.

[85] A. Kovalovszki, L. Treu, L. Ellegaard, G. Luo, and I. Angelidaki, "Modeling temperature response in bioenergy production: Novel solution to a common challenge of anaerobic digestion," *Applied Energy*, vol. 263, p. 114 646, Apr. 2020.

[86] A. Kunz, R. L. R. Steinmetz, and d. A. C. Amaral, *Fundamentals of anaerobic digestion, biogas purification, use and treatment of digestate* (Embrapa Suinos e Aves), 2nd ed. Concordia: Sbera: Embrapa Suinos e Aves, Mar. 25, 2022, ISBN: 978-65-88-155-03-5.

[87] A. Kovalovszki, M. Alvarado-Morales, I. A. Fotidis, and I. Angelidaki, "A systematic methodology to extend the applicability of a bioconversion model for the simulation of various co-digestion scenarios," *Bioresource Technology*, vol. 235, pp. 157–166, Jul. 2017.

[88] G. Lovato *et al.*, "In-situ biogas upgrading process: Modeling and simulations aspects," *Bioresource Technology*, vol. 245, pp. 332–341, Dec. 2017.

[89] A. Lemmer, H.-J. Naegele, and J. Sondermann, "How efficient are agitators in biogas digesters? determination of the efficiency of submersible motor mixers and incline agitators by measuring nutrient distribution in full-scale agricultural biogas digesters," *Energies*, vol. 6, no. 12, pp. 6255–6273, Dec. 2, 2013.

[90] F. Garcia-Ochoa and E. Gomez, "Theoretical prediction of gas–liquid mass transfer coefficient, specific area and hold-up in sparged stirred tanks," *Chemical Engineering Science*, vol. 59, no. 12, pp. 2489–2501, Jun. 2004.

[91] W. Merkel and K. Krauth, "Mass transfer of carbon dioxide in anaerobic reactors under dynamic substrate loading conditions," *Water Research*, vol. 33, no. 9, pp. 2011–2020, Jun. 1999.

[92] A. Pauss, G. Andre, M. Perrier, and S. R. Guiot, "Liquid-to-gas mass transfer in anaerobic processes: Inevitable transfer limitations of methane and hydrogen in the biomethanation process," *Applied and Environmental Microbiology*, vol. 56, no. 6, pp. 1636–1644, Jun. 1990.

[93] F. P. Incropera, D. P. DeWitt, T. L. Bergman, and A. S. Lavine, *Fundamentals of Heat and Mass Transfer*, 6th edition. New York: John Wiley & Sons Ltd, 2007, OCLC: 868311388, ISBN: 978-0-470-05554-0.

[94] M. Abu-Hamdiyyah and A. Shehabuddin, "Transfer enthalpies and entropies of amino acids from water to urea solutions," *Journal of Chemical & Engineering Data*, vol. 27, no. 1, pp. 74–76, Jan. 1982.

[95] W. M. Haynes, *CRC handbook of chemistry and physics: a ready-reference book of chemical and physical data.* 2014, OCLC: 882266963, ISBN: 978-1-4822-0867-2.

[96] R. H. Perry and D. W. Green, Eds., *Perry's chemical engineers' handbook*, 8th ed. New York: McGraw-Hill, 2008, OCLC: ocm72470708, ISBN: 978-0-07-142294-9.

[97] M. Popovic, "Thermodynamic properties of microorganisms: Determination and analysis of enthalpy, entropy, and gibbs free energy of biomass, cells and colonies of 32 microorganism species," *Heliyon*, vol. 5, no. 6, e01950, Jun. 2019.

[98] F. Rodante, "Thermodynamics of the "standard" α-amino acids in water at 25 °c," *Thermochimica Acta*, vol. 149, pp. 157–171, Sep. 1989.

[99] K. Zhang *et al.*, "Dynamic modeling and coordinated multi-energy management for a sustainable biogas-dominated energy hub," *Energy*, vol. 220, p. 119 640, Apr. 2021.

[100] J. M. Cabeza-Lainez and J. A. Pulido-Arcas, "New configuration factors for curved surfaces," *Journal of Quantitative Spectroscopy and Radiative Transfer*, vol. 117, pp. 71–80, Mar. 2013.

[101] W. C. Swinbank, "Long-wave radiation from clear skies," *Quarterly Journal of the Royal Meteorological Society*, vol. 89, no. 381, pp. 339–348, 1963. eprint: `https:`

`//rmets.onlinelibrary.wiley.com/doi/pdf/10.1002/qj.49708938105`.

[102] C. K. Pandey and A. Katiyar, “A note on diffuse solar radiation on a tilted surface,” *Energy*, vol. 34, no. 11, pp. 1764–1769, Nov. 2009.

[103] G. Evola, N. Le Pierrès, F. Boudehenn, and P. Papillon, “Proposal and validation of a model for the dynamic simulation of a solar-assisted single-stage libr/water absorption chiller,” *International Journal of Refrigeration*, vol. 36, no. 3, pp. 1015–1028, May 2013.

[104] ISO/TC 163/SC2, *Iso 13370:2017 thermal performance of buildings heat transfer via the ground - calculation methods*, 2017.

[105] T. H. Sørensen, N. Cruys-Bagger, K. Borch, and P. Westh, “Free energy diagram for the heterogeneous enzymatic hydrolysis of glycosidic bonds in cellulose,” *Journal of Biological Chemistry*, vol. 290, no. 36, pp. 22 203–22 211, Sep. 2015.

[106] H.-J. Hinz, Ed., *Thermodynamic Data for Biochemistry and Biotechnology*. Cham: Springer International Publishing, 1986, OCLC: 1159716974, ISBN: 978-3-642-71114-5.

[107] G. H. Charbonnet and W. S. Singleton, “Thermal properties of fats and oils. vi. heat capacity, heats of fusion and transition, and entropy of trilaurin, trimyristin, tripalmitin, and tristearin,” *Journal of the American Oil Chemists Society*, vol. 24, pp. 140–142, 1947.

[108] F. Rodante, “Thermodynamics of the “standard” α-amino acids in water at 25° C,” *Thermochimica Acta*, vol. 149, pp. 157–171, Sep. 1989.

[109] M. Abu-Hamdiyyah and A. Shehabuddin, “Transfer enthalpies and entropies of amino acids from water to urea solutions,” *Journal of Chemical & Engineering Data*, vol. 27, no. 1, pp. 74–76, Jan. 1982.

[110] M. Stur, M. Pohl, C. Krebs, and E. Mauky, “Characterisation of biogas storages: Influences and comparison of methods,” *Agricultural Engineering*, Bd. 77 Nr. 1 (2022), Mar. 2022, Publisher: LANDTECHNIK.

[111] *Zorg Biogas GmbH | Catalogue | Gasholders*.

[112] J. Kube, “Management of Gas Storages in Biogas Plants,” *Chemical Engineering & Technology*, vol. 41, no. 4, pp. 702–710, Apr. 2018.

[113] C. F. Colebrook, “TURBULENT FLOW IN PIPES, WITH PARTICULAR REFERENCE TO THE TRANSITION REGION BETWEEN THE SMOOTH AND

ROUGH PIPE LAWS.," *Journal of the Institution of Civil Engineers*, vol. 11, no. 4, pp. 133–156, Feb. 1939.

[114] W. B. Cory, "Fan selection," in *Fans and Ventilation*, Elsevier, 2005, pp. 309–318, ISBN: 978-0-08-044626-4.

[115] P. N. Brown, A. C. Hindmarsh, and L. R. Petzold, "Using Krylov Methods in the Solution of Large-Scale Differential-Algebraic Systems," *SIAM Journal on Scientific Computing*, vol. 15, no. 6, pp. 1467–1488, Nov. 1994.

[116] S. Menardo, G. Airoldi, V. Cacciatore, and P. Balsari, "Potential biogas and methane yield of maize stover fractions and evaluation of some possible stover harvest chains," *Biosystems Engineering*, vol. 129, pp. 352–359, Jan. 2015.

[117] H. Fisgativa, B. Zennaro, C. Charnier, C. Richard, G. Accarion, and F. Béline, "Comprehensive determination of input state variables dataset required for anaerobic digestion modelling (adm1) based on characterisation of organic substrates," *Data in Brief*, vol. 29, p. 105 212, Apr. 2020.

[118] C. Herrmann, C. Idler, and M. Heiermann, "Biogas crops grown in energy crop rotations: Linking chemical composition and methane production characteristics," *Bioresource Technology*, vol. 206, pp. 23–35, Apr. 2016.

[119] N. de Lucena Costa, C. Ramalho Townsend, J. Avelar Magalhães, and R. Gomes de Araujo Pereira, "Utilização de subprodutos do arroz na alimentação animal," Embrapa, Tech. Rep., Dec. 2005, pp. 1–5.

[120] L. R. Sarker, K. Mri, and R. Mm, "Ensiling of wet rice straw using biogas slurry and molasses in monsoon of bangladesh," *Journal of Animal Sciences and Livestock Production*, vol. 02, no. 01, 2018, [Online; accessed 2023-07-24].

[121] V. H. Bumbieris Junior, J.-C. Emile, C. C. Jobim, R. M. Rossi, E. H. Horst, and S. Novak, "Performance and milk quality of cows fed triticale silage or intercropped with oats or legumes," *Scientia Agricola*, vol. 78, no. 2, e20190124, 2021.

[122] Solcast, *Global solar irradiance data and pv system power output data*, [Online; accessed 2024-02-01], 2024.

[123] H. Lindorfer, R. Braun, and R. Kirchmayr, "Self-heating of anaerobic digesters using energy crops," *Water Science and Technology*, vol. 53, no. 8, pp. 159–166, Apr. 1, 2006.

[124] S. Mokhatab, W. A. Poe, and J. Y. Mak, "Natural Gas Compression," in *Handbook of Natural Gas Transmission and Processing*, Elsevier, 2019, pp. 433–461, ISBN: 978-0-12-815817-3.

[125] T. Pettersen and K. Lien, “A new robust design model for gas separating membrane modules, based on analogy with counter-current heat exchangers,” *Computers & Chemical Engineering*, vol. 18, no. 5, pp. 427–439, May 1994.

[126] A. Fache, “Power-to-gas : Développement d’un réacteur catalytique pour la production de méthane de synthèse,” Thèse de doctorat dirigée par Marias, Frédéric Énergétique Pau 2019, Ph.D. dissertation, 2019.

[127] J. Xu and G. F. Froment, “Methane steam reforming, methanation and water-gas shift: I. Intrinsic kinetics,” *AIChE Journal*, vol. 35, no. 1, pp. 88–96, Jan. 1989.

[128] T. Huld, R. Müller, and A. Gambardella, “A new solar radiation database for estimating pv performance in europe and africa,” *Solar Energy*, vol. 86, no. 6, pp. 1803–1815, Jun. 2012.

[129] ECOMEMBRANE, *Cupola m2 heat shield option*, [Online; accessed 2024-04-04].

[130] M. Lafratta *et al.*, “Development and validation of a dynamic first order kinetics model of a periodically operated well-mixed vessel for anaerobic digestion,” *Chemical Engineering Journal*, vol. 426, p. 131 732, Dec. 2021.

[131] R. Andreani, E. G. Birgin, J. M. Martínez, and M. L. Schuverdt, “On Augmented Lagrangian Methods with General Lower-Level Constraints,” *SIAM Journal on Optimization*, vol. 18, no. 4, pp. 1286–1309, Jan. 2008.

[132] H. Butemann and K. Schimmelpfeng, “Long-term electricity production planning of a flexible biogas plant considering wear and tear,” *Journal of Business Economics*, vol. 90, no. 9, pp. 1289–1313, Nov. 2020.

[133] T. Reinelt and J. Liebetrau, “Monitoring and Mitigation of Methane Emissions from Pressure Relief Valves of a Biogas Plant,” *Chemical Engineering & Technology*, vol. 43, no. 1, pp. 7–18, Jan. 2020.

[134] G. M. Yuki Junior, S. Sochard, E. Dinuccio, and F. Marias, “Numerical tool for dynamic simulation of anaerobic digesters including an air-inflated double membrane gasholder,” in *Computer Aided Chemical Engineering*, vol. 52, DOI: 10.1016/B978-0-443-15274-0.50500-X, Elsevier, 2023, pp. 3135–3140, ISBN: 978-0-443-15274-0.

[135] K. E. Brenan, S. L. Campbell, and L. R. Petzold, *Numerical Solution of Initial-Value Problems in Differential-Algebraic Equations*. Society for Industrial and Applied Mathematics, Jan. 1995, ISBN: 978-0-89871-353-4 978-1-61197-122-4.

[136] L. Colelli, C. Bassano, N. Verdone, V. Segneri, and G. Vilardi, "Power-to-Gas: Process analysis and control strategies for dynamic catalytic methanation system," *Energy Conversion and Management*, vol. 305, p. 118 257, Apr. 2024.

[137] R. de Transport d'Èlectricité, *RTE, France's Transmission System Operator | RTE*, Jan. 2021.

[138] European Commission. Joint Research Centre., *Clean Energy Technology Observatory, Hydropower and pumped hydropower storage in the European Union: status report on technology development, trends, value chains and markets : 2023.* LU: Publications Office, 2023.

[139] R. Kumar *et al.*, "Different energy storage techniques: Recent advancements, applications, limitations, and efficient utilization of sustainable energy," *Journal of Thermal Analysis and Calorimetry*, vol. 149, no. 5, pp. 1895–1933, Mar. 2024.

[140] franceinfo, *Electricité : Vers une redéfinition des heures pleines et heures creuses*, Sep. 2024.

[141] T. Huld, R. Müller, and A. Gambardella, "A new solar radiation database for estimating PV performance in Europe and Africa," *Solar Energy*, vol. 86, no. 6, pp. 1803–1815, Jun. 2012.

[142] W. H. McAdams, *Heat transmission*, 3rd ed., International student ed. Auckland: McGraw-Hill, 1958, OCLC: 154318179, ISBN: 978-0-07-085483-3.

[143] S. W. Churchill and H. H. Chu, "Correlating equations for laminar and turbulent free convection from a vertical plate," *International Journal of Heat and Mass Transfer*, vol. 18, no. 11, pp. 1323–1329, Nov. 1975.

[144] S. W. Churchill and H. H. Chu, "Correlating equations for laminar and turbulent free convection from a horizontal cylinder," *International Journal of Heat and Mass Transfer*, vol. 18, no. 9, pp. 1049–1053, Sep. 1975.

[145] S. W. Churchill and M. Bernstein, "A correlating equation for forced convection from gases and liquids to a circular cylinder in crossflow," *Journal of Heat Transfer*, vol. 99, no. 2, pp. 300–306, May 1, 1977.

[146] F. P. Incropera, D. P. DeWitt, T. L. Bergman, and A. S. Lavine, *Fundamentals of Heat and Mass Transfer*, 6th edition. New York: John Wiley & Sons Ltd, 2007, OCLC: 868311388, ISBN: 978-0-470-05554-0.

[147] W. M. Kays and M. E. Crawford, *Convective heat and mass transfer* (McGraw-Hill series in mechanical engineering), Third edition. New York St. Louis San Francisco Auckland Bogotá Caracas Lisbon London Madrid Mexico Milan Montreal New

Delhi Paris San Juan Singapore Sydney Tokyo Toronto: McGraw-Hill, Inc, 1993, ISBN: 978-0-07-112516-1.

[148] A. P. Colburn, "A method for correlating forced convection heat transfer data and a comparison with fluid friction," *Trans. AIChE*, vol. 29, pp. 174–210, 1993.

[149] V. Gnielinski, "New equations for heat and mass transfer in the turbulent flow in pipes and channels," *NASA STI/Recon Technical Report A*, vol. 41, pp. 8–16, Jan. 1, 1975, ADS Bibcode: 1975STIA...7522028G.

[150] B. Petukhov, "Heat transfer and friction in turbulent pipe flow with variable physical properties," in *Advances in Heat Transfer*, vol. 6, DOI: 10.1016/S0065-2717(08)70153-9, Elsevier, 1970, pp. 503–564, ISBN: 978-0-12-020006-1.

ECOLE DOCTORALE
ED 211 – Sciences exactes et leurs application

LABORATOIRE
LaTEP (UPPA) / DISAFA (UniTO)

gyjunior@univ-pau.fr